AD-A037 375 DENVER UNIV COLO DEPT OF PHYSICS AND ASTRONOMY F/G 4/1
WATER VAPOR, NITRIC ACID AND OZONE MIXING RATIO HEIGHT PROFILES--ETC(U)
FEB 77 D G MURCRAY, J N BROOKS, A GOLDMAN DAAD05-74-C-0795
UNCLASSIFIED BRL-CR-332 NL

1 OF 2
ADA037375

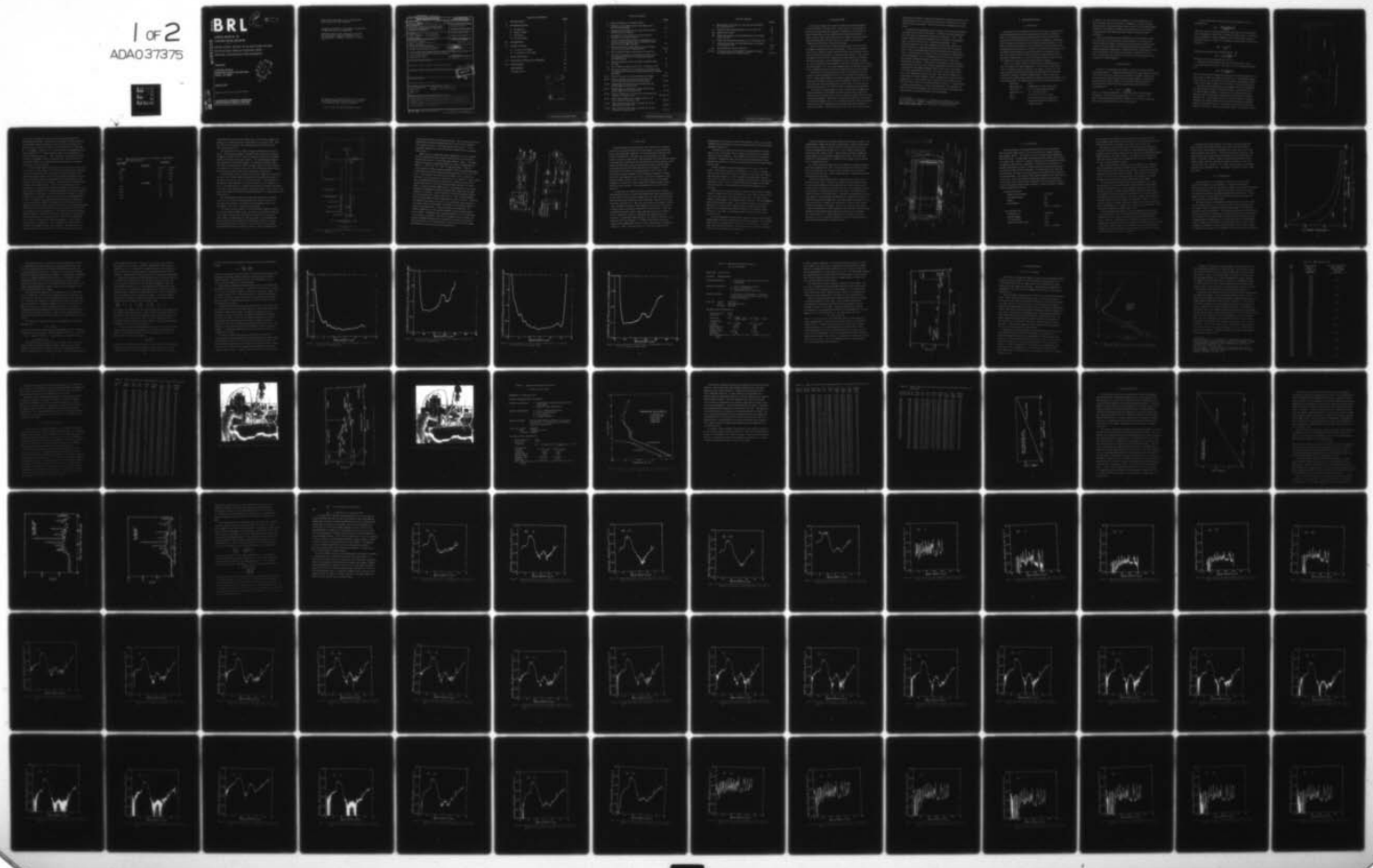

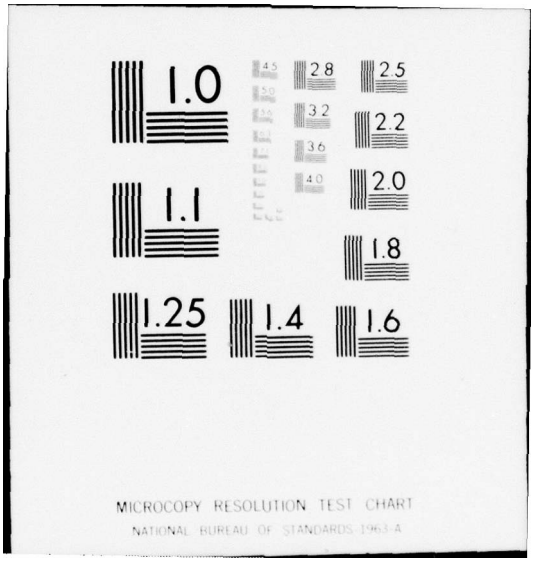
1.0
1.1
1.25
1.4
1.6
1.8
2.0
2.2
2.5
2.8
3.2
3.6
4.0
4.5
5.0
MICROCOPY RESOLUTION TEST CHART
NATIONAL BUREAU OF STANDARDS 1963-A

BRL CR 332

BRL

AD

CONTRACT REPORT NO. 332

(Supersedes IMR Nos. 267 and 361)

WATER VAPOR, NITRIC ACID AND OZONE MIXING RATIO HEIGHT PROFILES DERIVED FROM SPECTRAL RADIOMETRIC MEASUREMENTS

Prepared by

University of Denver
Department of Physics and Astronomy
Denver, CO 80208

February 1977

USA BALLISTIC RESEARCH LABORATORY
ABERDEEN PROVING GROUND, MARYLAND

Destroy this report when it is no longer needed.
Do not return it to the originator.

Secondary distribution of this report by originating or sponsoring activity is prohibited.

Additional copies of this report may be obtained from the National Technical Information Service, U.S. Department of Commerce, Springfield, Virginia 22151.

The findings in this report are not to be construed as an official Department of the Army position, unless so designated by other authorized documents.

The use of trade names or manufacturers' names in this report does not constitute indorsement of any commercial product.

UNCLASSIFIED

SECURITY CLASSIFICATION OF THIS PAGE (When Data Entered)

REPORT DOCUMENTATION PAGE

READ INSTRUCTIONS BEFORE COMPLETING FORM

1. REPORT NUMBER: CONTRACT REPORT NO. 332	2. GOVT ACCESSION NO.
3. RECIPIENT'S CATALOG NUMBER: BRL (19) CR-332	
4. TITLE (and Subtitle): WATER VAPOR, NITRIC ACID AND OZONE MIXING RATIO HEIGHT PROFILES DERIVED FROM SPECTRAL RADIOMETRIC MEASUREMENTS.	5. TYPE OF REPORT & PERIOD COVERED: Scientific Report
	6. PERFORMING ORG. REPORT NUMBER
7. AUTHOR(s): David G. Murcray, John J. Kosters, James N. Brooks, W. John Williams, Aaron Goldman	8. CONTRACT OR GRANT NUMBER(s): DAAD05-74-C-0795 new
9. PERFORMING ORGANIZATION NAME AND ADDRESS: University of Denver, Dept of Physics and Astronomy, Denver, CO 80208	10. PROGRAM ELEMENT, PROJECT, TASK AREA & WORK UNIT NUMBERS: (12) 138 p.
11. CONTROLLING OFFICE NAME AND ADDRESS: US Army Ballistic Research Laboratory, Aberdeen Proving Ground, MD 21005	12. REPORT DATE: FEBRUARY 1977
	13. NUMBER OF PAGES: 139
14. MONITORING AGENCY NAME & ADDRESS (if different from Controlling Office): US Army Materiel Development & Readiness Command, 5001 Eisenhower Avenue, Alexandria, VA 22333	15. SECURITY CLASS. (of this report): UNCLASSIFIED
	15a. DECLASSIFICATION/DOWNGRADING SCHEDULE

16. DISTRIBUTION STATEMENT (of this Report)

Approved for public release; distribution unlimited.

17. DISTRIBUTION STATEMENT (of the abstract entered in Block 20, if different from Report)

18. SUPPLEMENTARY NOTES

Supersedes IMR Nos. 267 and 361.

19. KEY WORDS (Continue on reverse side if necessary and identify by block number)

Spectral Radiometry
Water Vapor
Nitric Acid
Ozone
Atmospheric Constituent Profiles
Atmospheric Emission Spectroscopy

20. ABSTRACT (Continue on reverse side if necessary and identify by block number)

Two balloon flights of 27 June 1974 and 19 February 1975 are reported here. The LHe spectral radiometer which was developed for these flights is described in detail. The calibration and data reduction procedures are also described in detail. Plots of spectral radiance at various altitudes up to 38 km are shown. Finally mixing ratio height profiles derived from this data for H_2O, HNO_3 and O_3 are calculated.

DD FORM 1 JAN 73 1473 EDITION OF 1 NOV 65 IS OBSOLETE

UNCLASSIFIED 407002

SECURITY CLASSIFICATION OF THIS PAGE (When Data Entered)

TABLE OF CONTENTS

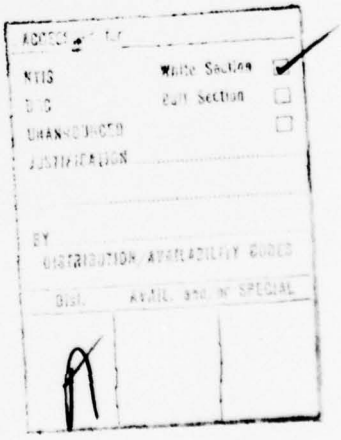

LIST OF FIGURES

LIST OF TABLES

I. INTRODUCTION

This report contains the scientific results of two balloon flights on 27 June 1974 and 19 February 1975. It describes the instrumentation flown and its calibration, the reduction of flight data, the analysis of a portion of that data, and an evaluation of the system performance. A similar report, with results from three later flights, will be presented separately; although occasional reference is made in this report to comparisons with the later calibrations and data.

There are several ways to measure minor gases in the terrestrial atmosphere using passive infrared techniques. They are all variations of the inverse radiative transfer problem of inferring constituent concentrations from the transmitted or emitted spectral radiance. One of these techniques uses the sun as a radiant source and measures the change in spectral transmittance of the atmosphere as either a function of height or, from a constant, elevated height, as a function of changing secant including zenith angles $> 90^{o}$. A second technique measures the spectral emission of the constituents both as a function of height and selected zenith angles.

Generally, the spectral resolution of the first technique is greater, making constituent identification easier, but is limited to absorptivities ≥ 0.01. These measurements are limited to daylight hours and specifically to sunrise and sunset in the case of the long path ($\theta \geq 90^{o}$) data. In contrast, spectral emission measurements can be made at any time and can measure emissivities $\leq 10^{-4}$ with an order of magnitude less resolution.

In an effort to obtain diurnal as well as seasonal and geographic data and in preparation for the flights discussed in this report, a spectral radiometer was designed and constructed capable of measuring emissivities of known atmospheric constituents as a function of height and zenith angle at selected geographic sites. The constituents and their spectral properties had been previously identified from solar absorption spectroscopy and laboratory studies. This instrument was one of the first scanning grating

spectrometers designed to operate at liquid helium temperatures and several subtle problems were encountered which had to be resolved for successful operation of the instrument. These are discussed in appropriate sections below.

A brief discussion dealing with the selection of this particular spectral instrument may be useful at this point. To obtain constituent height profiles from emission data requires spectral resolutions $< 3\ cm^{-1}$. The actual resolution requirement depends on the constituent, but normally a higher resolution provides more constituent information. From a practical point of view, filter radiometer systems offer neither adequate resolution nor sufficient spectral purity for the desired measurements. Any instrumental debate reduces to diffraction techniques (grating) vs interferometric techniques (Fourier transform) or combinations of each (Hadamard). Any real comparison of these two basic forms of spectroscopy ultimately depends on the physical source of the noise generated at the detector. If the detector preamplifier system is photon noise limited, then there is no multiplex advantage of the interferometric system and the throughput advantage reduces to the ratio of the square roots of the etendue of each system. This ratio is in the range of from one to ten, depending on specific systems. Since the two systems are, in principle, not greatly different, other considerations become the determining factors. In this specific case, these factors were experience of the University of Denver with cold grating spectrometers, [1] the possibility of using a grating system as a filter monochromator, the availability of real time spectral information, and the lack of success of field type cold interferometric systems at the date of this undertaking.

---

[1] J. N. Brooks, A. Goldman, J. J. Kosters, D. G. Murcray, F. H. Murcray and W. J. Williams, "Balloon-Borne Infrared Measurements", Phys. Chem. Upper Atmos. (B. McCormac, ed.) 278-285, 1973.

II. INSTRUMENTATION

A. Introduction

In preparation for the flights described in this report, a liquid helium cooled grating spectrometer was designed and built at the University of Denver. The design parameters were chosen such that the instrument could measure the spectral emission from minor atmospheric constituents of the stratosphere and operate from a balloon supported platform. The features of this spectrometer are described below, along with some of the initial problems encountered. A second, nearly identical spectrometer was developed simultaneously with this instrument for incorporation in the nose section of the WB57F aircraft as part of the Department of Transportation's CIAP program. A few of the design features, primarily external configuration, have derived from this functional dualism.

There are a number of basic considerations in designing a spectrometer for operation at LHe temperatures. The normal considerations, such as resolution, spectral range(s), scan time(s), field of view, etc. were assigned values based on the spectral information and sensitivity required to calculate constituent height profiles. These values were derived from available high resolution transmittance data and medium resolution emission data. The following values were used as design guidelines:

Resolution	1 cm^{-1}
Spectral Range	3-30μm total, in selected intervals
Scan Time	1/2 - 2 min, possibly adjustable
External F.O.V.	1/2 - 1° in the vertical
NER	10^{-8} to 10^{-9} w cm^{-2} sr^{-1} μm^{-1}
Optics	Low emissivity and low temperature (instrument emission should be low relative to data)

In addition, the instrument was designed for remote operation, low power operation (due to heat load on cryogenics), 12 hour minimum operating time, measuring incident radiance from several elevation angles, operation at stratospheric temperatures and pressures, and sustaining 15-20 g's shock in any plane (parachute impact) and possibly retain calibration.

There are also some special considerations associated with cooling the instrument to LHe temperature and containing it in a high vacuum. These include such things as operating moving mechanical systems (grating drive, optical chopper, switches) and providing an optical design (and mounting) that is temperature compensating; thus avoiding both external access to alignment when cold and stressing or cracking the mirrors. Some consideration was also given to the nature of the preamplifier since the detector is high impedance.

B. Optical Design

Selection of an appropriate grating(s) is the principle step in designing the spectrometer. Using the grating equation, the expression for Rayleigh diffraction limit and the equation for instrument throughput, expressions can be derived relating the grating size and blaze angle to resolution and noise equivalent radiance (NER). The minimum usable grating size is determined by the desired resolution and the diffraction limit of the grating aperture:

$$d\nu = 1\ \text{cm}^{-1} = \frac{0.61}{w \sin\theta},$$

where w = width of grating and θ = operational angle (to the normal) of the grating. This minimum grating width is w = 1.2 cm for $\theta = 30^{\circ}$. Since most gratings do not perform at 100% of their theoretical resolving power, the grating should be at least slightly larger.

The instrument NER is also affected by the grating size in the following way:

$$NER = \frac{NEP\ (of\ detector)}{(A\Omega)\ d\lambda\tau},$$

where $A\Omega$, the area of the grating and the solid angle of the slit aperture, is the throughput or etendue, $d\lambda$ is the spectral interval and τ is the instrument transmission. The throughput can also be expressed in terms of the spectrometer slit width (s), slit height (ℓ), grating width (w) and focal length (F) as:

$$A\Omega = \frac{s \cdot \ell \cdot w^2}{F^2}$$

Using the grating equation and substituting $d\theta = \frac{s}{F}$,

$$A\Omega = \frac{\ell}{F} \frac{d\nu}{\nu} \frac{2 \sin\theta}{\cos\theta} w^2,$$

where $\frac{\ell}{F}$ is the Fastie parameter and is $\leq 1/30$.

Most spectrometer designs have similar f/numbers (the ratio of F/w) within about 50% limits. If the ratio F/w = a is considered constant, then

$$A\Omega = \frac{d\nu}{\nu} \frac{2 \sin\theta}{\cos\theta} \frac{\ell\ w}{a}$$

and, for a specific wavelength and resolution, the throughput improves with an increase in angle, slit height and grating size. The throughput scales either linearly or as the square of the grating width, depending on whether or not the slit height is scaled with an increase in the grating dimension.

The results of the diffraction and throughput criteria are compatible and indicate that the larger the grating the better the instrument, which is a well accepted conclusion. The limit on the grating size became a practical choice of the largest configuration which could be reasonably operated cold. This limit was set at 8.4 cm square based on arguments relating to instrument weight and size and after calculating an adequate NER for a grating of this size. It should be noted that both θ and ℓ have practical restrictions. Since the wavelength range to be scanned is broad,

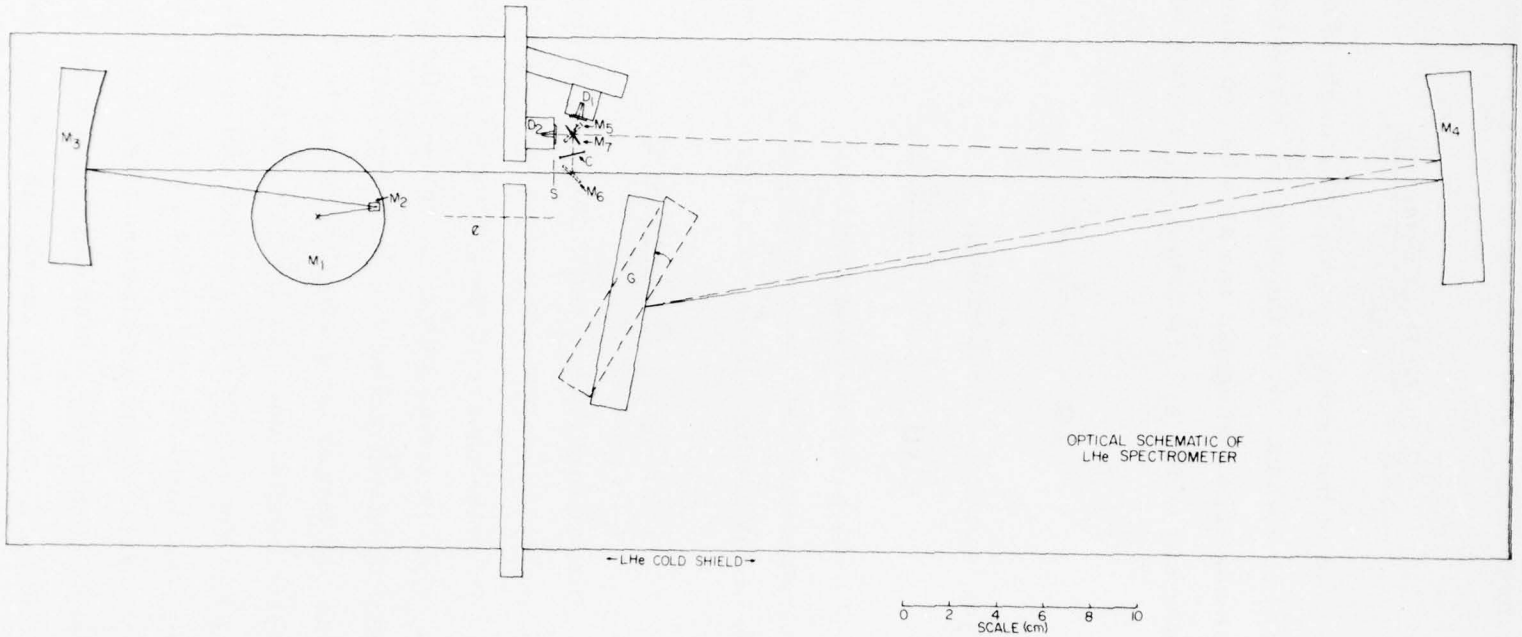

Figure 1. Optical schematic of LHe Spectrometer

θ cannot be too large due to the functional relationship between the grating efficiency and θ. The limit on ℓ is related to maximum detector sizes and the available techniques to reduce the exit slit image to the detector size. In this case a limit of 1 cm was placed on ℓ: assuming $\frac{\ell}{F} \sim 1/30$ and $\frac{F}{W} \sim 5$, then at w = 6 cm the increase in throughput becomes linear instead of $\sim w^2$. The instrument volume is still scaling as w^3 and the weight by at least w^2. Thus, there may be a point at which the increase in throughput reaches a practical limit. The size of 8.4 cm was chosen because it is a standard Bausch and Lomb size and meets the various criteria discussed.

The Littrow type mount was selected for the grating because one less large mirror is required than in a Czerny-Turner type mount. Therefore it can be mounted in a smaller volume for the same grating size and spectrometer focal length. Also, at the resolution anticipated, slit curvature is not important and the conventional circular slit geometry of the Czerny-Turner system is not needed. Figure 1 shows the selected optical schematic of the spectrometer. There are several features in this design which are related to the low level of signals to be measured. The optical beam is dispersed twice (double passed) by the grating and optically chopped after the first pass. This not only improves the spectral purity, but provides a radiometric reference at 4K which, for all purposes here, is zero. In addition, the image plane after the first pass is displaced from the slit-detector plane by the height of the slit such that no direct radiation from the first pass falls onto the detectors (even though unchopped). This is necessary because large amounts of dc radiation on the detector can change the noise and responsivity. The sequence through the optical path is as follows: radiation from the fore-optics passes through baffles in the LHe heat sink to the entrance slit (s), from s to the collimating mirror (M_4), to the grating (G), back to M_4 and M_5. The first pass terminates at the chopper (C). The second pass is similar to the first, starting at the chopper, off M_6, M_4, G and M_4. The final focus is at the light cones in front of the detectors after either passing through or

Table I. Spectrometer Resolution as a Function of Wavelength for 2 mm wide slits.

Wavelength	Resolution	
	2nd order	
9.0μm	$3.8 cm^{-1}$	.031μm
10.0	3.0	.030
11.0	2.4	.029
12.0	2.0	.029
13.0	1.7	.029
	1st order	
18.0	1.9	.062
20.0	1.5	.060
22.0	1.2	.058
24.0	1.0	.058
26.0	0.8	.057

reflecting off the dichroic beam splitter M_7. Note that the chopper, M_5 and M_6 are in a plane below that of the detectors, M_7 and the slit. Also, the exit slit is one end of a short light pipe utilized to match the slit size to the detector size.

Currently there are two replica gratings available for the spectrometer. One is blazed at 10μm at an angle of 22^o and the other is blazed at 22μm at an angle of 26.8^o. Both are mounted on aluminum substrates, which bolt directly into the spectrometer. The 22μm blazed grating has been used on the initial balloon flights, recording the 20-26μm region (1st order) with one detector and the 10-13μm region (2nd order) with the second detector. A 2mm slit was used on these flights and Table I shows the resolution attainable with this slit and grating combination.

The fore-optics shown in Figure 2 are used to couple the narrow field of view (F.O.V.) beam observed through the cold shields and window to the relatively fast, f/5, F.O.V. of the spectrometer. The actual F.O.V. through the window depends on the slit size which, for a 2 x 8mm slit, is 1 x 4^o. The spectrometer is oriented such that the slit length is horizontal. The center of the optical axis passes radially through the center of the vacuum dewar and changes in the observational height angle are accomplished by rotating the dewar.

The cold baffling is designed with the LHe baffles just on the edge of the F.O.V. and the internal LN_2 baffles just outside of the F.O.V. An image of the grating is formed near the LHe baffles closest to the LN_2 baffles. The F.O.V. diverges from that point.

The window, which is KRS5, is cooled during both flight and calibration with an external supply of LN_2. A reflective cold shield is attached to the copper cooling ring of the window and extends into the spectrometer dewar, overlapping the internal LN_2 baffle. This shield did not quite overlap the internal baffle on the flights described here, but has recently been extended to eliminate a large amount of stray radiation being admitted through the gap and scattered or reflected off the window

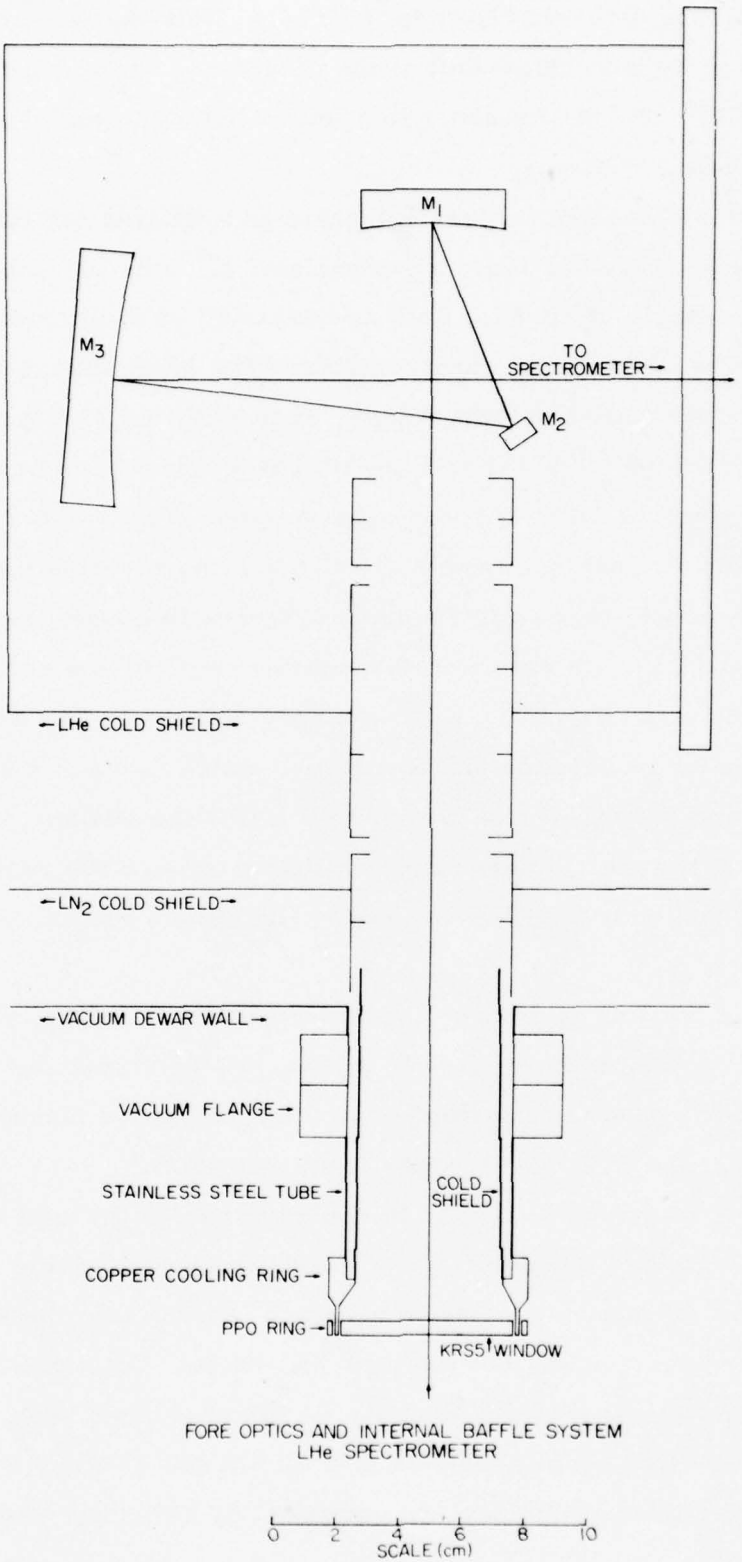

Figure 2. Schematic of LHe Spectrometer fore optics and internal baffle system

into the spectrometer (see discussion below). The LN_2 and LHe internal baffling and the external baffling also serve to block stray radiation from outside the F.O.V. from entering the spectrometer. This is especially important for observations near and below the local horizon (limb scans).

Upper limits on a desirable window temperature can be calculated based on expected minimum radiance levels at 40km, the emissivity of KRS5 and some ratio criterion between these two values. From data obtained with an LN_2 cooled spectrometer at 30km, extrapolations for 40km are $\sim 10^{-8}$ w cm^{-2} sr^{-1} μm^{-1} at 12μm and 24μm. Using the criterion that the window emission should be $\leq$ 10% of the minimum signal to be measured, then the window emission should be $\simeq 10^{-9}$ w cm^{-2} sr^{-1} μm^{-1}. The primary transmission loss of KRS5 is due to reflection at two faces, so the absorption or emissivity is $\leq$ 2%. However, some contribution to the apparent emissivity comes from the reflection term as the window looks back into the LN_2 and LHe shielded regions of the instrument. To what extent the window looks at LN_2 temperatures versus LHe temperatures depends on the optical quality of the window and the angle at which it is mounted. A close estimate of the desired window temperature can be obtained by using an emissivity of $\sim$ 10%. Window temperatures of 78K at 12μm and 50K at 24μm meet the above criterion. From this it is apparent that some correction in the reduced data will be necessary for window radiance at the longer wavelength, even though the window is cooled to LN_2 temperature. Three parameters are important: the window temperature, the LN_2 baffle temperature and the optical quality of the window. Perhaps the most important parameter is the temperature of the internal LN_2 baffles. Before the cold baffle from the window cooling was extended, knowledge of the temperature near the window mount was also necessary since the dominant correction required on the flights discussed here was derived from this temperature.

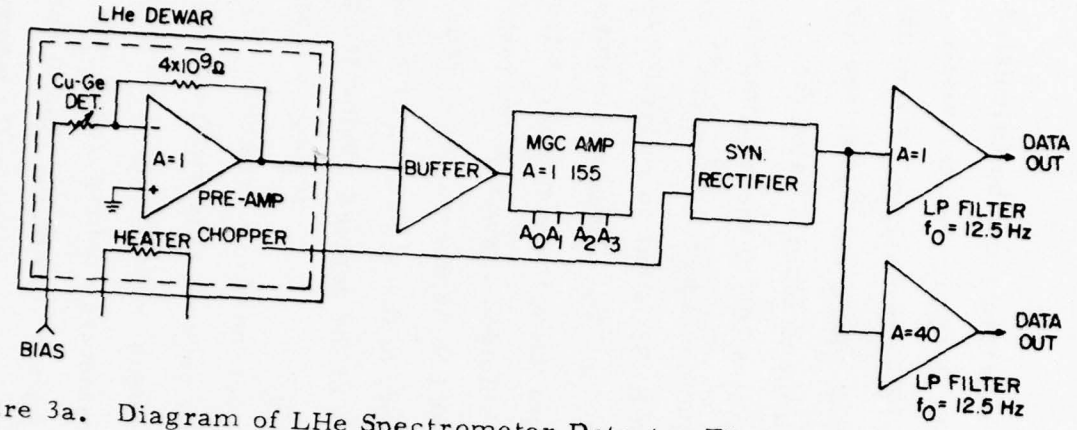

Figure 3a. Diagram of LHe Spectrometer Detector Electronics

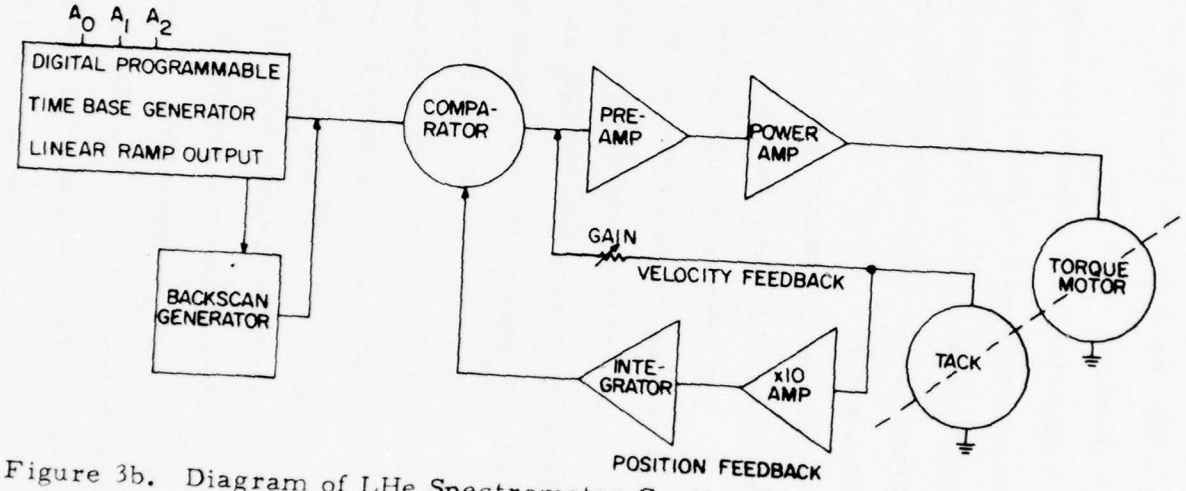

Figure 3b. Diagram of LHe Spectrometer Grating Drive System

C. Electronics

Two Santa Barbara Research Center Ge:Cu detectors are mounted in the main cryostat at the end of short light pipes. As previously mentioned, these light pipes adapt the 1 x 4 mm dimensions of the detectors to exit slit dimensions. The detectors are heat sinked to the LHe reservoir through a copper block. One advantage of the spectrometer design is that separate vacuum dewars for the detectors are not necessary, which reduces the instrument size and eliminates the need for optical adjustment between the exit slit image and the detector position. The dark resistance of these detectors is approximately 5×10^{11} ohms. An electrometer type pre-amplifier with a high input impedance, shunted with a very low capacitance is therefore required for impedance matching of the signal transfer circuit. The input radiance is interrupted (chopped) at a 260 Hz rate with a tuning-fork chopper manufactured by American Time Products. The pre-amp (buffer) circuit is shown in Figure 3a.

To reduce the microphonic noise generated by tuned or vibrating leads between the detector and the pre-amp and the capacitance produced by long leads which would reduce signal due to RC loss, the detector pre-amp was physically mounted as close as possible to the detector inside a thermally controlled case. When this instrument was developed, commercially available electrometer-type amplifiers required too much power to operate, which presented an extreme heat load to the LHe. Also, the available electrometers had an input capacitance that was too high for the RC combination of detector impedance and chopping frequency. Therefore, considerable experimentation was required to develop a pre-amp with high input impedance ($\approx 10^{13}\,\Omega$), matched differential input stages and low supply power (40 mv for both channels) that would operate reliably at $\approx$ 200K. Because the gain "A" of the pre-amp is directly

proportional to the resistance value of the feedback resistor, R_f, R_f was isolated from the heated pre-amp environment and heat sinked to the LHe baseplate temperature.

Problems were experienced when the pre-amp temperature would get too cold (~ LN_2 temp). Some resistors would physically crack and become an open resistance. This problem caused failures and delays. Therefore, considerable effort was exercised to manually select components that would survive if the pre-amp temperature would inadvertently get too cold.

Another problem has been microphonics as the major source of noise. Unfortunately, detector resistance noise is not seen. Analog Devices now has available a new IC, low power, FET input, electrometer type op-amp, mounted in a TO-99 case that can be physically mounted very close to the detector mount, probably eliminating most of the present lead length. This, in turn, should decrease the microphonics and hopefully increase S/N. Time should be spent using this approach for a pre-amp.

Following the pre-amp, the detector signal is buffered with a voltage follower, mounted external to the dewar on a circuit board in the electronic case of the experiment control box (see Figure 3a). The signal is then wired to a gain amplifier controlled by binary switches. This gain amplifier has 16 gain settings ($\sqrt{2}$ apart). If in the future automatic gain control is desired, a circuit has been designed to detect the peak signal voltage level of the scan and logically adjust the gain for the following scan on that basis. This AGC circuit adapts easily to the present manual gain control circuit.

From the adjustable gain stage the ac signal is synchronously rectified using a phase reference signal from the tuning fork chopper. The dc signal is then fed to two low pass active filters (f_o = 25 Hz, June; f_o = 12.5 Hz, Feb.) with two parallel outputs: one with a gain of one and the second with a gain of 10 for June and 40 for Februrary.

The prime flight data recording system is an on-board recorder. The analog detector signal and all other "housekeeping" signals are processed with an analog to digital converter and then recorded with a University of Denver designed and developed 1/2", 7 track, digital, IBM format, long record time, tape recorder. This 8 channel recorder samples the analog signal of each channel 25 samples per second. One of the eight channels is submultiplexed for 16 inputs for low sample rate information such as temperatures, etc.

As a back-up the data signals are also real time recorded through an FM-FM, S-band telemetry link. This system lacks the desired accuracy if the recorded data is to be used for data reduction, but it provides a real time look at the data. If the program permits, a PCM system should be considered in the future.

The Bausch and Lomb grating is driven axially with a direct drive Aeroflex torque motor. Also directly coupled to the grating drive shaft is an Aeroflex tachometer used for position and velocity control in the closed loop drive system circuit (see Figure 3b). The signal which drives the grating is a ramp function derived from a binary controlled D to A converter driven from 100 kHz clock. This type of ramp generator features many options: 7 scans periods, programmed or command controlled scan stop mode, programable speed-up or slow-down mode during the scan, e.g. slow down the scan to improve the resolution at a specific band, and an externally adjustable scan length. Because of the hostile environment in which the grating drive system operates, special Bemol self-lubricating Fernalon AW polyimide ball bearings were selected for axial support. This torque motor-tach-ramp combination is a reliable, versatile, accurate, efficient, low power (typically 20 m W) low mass grating drive system that has operated successfully at 4.2K.

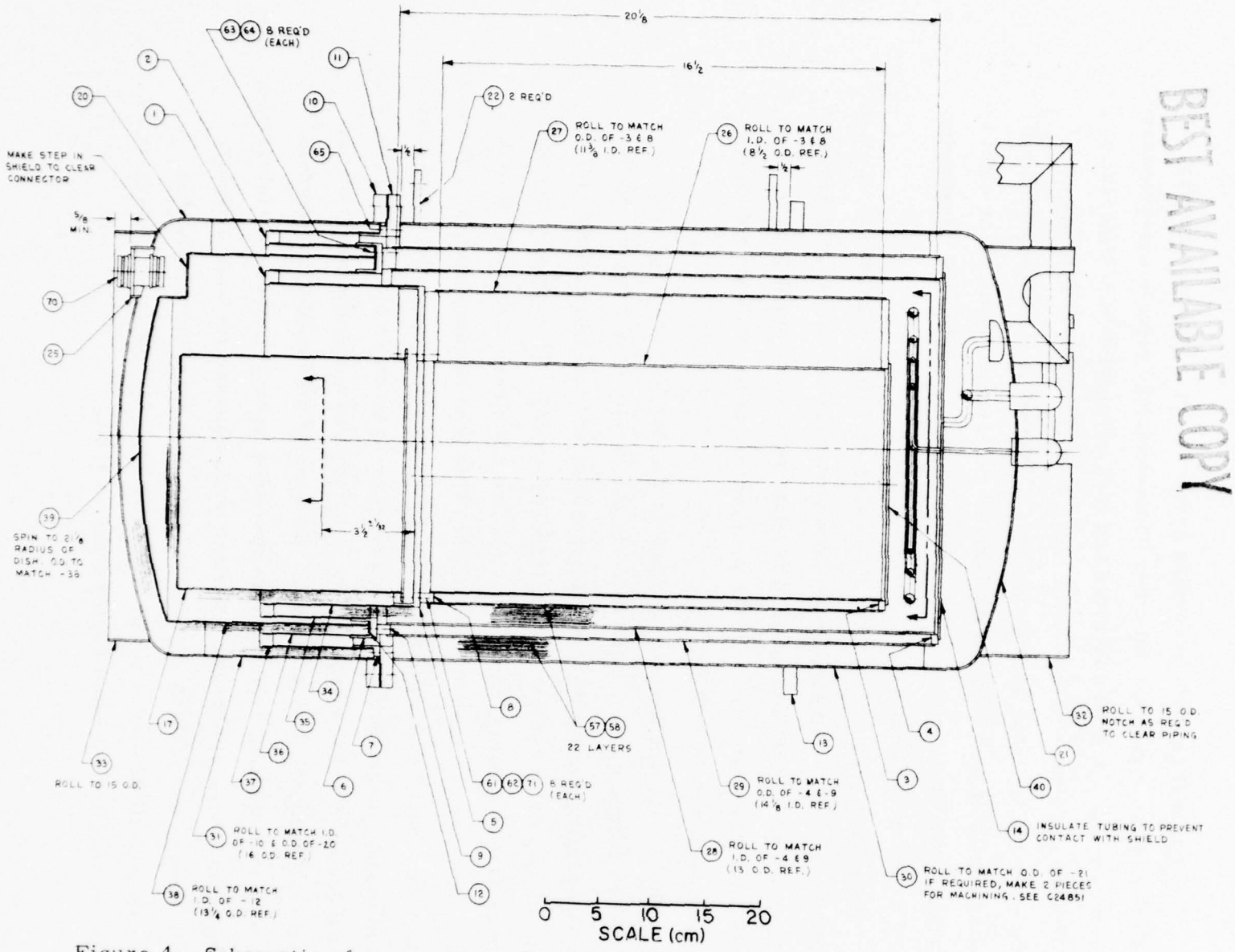

Figure 4. Schematic of crossection of vacuum dewar for mounting the LHe Spectrometer

D. Vacuum Dewar

The vacuum dewar was designed specifically for the spectrometer and its airborne applications. It was constructed by Cryogenic Engineering Company, Denver. The dewar is 0.46 m in diameter (plus plumbing) and 0.90 m long. It weighs about 100 kg and the spectrometer which mounts in it weighs 9 kg. There are a number of features which should be described to explain the spectrometer capabilities. The purpose of the dewar is to provide liquid helium cooling for the spectrometer and the Ge:Cu detectors mounted to the spectrometer base plate. The operational time, after filling, should be in excess of 12 hours to permit the launching and completion of a balloon flight. The amount of LHe required depends on the heat load from two sources. One is the external load through radiation and conduction and the other is the internal power dissipation of the grating spectrometer. For the final dewar design, shown in Figure 4, these heat loads are approximately summarized as follows:

External Heat Load	
Radiation and Insulation	.191 watts
Fiberglass Support	.062
Piping	.051
Miscellaneous	.010
	.314 w → .443ℓ/hr.
Internal Heat Load	
Grating Drive	.020 watts
Optical Chopper	.014
Pre-amp Heater	.050
Radiation through window	.050
	.134 w → .189ℓ/hr.

The LHe hold time should be 19 hours with the dewar capacity of 12ℓ. Times slightly longer than this (21-22 hours) have actually been measured, but the grating drive and chopper were off for most of that time.

The liquid nitrogen shield around the LHe dewar contains about 8ℓ of LN_2 with a hold time of over 48 hours. The external LN_2 supply for cooling the optical window contains 25ℓ and will cool the window and external baffle system for more than 12 hours. The window cooling system has relatively high heat inputs due to conductive and convective losses, i.e. it is not a vacuum insulated system.

The venting of both the He and N_2 gas is at points in the respective dewars that permit operating the dewar at observation angles of about -10° to 60° from the horizontal. Also, the dewar can operate vertically, standing on the end away from the window. This, however, rotates the F.O.V. ($4^{\circ} \times 1^{\circ}$) by 90° and also increases the temperature gradient between the LHe in the dewar and the spectrometer base plate.

The spectrometer and dewar system are suspended in the vacuum dewar with four re-entrant fiberglass cylinders which provide rigidity, mechanical strength for up to 20 g's loading on parachute impact and thermal insulation. Initially the spectrometer base plate of aluminum was coupled to the LHe through two large stainless steel washers and the stainless steel walls of the dewar. The initial coolings indicated that the base plate did not get cold enough for the detectors to operate. To aid thermal conductivity copper straps were soldered to the walls of the LHe dewar and brought out to a copper ring in contact with the base plate. This lowered the temperature considerably to < 7K.

Heat sinking the base plate was one of two problems encountered in the initial design. The second was that the LHe plumbing provided a resonant cavity for acoustic oscillations so that the LHe hold times were 2 - 12 hours. This problem was difficult to recognize due to lack of experience with the instrument and because the helium hold times usually were in the 8-12 hour range. Several experiences of 2 hour hold times resulted in carefully checking for thermal shorts and finally determining that the problem was acoustic oscillation.

Working with this spectrometer in its dewar requires significantly more time for testing and modifying than conventional spectrometers because of the times required for pumping the vacuum dewar and cooling and warming the spectrometer. Five days minimum are required to complete one test cycle of placing the spectrometer and cold shields into the dewar, evacuating, cooling, testing, warming and reopening the dewar. Slightly longer times are required if a bakeout procedure is used in the evacuation process. However, once tested, the spectrometer can be kept operational for extended periods. The longest such period to date is about one month.

III. CALIBRATION

The spectrometer is calibrated in the laboratory and in the field prior to each flight or series of flights. It is important that these calibrations are accurate and that all the variables are measured and changed in a controlled manner. The calibration provides a means of converting the voltages measured during flight to absolute spectral radiance. These radiance values are then used to calculate spectral emissivities and constituent profiles (see Data Reduction).

The spectrometer is calibrated by filling the field of view with a known source of uniform intensity. This source is then varied in intensity over the range of values anticipated during the balloon flight. The calibration is derived from two procedures. The two procedures consist of either using a series of single point calibrations at different temperatures and assuming zero radiance at zero voltage output or using successive calibrarion scans at slightly different temperatures in a differential mode and calculating the slope resulting from the radiance and voltage differences. In this manner a number of systematic errors can be determined, such as offset voltages, uncertainties in the value of the calibration source and system non-linearities.

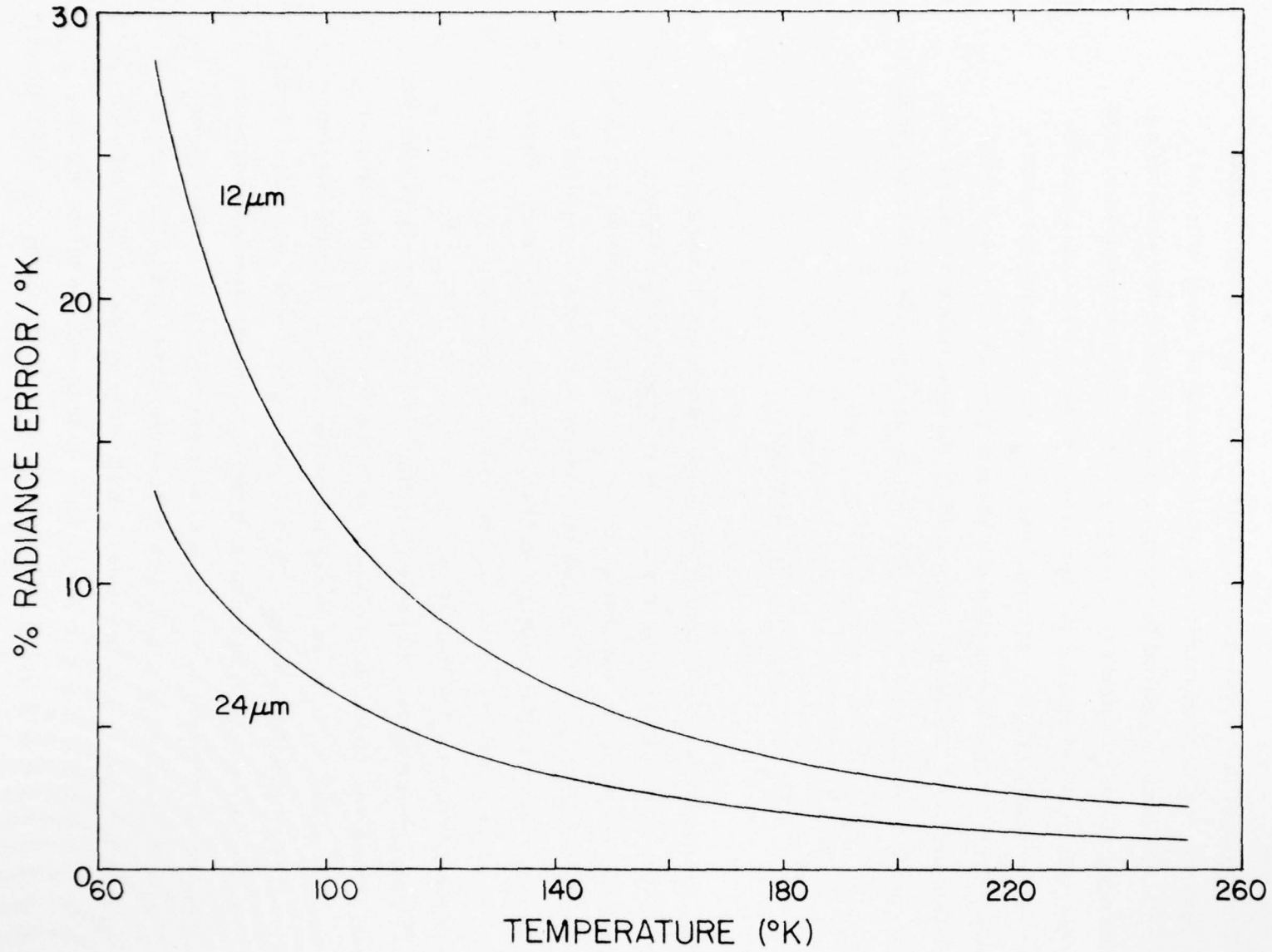

Figure 5. Functional relationship between a temperature error and the resulting radiance error of the Planck black body function at 12μm and 24μm.

The calibration source is usually a cavity with dimensions such that it is optically black to better than 0.99, an aperture that fills the field of view and walls that are heavy enough to be good thermal conductors to assure temperature uniformity. In addition, the black body is double walled with liquid nitrogen between the walls. This black body is operated cold over a range of temperatures down to 80K. It is important that it is mounted with sufficient overlap of the window mount to prevent warm radiation from entering the cavity through the aperture since there are five orders of magnitude between radiance values at room temperature and liquid nitrogen temperature at 12μm.

The uniformity and absolute value of temperature of the black body are very important. Errors of 1K in temperature of the black body can lead to errors in excess of 10% in the assumed radiance value (see Figure 5). The black body temperature is measured with sensors mounted in the wall at the end of the cylindrical shaped cavity. Both thermistors and platinum resistors are used as temperature sensors. Also, the LN_2 is pressurized and the temperature of the LN_2 at various pressures compared with the temperature sensors. With care these temperatures will agree to $\pm$ 0.2K, but systematic measuring errors can easily cause errors of $\pm$ 2K.

The calibration coefficient (K) for each wavelength is derived in the following way:

$$K'V = (\Sigma N_i),$$

where V is the detector output voltage at wavelength λ and ΣN_i is the sum of all the sources of spectral radiance incident on the detector. In general,

$$\Sigma N_i = N_B(\text{Black Body})\,\tau_B + N_W(\text{Window})\,\tau_W + N_M(\text{Mirrors})\,\tau_M - N_R(\text{Reference})\,\tau_R.$$

The quantities N_B, N_W, N_M and N_R are radiance values associated Plank radiation from their respective media. Only a fraction of this radiance will be incident on the detector due to the optical properties of the intervening path (i.e., the black body radiance will be partially absorbed

by the window and mirrors). Thus τ_B, τ_W, τ_M and τ_R have values in the range of 0.0 to 1.0 and are effective transmission terms for each radiance source. In reality each τ would be a product of terms such as mirror reflectivities, grating efficiency and window transmission and reflection. Most of these terms drop out of the calibration as shown below.

The general expression for ΣN_i contains terms for emission from the instrument mirrors and optical reference path (that which the detector sees during the closed portion of the tuning fork chopping). Since the mirrors and reference are at or near liquid helium temperature, these terms are zero. In addition the instrument transmission function, which includes mirror reflectivities and grating efficiency, can be incorporated into the calibration coefficient which is constant. The vacuum window transmission can also be included in the calibration coefficient but will still show up in the window correction term. Thus,

$$\frac{K'V}{\tau_I \tau_W} = KV = N_B + N_W \frac{\epsilon_W}{\tau_W} + N'_W \frac{R_W}{\tau_W} = N_B + N_W^*$$

where N'_W is the radiance from all sources being reflected internally from the window into the spectrometer. Both window terms should remain constant during calibration and for simplicity of expression can be referred to as N_W^*. (There may be some minor thermal coupling between the black body and the window but it does not appear to be important during the time frame of the calibration procedure.)

There are two ways of determining values for K as a function of wavelength. Both assume that the field of view is filled with a proper black body with controllable temperature. At each temperature of the black body a value for K can be calculated:

$$K = \frac{N_B + N_W^*}{V}.$$

If the detector and electronics are linear over the radiant range in question and if $N_W^* \ll N_B$, then K will be constant as N_B is varied. If K is not constant, the nature of this variability can be determined by calculating

the value of K from succeeding pairs of measurements in the differential fashion,

$$K = \frac{N_{1B} - N_{2B}}{V_1 - V_2} .$$

This proceedure removes errors in K due to window radiance and provides a means of measuring system linearity by varying N_B over the entire range of interest. This procedure is also very susceptible to errors in the measured temperature of the black body.

On the February flight the window radiance term was significant and the differential technique was used. The derived values of K were constant to 5-10% over the range of radiance to be measured during the flight. At very large radiance levels K became non-linear. Also at large radiance levels but in the linear region, the value of K calculated from the single point procedure was approximately equal to the linear value of K from the differential calculation.

A good relative calibration was also obtained for the June flight, but the magnitude of K was wrong, apparently due to slight icing of the window during the calibration procedure. The absolute magnitude of K was adjusted by a factor of 2.2 based on comparative atmospheric data with the Februrary flight. This leaves the absolute magnitude of the final data and derived constituent profiles for the June flight somewhat in question, but the relative shapes of the profiles should be accurate. The calibration coefficients used on these two flights are shown in Figures 6 through 9. The primary difference in K for the two dates results from a change in bias voltage.

A number of experiments have been performed to determine if variation of any of the instrument environmental parameters might change the calibration coefficients. The temperature of the liquid helium sink and the liquid nitrogen shield were varied by lowering the gaseous venting pressure, but the spectrometer output did not change when looking at a constant radiance source. Changes in the calibration can also be caused

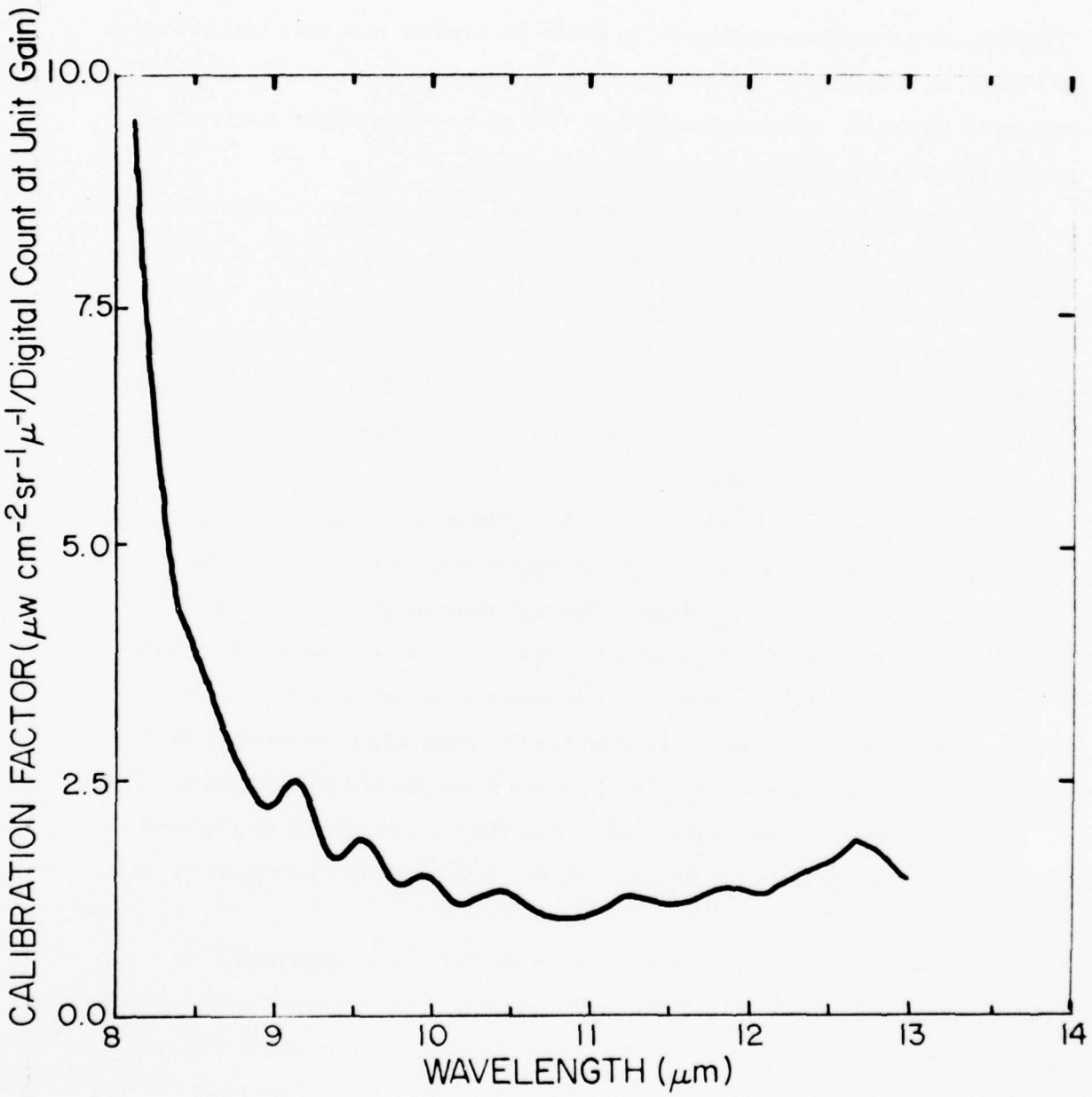

Figure 6. Plot of calibration coefficients (K_λ) vs wavelength for 27 June 1974 in the short wavelength region.

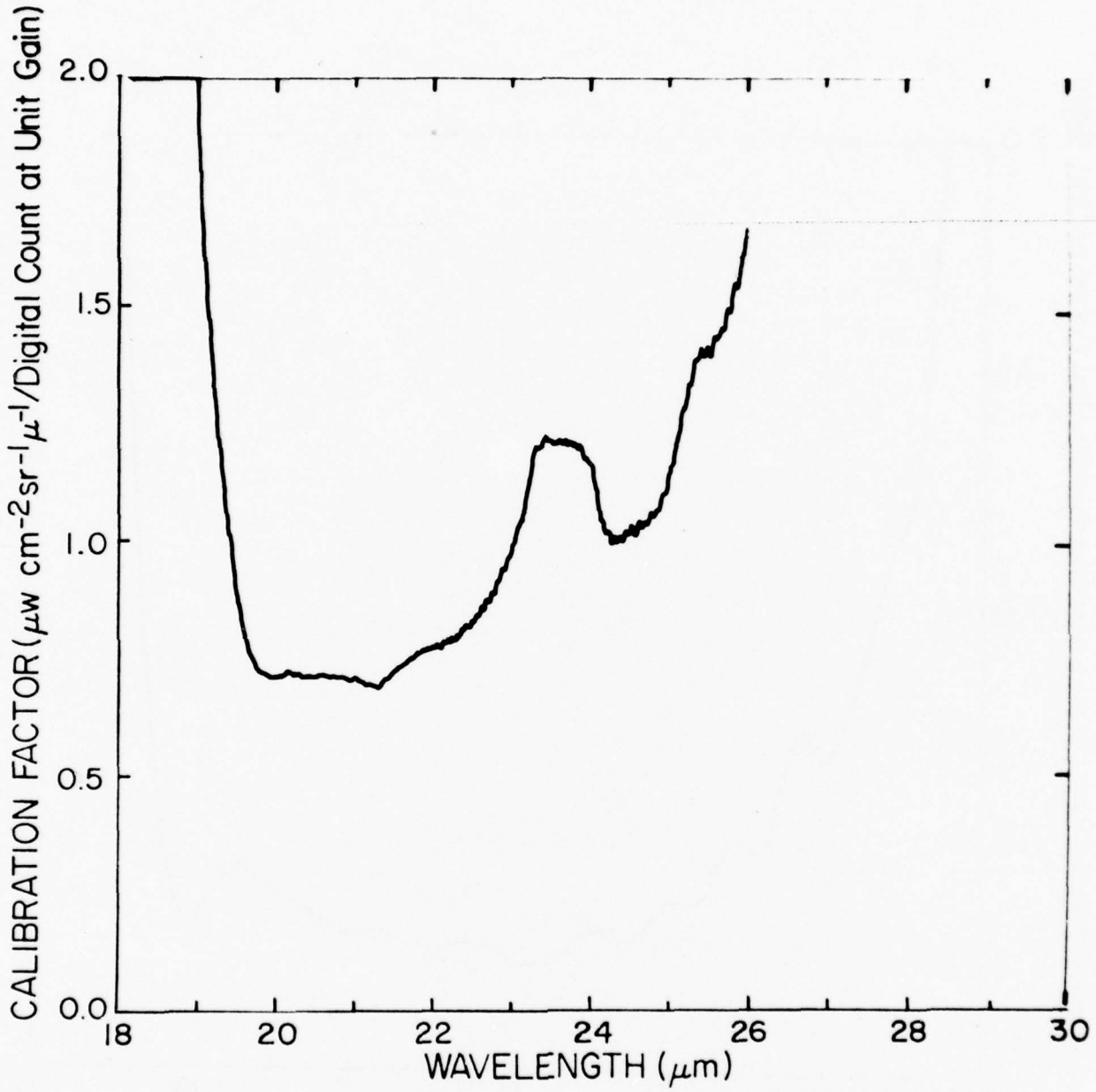

Figure 7. Plot of calibration coefficients (K_λ) vs wavelength for 27 June 1974 in the long wavelength region.

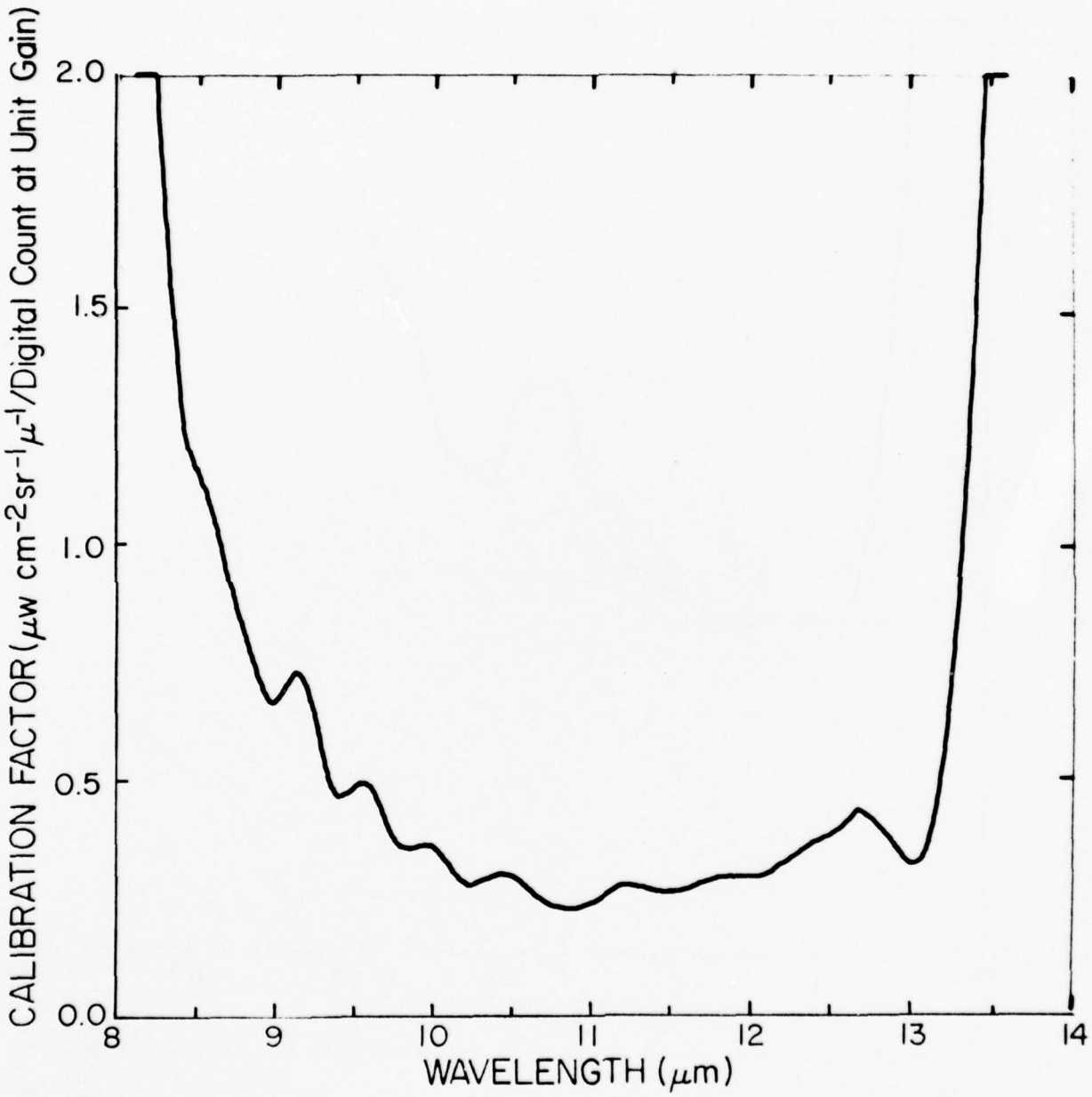

Figure 8. Plot of calibration coefficients (K_λ) vs wavelength for 19 February 1975 in the short wavelength region.

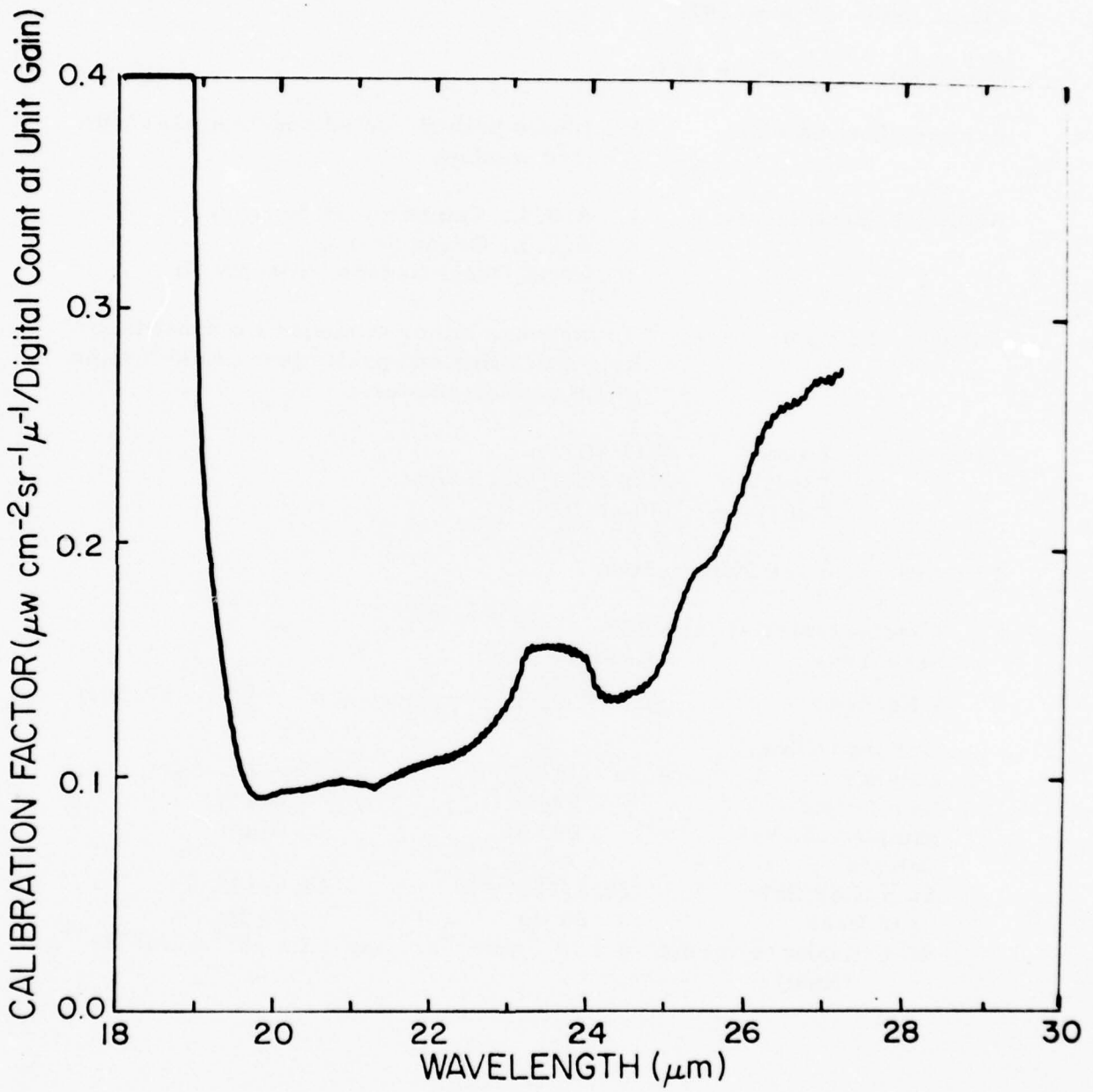

Figure 9. Plot of calibration coefficients (K_λ) vs wavelength for 19 February 1975 in the long wavelength region.

Table II. Flight and Instrument Parameters

27 June 1974 Flight

Flight Date: 27 June 1974

Location: Holloman AFB

Primary Instrument:

1. Liquid helium cooled spectrometer with cold window.

Auxiliary Instruments:

1. A.S.L. Temperature Sensors
2. A.S.L. Ozone Sensor
3. NASA Ozone Sensor (Hilsenrath)

Purpose of Flight: To measure minor atmospheric constituent height profiles and preliminary field testing of LHe spectrometer.

Time Log:

Launch	0711 MDT
Float	0928 MDT (38.0 km)
Cut Down	1404 MDT

LHe Spectrometer Parameters:

Window Material	KRS5	
Scan Time	43 sec	
λ Equation	$\text{char} = \frac{16420}{13.793} \frac{b'}{15030} (\sin^{-1}(\frac{n\lambda}{50}) - 17.703)$	
Grating Order	2	1
λ Range	8.50 - 13.00μm	19.20 - 26.15μm
Resolution	.03μm	.06μm
Sample Interval	.005μm	.01μm
Detector Bias	+ 4v	+ 4v
Amplifier Gain	22.5/225	15.8/158
Band Pass	25 Hz	25 Hz
NER (Realized during flight)	4×10^{-8} wcm^{-2}sr^{-1}μm	3×10^{-8} wcm^{-2}sr^{-1}μm

by shifts in optical alignment. To study this and other long term calibration variables, the instrument is calibrated several times before a flight, either as a complete black body calibration or as a one point calibration check (usually against a room temperature source). No measurable change in the calibration has been noted to date that can be related to shifts in alignment, which includes any effects due to transporting the instrument and recovery related shocks and vibrations.

The calibration is linearly related to the detector bias voltage. The bias value is established with the window cold and the black body cooled to a radiance level anticipated in the stratosphere. As a result the preamp is saturated at higher radiance levels. However, an auxiliary low voltage bias can be substituted for the flight bias for preflight checks.

Both the calibration and the data reduction processes assume proper wavelength identification of the data. The wavelength calibration is accomplished by measuring the positions of a large number of known atmospheric lines or line groups. These line positions are fitted by least squares to the grating equation based on the assumption of a constant angular velocity of the grating drive. The equation has the form:

$$n\lambda = 2d \sin(\omega t + \phi)$$

where d = 25 microns and t is the time base of the recorder expressed as data sample points. Values for the constant ω and ϕ are contained in Tables II and V. To date this method seems to be accurate to within a resolution element. Note that line positions from both orders of the grating (both detectors) must fit the grating equation using the same constants. Selected atmospheric lines are monitored during flight and minor adjustments are made to the equation to compensate for temperature effects on the drive circuitry. This is accomplished with a scaling parameter (b' or a) contained within the constant ω.

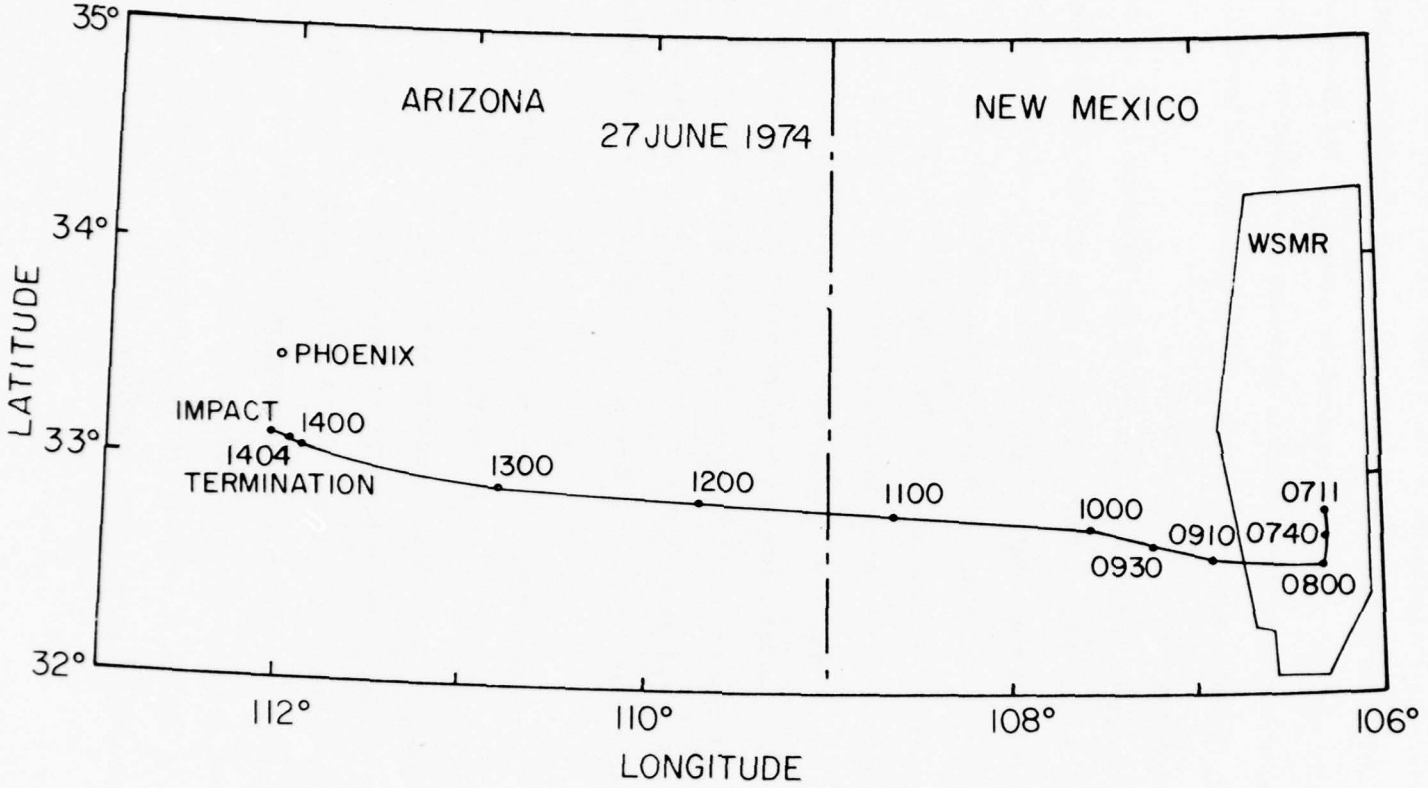

Figure 10. Plot of Balloon Flight trajectory for 27 June 1974.

IV. FLIGHT DETAILS

A. 27 June 1974 Flight

The 27 June 1974 flight was made in conjunction with the NASA LACATE Program and direct flight costs were allocated to that program. Prior to this flight difficulties were experienced with the liquid helium dewar hold times as was explained previously. This flight had originally been scheduled for early May and was postponed until June due to the required modifications.

This first flight was launched at 0711 MDT on 27 June 1974 at Holloman AFB. Table II summarizes the flight details. The main experiment on board was the above described spectral radiometer set to scan from 8.5μm to 13.0μm and from 19.2μm to 26.15μm. An Ozone Sensor developed by Hilsenrath of NASA Goddard was also on board. Also a pair of temperature sensors and an ozone sensor provided by Atmospheric Sciences Laboratory were flown. The instruments including control instrumentation and parachute weighed 682 kg and the balloon weighed an additional 595 kg. The balloon reached a float altitude of 38 km at 0928 MDT and remained at that altitude until termination at 1404 MDT. Figure 10 shows the flight trajectory. The parachute impacted south of Phoenix and the equipment was recovered and returned in good condition.

Temperature and humidity data from rawinsonde ascents near the time of the balloon flight were collected and plotted on a common plot. A smoothed average was selected as representative of the sonde data and used in the infrared radiance analysis process described in a later section. The sonde temperatures, dew points and smoothed curves are shown in Figure 11. Note the magnitude of variation of any one temperature measurement from the smoothed curve. This ΔT when interpreted radiometrically (Figure 5) represents a basic uncertainty in the inverse radiative transfer process.

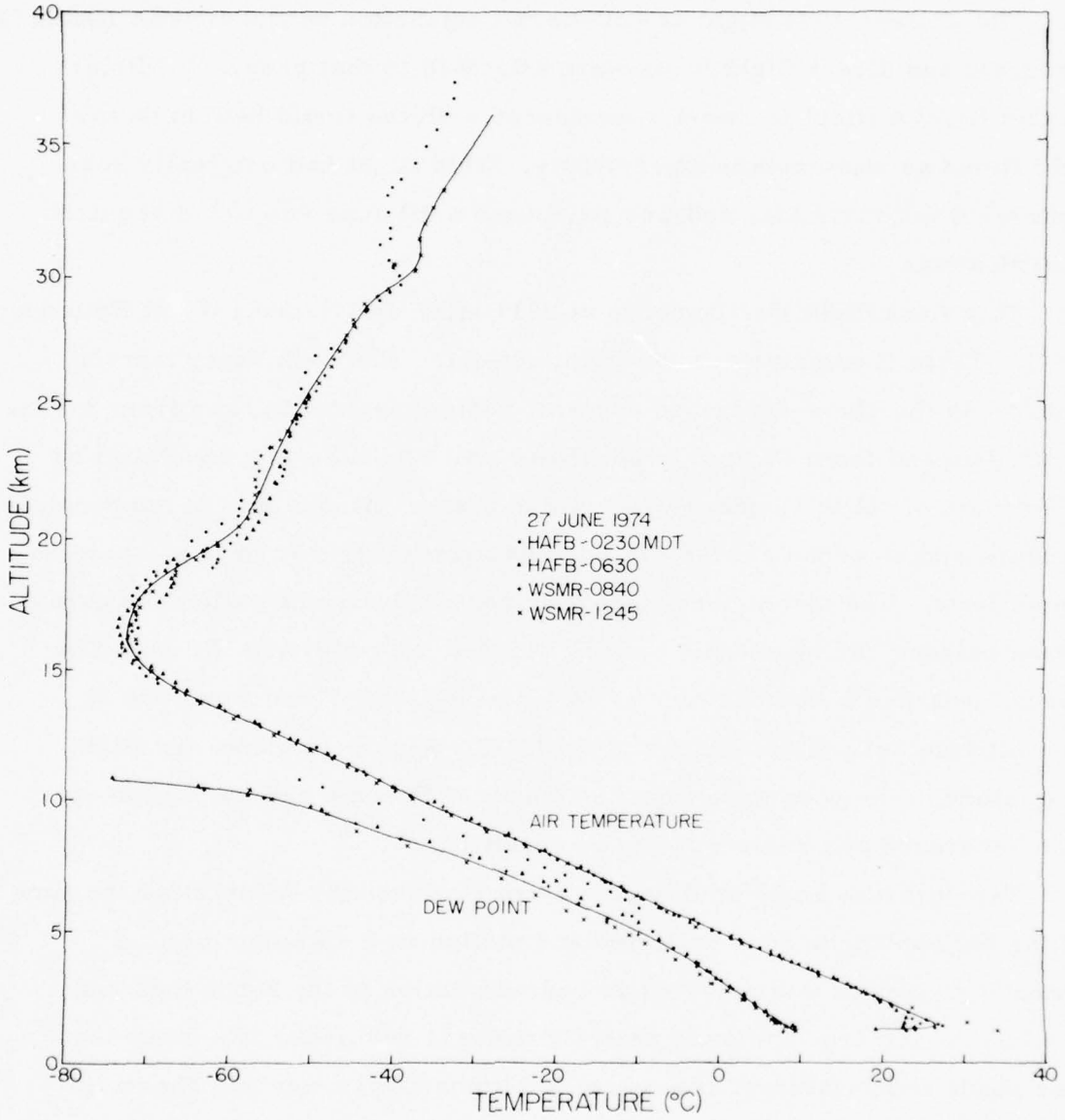

Figure 11. Plot of air temperature vs altitude for 27 June 1974 including data from several rawinsondes and also showing dew point.

The spectral radiometer worked throughout the flight and data from both wavelength regions were recorded on tape. Three elevation scans were made at float altitude. Several minor problems in the instrument performance caused a considerable delay in the data reduction process. The principal problems were cross-talk between pre-amps, resonant microphonics (both discussed later), variability in wavelength drive due to variable ground currents in the tachometer lead and warming of the outside surface of the vacuum dewar at float altitude causing an increase in the radiance reflected from the window into the spectrometer.

Usable data were obtained from one of the three auxiliary experiments, the NASA ozone sensor. The ozone altitude profile derived from this experiment was supplied by Ernest Hilsenrath, Upper Atmosphere Branch, Goddard Space Flight Center and is shown in Table III.[2] This table contains the O_3 mixing ratio from the flight data and from an average of 17 rocket sondes flown at mid-latitude during the day.[3] According to Dr. Hilsenrath, there is no significant change in the mixing ratio during float. He also indicates that it is difficult to estimate the errors in the measurement since the vacuum chamber tests with the aspirator were not conclusive above 36.5 km. Additional errors could also be due to losses in the plumbing at high altitudes that could not be accounted for in the data reduction. In either case, these errors would tend to under-measure the ambient ozone by as much as 20% above 36.5 km. Below this altitude the measurement should be as good as the optical measurement itself, which is about $\pm$ 5%.

---

[2]E. Hilsenrath and T. A. Ashenfelter, "A Balloon Ozone Measurement Utilizing an Optical Absorption Cell and an Ejector Air Sampler," NASA Technical Note No. NASA TN D-8281, Goddard Space Flight Center, Greenbelt, Md. 20771, July 1976.

[3]A. J. Krueger, "The Mean Ozone Distribution of Several Series of Rocket Soundings to 52 km at Latitudes from 58°S to 64°N", Pure Appl. Geophys. 106-108, 1272-1280, 1973.

Table III. NASA Ozone Profile

Alt (km)	Balloon Ozone Monitor 27 June 1974 μgm/gm	Standard Atmosphere Mid-Latitude 17 Rocket Sondes μgm/gm
17.0	0.63	
17.5	0.97	
18.0	1.52	2.65
18.5	2.29	
19.0	3.16	
19.5	3.00	
20.0	3.57	4.27
20.5	4.48	
21.0	4.87	
21.5	5.20	
22.0	5.52	6.00
22.5	6.23	
23.0	6.73	
23.5	7.36	
24.0	8.23	7.77
24.5	8.65	
25.0	9.73	
25.5	10.3	
26.0	11.0	9.39
26.5	11.5	
27.0	11.9	
27.5	12.0	
28.0	12.6	10.2
28.5	13.1	
29.0	12.6	
29.5	12.8	
30.0	12.9	10.9
30.5	13.2	
31.0	13.1	
31.5	12.8	
32.0	12.9	11.9
32.5	12.9	
33.0	12.7	
33.5	13.2	
34.0	12.3	12.7
34.5	12.9	
35.0	13.4	
35.5	12.6	
36.0	12.1	13.4
36.5	13.1	
37.0	11.7	
37.5	11.4	
38.0	10.6	13.0

The ASL ozone instrument did not function properly but the reason for this is unclear. The temperature sensors operated properly, but apparently the convective and radiative environment around such a large balloon payload preclude making a true air temperature measurement.

A summary of the atmospheric parameters for each spectral scan of the spectral radiometer is included in Table IV. The table includes an identification number for each scan, time altitude, pressure, angle of observation of incident radiance, atmospheric temperature from Figure 11, an apparent window reflectance temperature and an assumed window temperature. The window temperature sensing circuit suffered from the same ground current problems as the tachometer, thus negating the measurement on this flight.

B. 19 February 1975 Flight

The 19 February 1975 flight was flown as a test flight for a group of instruments to be flown in Alaska in April and May of 1975. The assembled gondola ready for flight is shown in Figure 12. The experiments on board included the spectral radiometer, a four field of view filter radiometer, the ASL temperature sensors, ASL ozonesonde, an X-ray sensor designed and built by James Barcus of the University of Denver, and 1.27μm O_2 ($^1\Delta_g$) radiometer designed and built at the University of Denver.

The balloon was launched at 0342 MST and reached a float altitude of 29.1 km at 0552 MST. The payload of 726 kg and balloon of 456 kg floated eastward until 1258 MST when the flight was terminated. Figure 13 shows a plot of the flight trajectory. The parachute impacted 10 miles east of Big Springs, Texas. The instruments were returned in good condition and prepared for shipment to Alaska after the necessary modifications. A summary of the flight and instrument parameters is listed in Table V. Temperature and dew point height profiles were collected from ascents made at times near those of the balloon flight. Plots of these data and the assumed average profiles are shown in Figure 14.

Table IV. Table of Parameters for Individual Scans for the Flight of 27 June 1974.

Record No.	Time (MST)	Alt (kft)	Alt (km)	Press (mb)	Zenith Angle (°)	Air Temp (°K)	Skin Temp (°K)	Window Temp (°K)
60	0740	32.8	10.0	288.	63.0	236.7	308.	80
64	0743	36.1	11.0	249.	63.0	230.0	306.	80
69	0747	39.4	12.0	214.	63.0	223.1	304.	80
73	0750	42.7	13.0	183.	63.0	215.3	301.	80
78	0753	45.9	14.0	157.	63.0	208.5	294.	80
82	0756	49.2	15.0	133.	63.0	203.5	289.	80
86	0759	52.5	16.0	112.	63.0	201.0	281.	80
94	0804	55.8	17.0	95.0	63.0	201.2	271.	80
102	0809	59.1	18.0	80.9	63.0	203.5	262.	80
105	0814	62.3	19.0	68.8	63.0	207.5	258.	80
111	0819	65.6	20.0	58.5	63.0	212.8	251.5	80
116	0824	68.9	21.0	49.9	63.0	215.8	250.4	80
119	0827	72.2	22.0	42.6	63.0	217.5	250.1	80
127	0831	75.5	23.0	36.4	63.0	218.8	250.2	80
132	0835	78.7	24.0	31.2	63.0	220.2	250.5	80
135	0838	82.0	25.0	26.6	63.0	222.1	250.7	80
142	0842	85.3	26.0	22.8	78.0	224.3	251.0	80
147	0846	88.6	27.0	19.6	78.0	226.3	251.4	80
152	0849	91.9	28.0	16.8	78.0	228.4	251.7	80
156	0852	95.1	29.0	14.6	78.0	230.5	252.2	80
160	0856	98.4	30.0	12.5	78.0	234.8	252.6	80
168	0900	101.7	31.0	10.8	83.0	236.6	253.6	80
180	0906	108.3	33.0	8.0	83.0	239.2	256.0	80
191	0915	114.8	35.0	6.0	83.0	243.2	259.3	80
204	0922	121.4	37.0	4.5	83.0	246.0	263.5	80
226	0937	124.7	38.0	4.0	83.0	246.0	268.0	80
247	0952	124.7	38.0	4.0	83.0	246.0	270.3	80
275	1010	124.7	38.0	4.0	88.0	246.0	269.6	80
280	1021	124.7	38.0	4.0	93.0	246.0	269.5	80
283	1023	124.7	38.0	4.0	93.0	246.0	269.4	80
286	1025	124.7	38.0	4.0	93.0	246.0	269.4	80
289	1028	124.7	38.0	4.0	93.0	246.0	269.3	80
292	1030	124.7	38.0	4.0	93.0	246.0	269.3	80
295	1032	124.7	38.0	4.0	93.0	246.0	269.2	80
298	1034	124.7	38.0	4.0	93.0	246.0	269.1	80
301	1036	124.7	38.0	4.0	93.0	246.0	269.0	80
304	1038	124.7	38.0	4.0	93.0	246.0	268.8	80
318	1046	124.7	38.0	4.0	48.0	246.0	268.5	80
346	1058	124.7	38.0	4.0	63.0	246.0	267.6	80
361	1114	124.7	38.0	4.0	78.0	246.0	267.3	80
375	1125	124.7	38.0	4.0	83.0	246.0	266.9	80
389	1135	124.7	38.0	4.0	88.0	246.0	266.4	80
396	1142	124.7	38.0	4.0	93.0	246.0	266.2	80
403	1147	124.7	38.0	4.0	93.0	246.0	266.0	80
490	1151	124.7	38.0	4.0	93.0	246.0	265.5	80

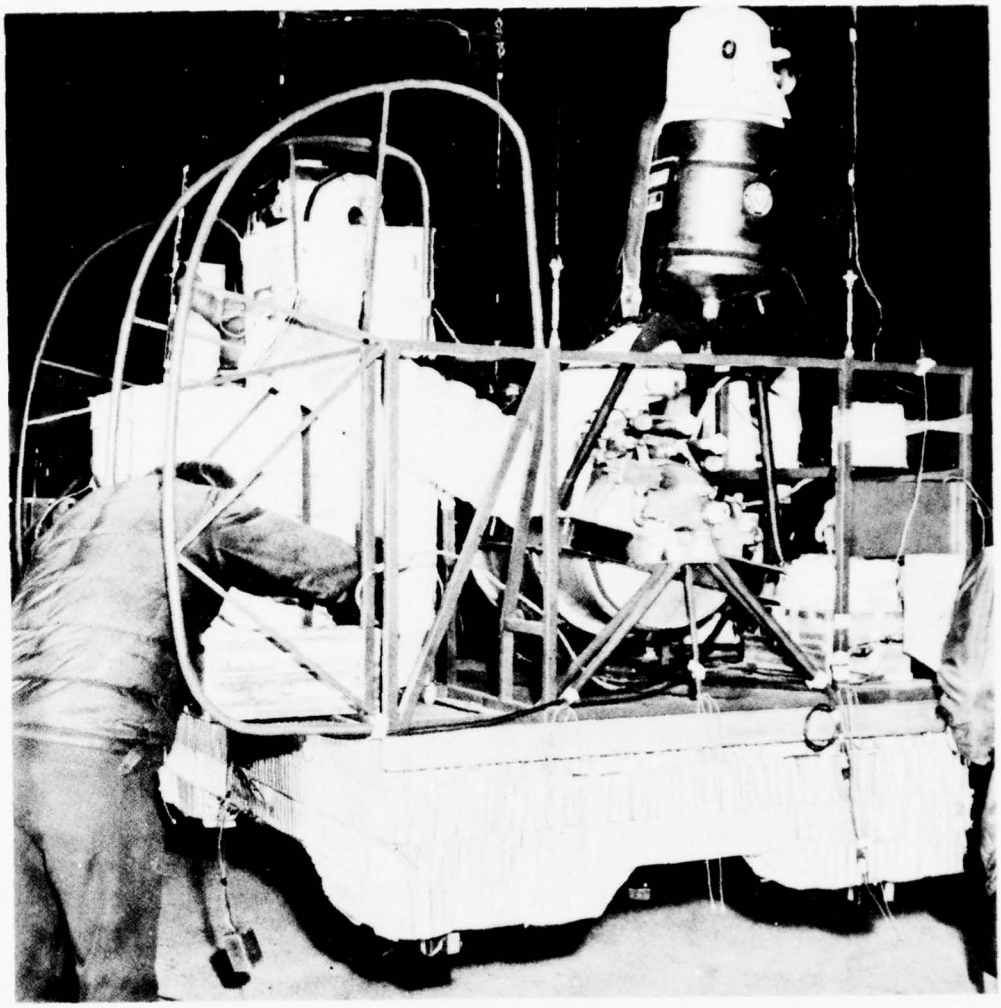

Figure 12. Photo of LHe Spectrometer mounted in gondola ready for flight.

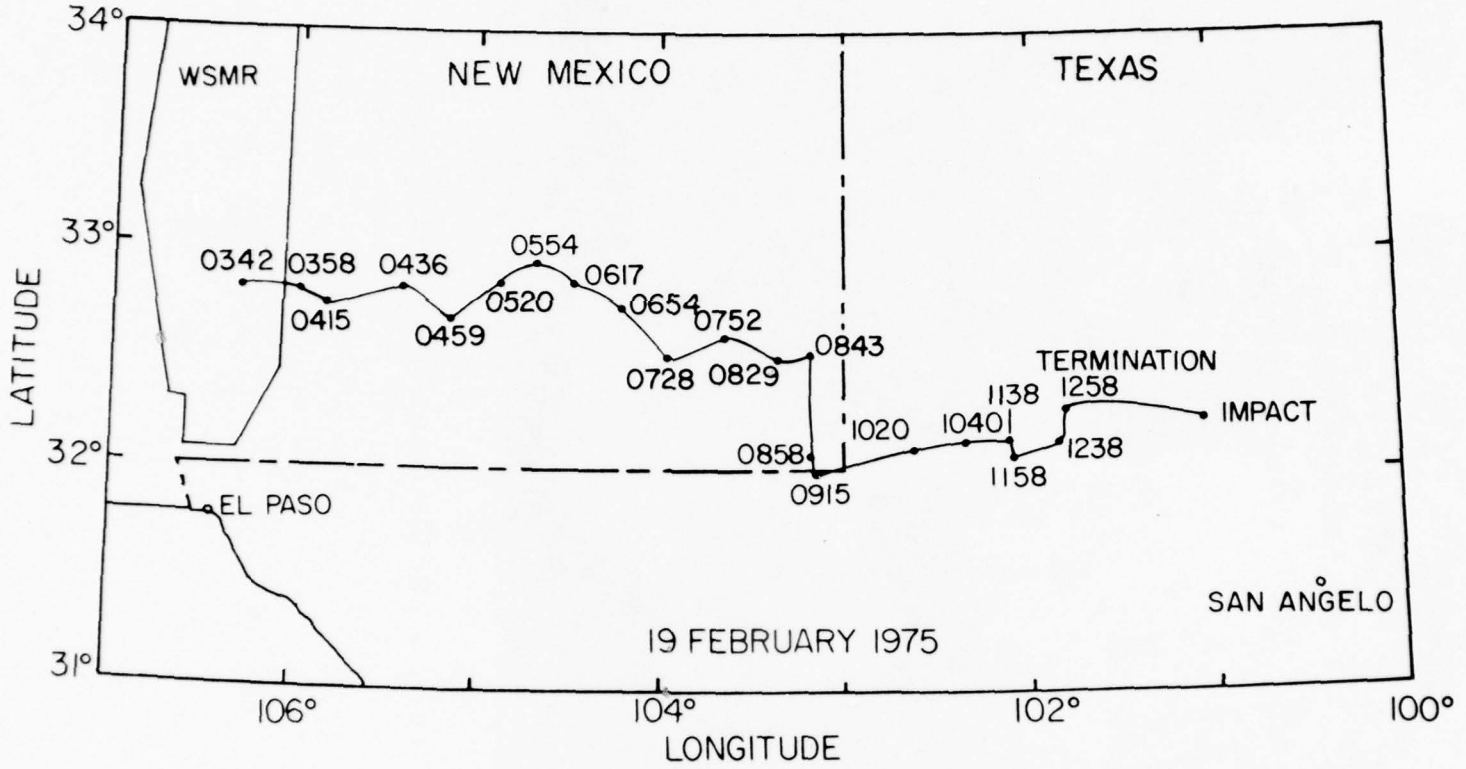

Figure 13. Plot of Balloon Flight trajectory for 19 February 1975.

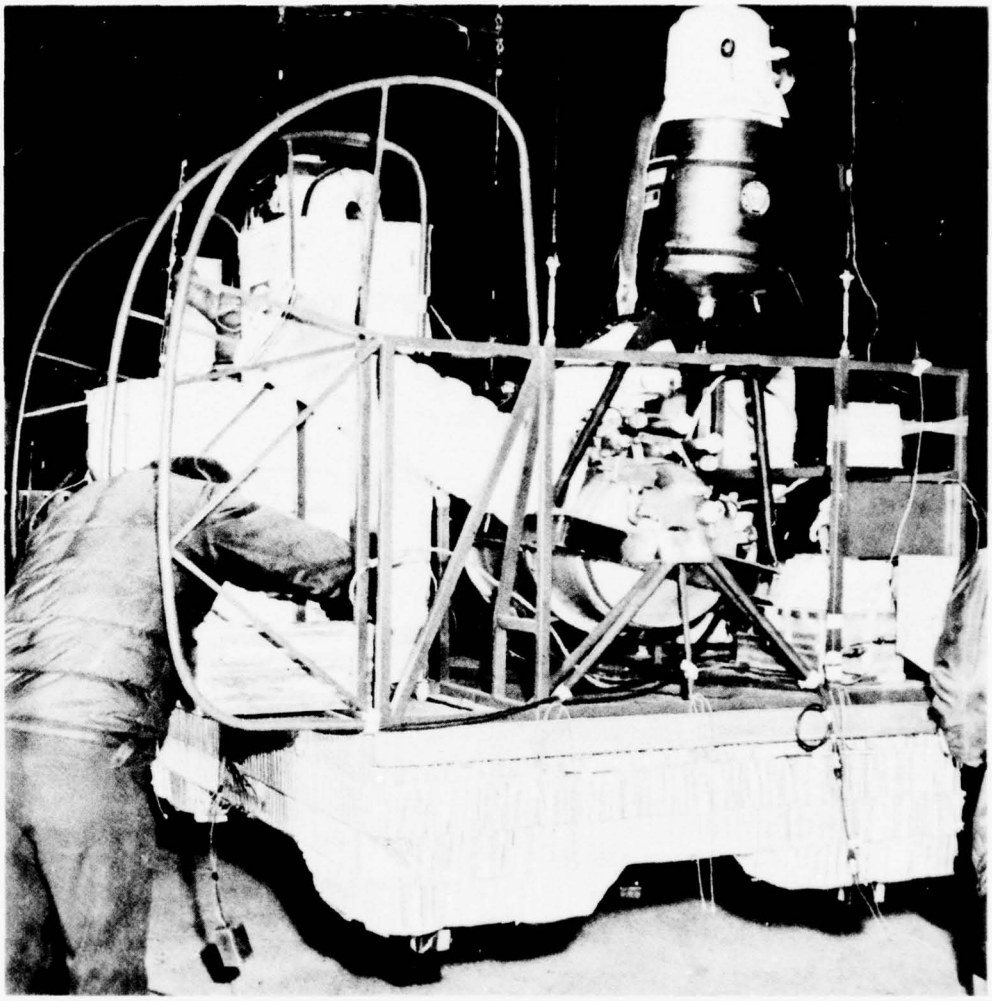

Figure 12. Photo of LHe Spectrometer mounted in gondola ready for flight.

Table V. Flight and Instrument Parameters

19 February 1975 Flight

Flight Date: 19 February 1975

Location: Holloman AFB, New Mexico

Primary Instruments:
1. Liquid helium cooled spectrometer with cold window.
2. 4 detector LN_2 radiometers.

Auxiliary Instruments:
1. A.S.L. Temperature Sensors
2. A.S.L. Ozone Sensors
3. X-ray (Barcus)
4. 1.27μm Radiometer

Purpose of Flight: Test instrumentation for Alaska series in April and May 1975. To measure minor atmospheric constituent height profiles.

Time Log:

Launch	0342MST
Float	0552MST (29.1 km)
Cut Down	1258MST

LHe Spectrometer Parameters:

Window Material	KRS 5	
Scan Time	43 sec	
λ Equation	$n\lambda = 50 \sin[8.60 \times 10^{-4} \frac{a}{.5580}(char) + 18.79]$	
Grating Order	2	1
λ Range	8.10-13.60μm	18.00-27.20μm
Resolution	.03μm	.06μm
Sample Interval	.005μm	.01μm
Detector Bias	+ 18v	+18v
Amplifier Gain	2.83/113.2	2.83/113.2
Band Pass	12.5Hz	12.5Hz
NER (Realized during flight)	$4 \times 10^{-8} wcm^{-2} sr^{-1} \mu m^{-1}$	$3 \times 10^{-8} wcm^{-2} sr^{-1} \mu m^{-1}$

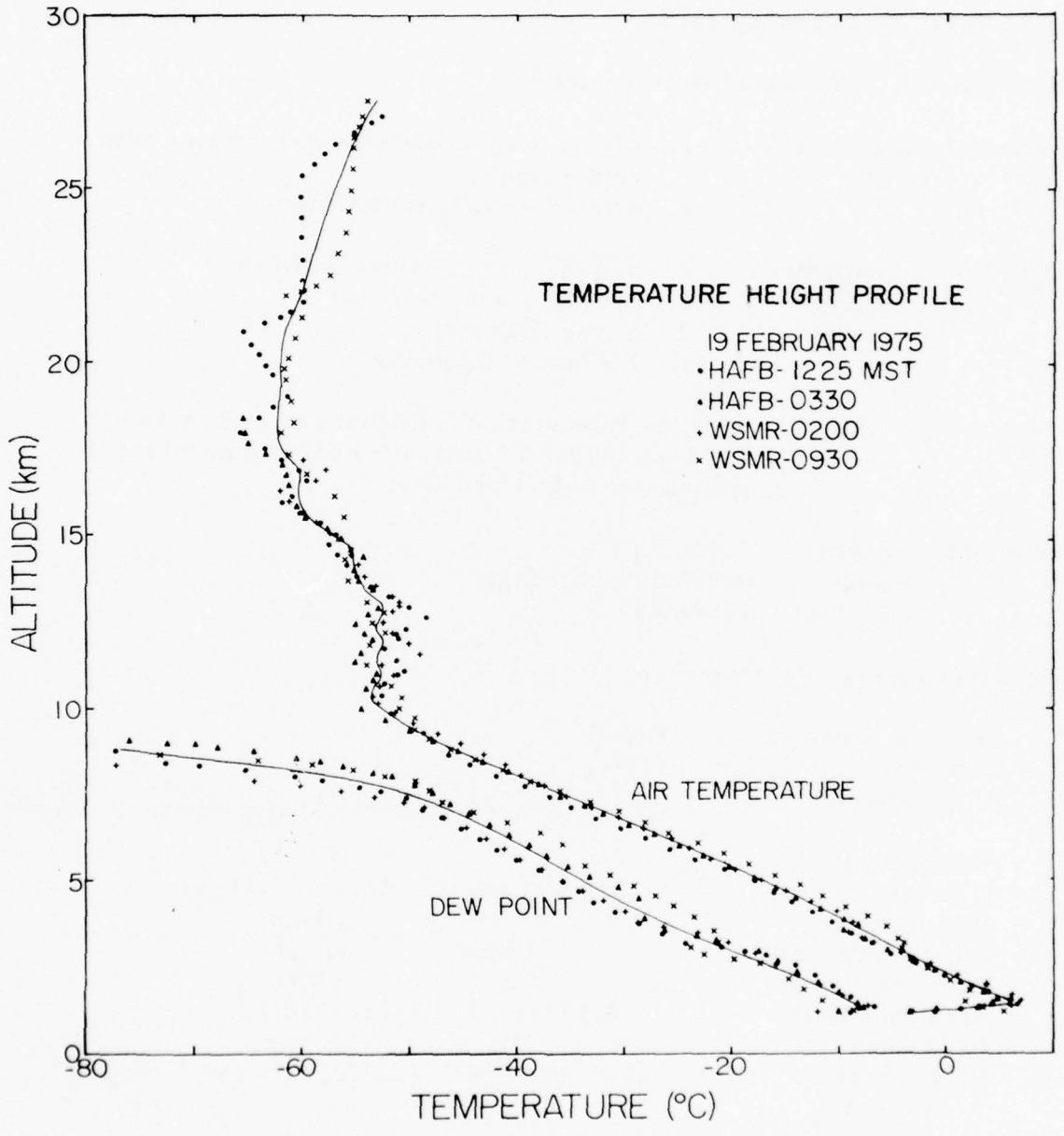

Figure 14. Plot of air temperature vs altitude for 19 February 1975 including data from several rawinsondes and also showing dew point.

The spectral radiometer operated successfully during the entire flight. However, many of the same minor problems present in the June data plagued the data reduction process. Apparently the problems had not been completely identified. In most instances the magnitude of the problem had been significantly reduced, but better solutions were required before flying in Alaska. The filter radiometer lost sensitivity shortly after launch so no useful data were obtained: apparently the detector had run out of liquid helium. The ASL Ozonesonde did not obtain a meaningful measurement and the temperature sensors still read high. This approach for measuring local air temperature was abandoned after this flight. The X-ray monitoring instrument operated properly and measured appropriate background levels, but these data are not directly of interest and are not presented here. Any perturbed X-ray data from Alaska will be reported. The 1.27μm radiometer stopped operating during ascent apparently due to cold electronics.

A summary of the atmospheric parameters for the spectral radiometer for the February flight are shown in Table VI. Spectral scan identification numbers are contained in the first two columns. These are associated with the two recorders flown as part of the balloon instrumentation. The other columns are identified the same as for the June flight.

Table VI. Table of Parameters for Individual Scans for the Flight of February 1975.

Record No.(#2)	Record No.(#3)	Time (MST)	Alt (kft)	Alt (km)	Press (mb)	Zenith Angle (^{o})	Air Temp (^{o}K)	Skin Temp (^{o}K)	Window Temp (^{o}K)
46	47	0401	18.0	5.5	504.	63.0	251.9	242.5	80
49	50	0403	19.7	6.0	472.	63.0	248.6	240.2	80
52	53	0405	21.3	6.5	439.	63.0	245.2	238.2	80
55	56	0407	23.0	7.0	411.	63.0	241.2	236.0	80
58	59	0409	24.6	7.5	383.	63.0	237.6	234.0	80
61	62	0412	26.2	8.0	355.	63.0	233.7	232.5	80
64	65	0414	27.9	8.5	330.	63.0	230.5	231.8	80
67	68	0416	29.5	9.0	306.	63.0	226.7	228.8	80
70	71	0418	31.2	9.5	286.	63.0	223.2	227.0	80
72	73	0420	32.8	10.0	265.	63.0	220.2	225.6	80
74	75	0421	34.4	10.5	245.	63.0	219.5	224.3	80
76	77	0422	36.1	11.0	228.	63.0	220.6	223.0	80
78	79	0424	37.7	11.5	210.	63.0	219.6	221.5	80
87	85	0428	40.0	12.2	188.5	63.0	220.2	218.3	80
90	88	0429	41.0	12.5	179.7	63.0	219.6	214.5	80
96	92	0433	42.3	12.9	169.3	63.0	221.0	212.5	80
101	97	0436	44.3	13.5	153.6	63.0	219.6	209.0	80
104	100	0438	47.6	14.5	131.7	63.0	218.0	206.0	80
106	102	0440	49.2	15.0	121.4	63.0	215.6	205.2	80
110	105	0442	51.8	15.8	107.5	63.0	213.1	201.8	80
114	109	0445	54.1	16.5	96.3	63.0	212.3	198.6	80
118	113	0447	55.8	17.0	88.5	63.0	211.4	196.0	80
120	115	0449	57.7	17.6	81.2	63.0	209.0	194.5	80
123	118	0451	59.1	18.0	76.0	63.0	208.7	192.2	80
126	121	0453	61.0	18.6	69.3	63.0	208.4	189.8	80
129	124	0456	63.0	19.2	63.2	63.0	208.2	187.0	80
131	126	0457	64.3	19.6	59.6	63.0	208.2	185.0	80
134	129	0459	65.6	20.0	55.7	63.0	208.2	182.7	80
138	133	0501	67.3	20.5	51.7	63.0	208.2	179.8	80
141	136	0504	68.9	21.0	47.7	63.0	208.2	177.8	80
144	139	0506	70.5	21.5	44.1	63.0	208.2	175.9	80
147	142	0508	71.9	21.9	41.5	63.0	208.2	174.2	80
152	147	0511	73.8	22.5	37.8	63.0	208.2	172.5	80
154	149	0513	75.5	23.0	35.0	63.0	208.2	171.9	80
158	152	0516	77.1	23.5	32.4	63.0	208.2	171.2	80
163	157	0518	78.7	24.0	29.9	63.0	208.2	170.3	80
166	160	0521	80.7	24.6	27.2	63.0	208.2	170.0	80
169	163	0524	82.3	25.1	25.0	63.0	208.2	169.8	80
172	166	0525	83.7	25.5	23.7	63.0	208.2	169.2	80
176	170	0528	85.3	26.0	21.9	63.0	208.2	169.0	80
180	174	0531	86.9	26.5	20.3	63.0	208.2	168.8	80
183	177	0533	88.3	26.9	19.0	63.0	208.2	168.6	80

Table VI. Table of Parameters for Individual Scans for the Flight of February 1975. (Continued)

Record No. (#2)	Record No. (#3)	Time (MST)	Alt (kft)	Alt (km)	Press (mb)	Zenith Angle (^{o})	Air Temp (^{o}K)	Skin Temp (^{o}K)	Window Temp (^{o}K)
188	182	0537	90.2	27.5	17.3	63.0	208.5	168.0	80
193	187	0540	91.9	28.0	16.0	63.0	208.8	167.3	80
196	190	0542	92.5	28.2	15.5	63.0	209.0	166.9	80
199	193	0545	93.8	28.6	14.7	78.0	209.3	166.3	80
202	196	0547	94.5	28.8	14.2	78.0	209.5	166.0	80
204	198	0548	95.1	29.0	13.8	78.0	209.6	165.3	80
207	201	0550	95.5	29.1	13.5	78.0	209.7	164.9	80
208	202	0551	95.5	29.1	13.5	83.0	209.7	164.7	80
213	207	0554	95.5	29.1	13.5	88.0	209.7	163.9	80
215	209	0556	95.5	29.1	13.5	93.0	209.7	163.4	80
221	215	0559	95.5	29.1	13.5	81.0	209.7	162.1	80
229	222	0604	95.5	29.1	13.5	81.0	209.7	161.0	80
242	235	0608	95.5	29.1	13.5	81.0	209.7	158.4	80
255	248	0614	95.5	29.1	13.5	81.0	209.7	156.4	80
263	256	0621	95.5	29.1	13.5	81.0	209.7	155.2	80
279	271	0636	95.5	29.1	13.5	81.0	209.7	155.0	80
290	282	0645	95.5	29.1	13.5	81.0	209.7	155.2	80
308	300	0652	95.5	29.1	13.5	81.0	209.7	157.0	80
358	350	0718	95.5	29.1	13.5	81.0	209.7	164.0	80
408	400	0754	95.5	29.1	13.5	81.0	209.7	169.5	80
458	450	0830	95.5	29.1	13.5	81.0	209.7	173.5	80
	500	0905	95.5	29.1	13.5	81.0	209.7	176.3	80
	550	0940	95.5	29.1	13.5	81.0	209.7	177.1	80
	600	1015	95.5	29.1	13.5	81.0	209.7	176.5	80
	689	1048	95.5	29.1	13.5	81.0	209.7	174.6	80
	764	1200	95.5	29.1	13.5	81.0	209.7	173.8	80

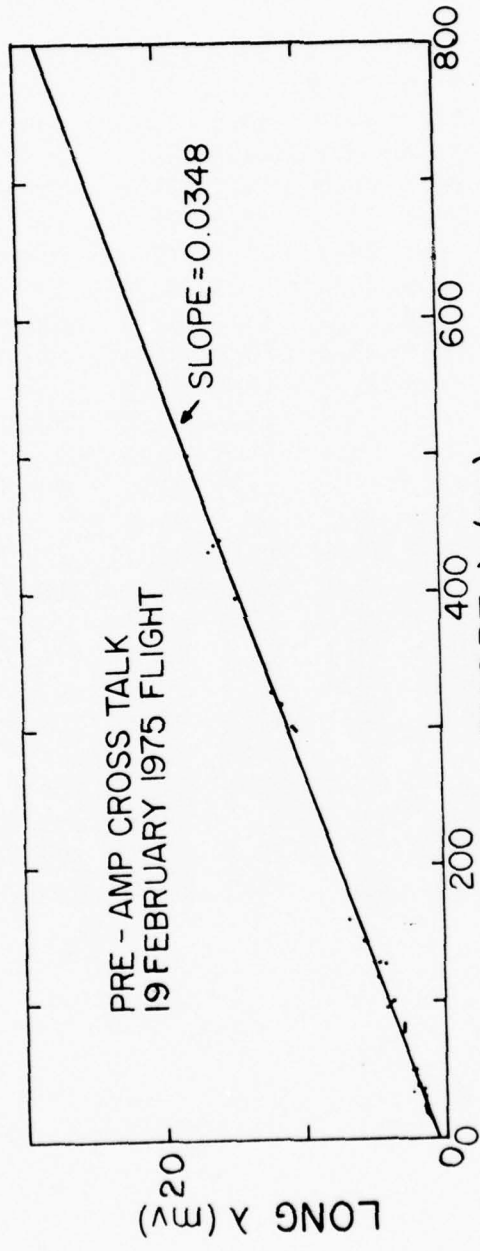

Figure 15. Plot of Electronic cross talk from short wavelength pre-amp to long wavelength pre-amp

V. DATA REDUCTION

The data reduction process is essentially the same for both flights except that specific constants may differ for each. The objective of the data reduction is to convert the recorded electrical voltages back to the original incident radiance with as much precision as possible. To accomplish this the recorded data must be examined for spurious content and, whenever possible, the undesired signal removed or compensated for. In addition the untreated data are examined for variations of the primary data reduction parameters such as wavelength and zero references (both optical and electrical). Of course, ideally there are no spurious inputs. In practice, with proper identification of such inputs in ground tests and during the first few flights, these inputs should be reduced to insignificant levels.

Before the June and February data were reduced to radiance, corrections had to be made for electrical cross talk between the pre-amps. The cross talk was not recognized until after the June flight because it was at relatively low levels ($\leq 10\%$) and unanticipated. It is important, however, because the radiance levels at complementary wavelengths of the first and second order of the grating are sometimes orders of magnitude apart. The cross talk mechanism was not properly identified after the June flight and was present but slightly reduced for the February flight. It has been eliminated to $< 0.1\%$ on all subsequent flights. Careful measurements were made of the effect prior to the February flight and in-flight data were used for the June flight. Figures 15 and 16 are plots of the pre-February measurements showing that the cross talk is linear with amplitude with a different magnitude from short wavelength to long ($\sim 3.5\%$) than from long wavelength to short ($\sim 6.3\%$). It was finally determined that there was a small capacitive coupling between the output of one pre-amp and the input of the other ($\sim .01$ pf) causing this cross talk. The solution was to shield about 3 cm of input lead.

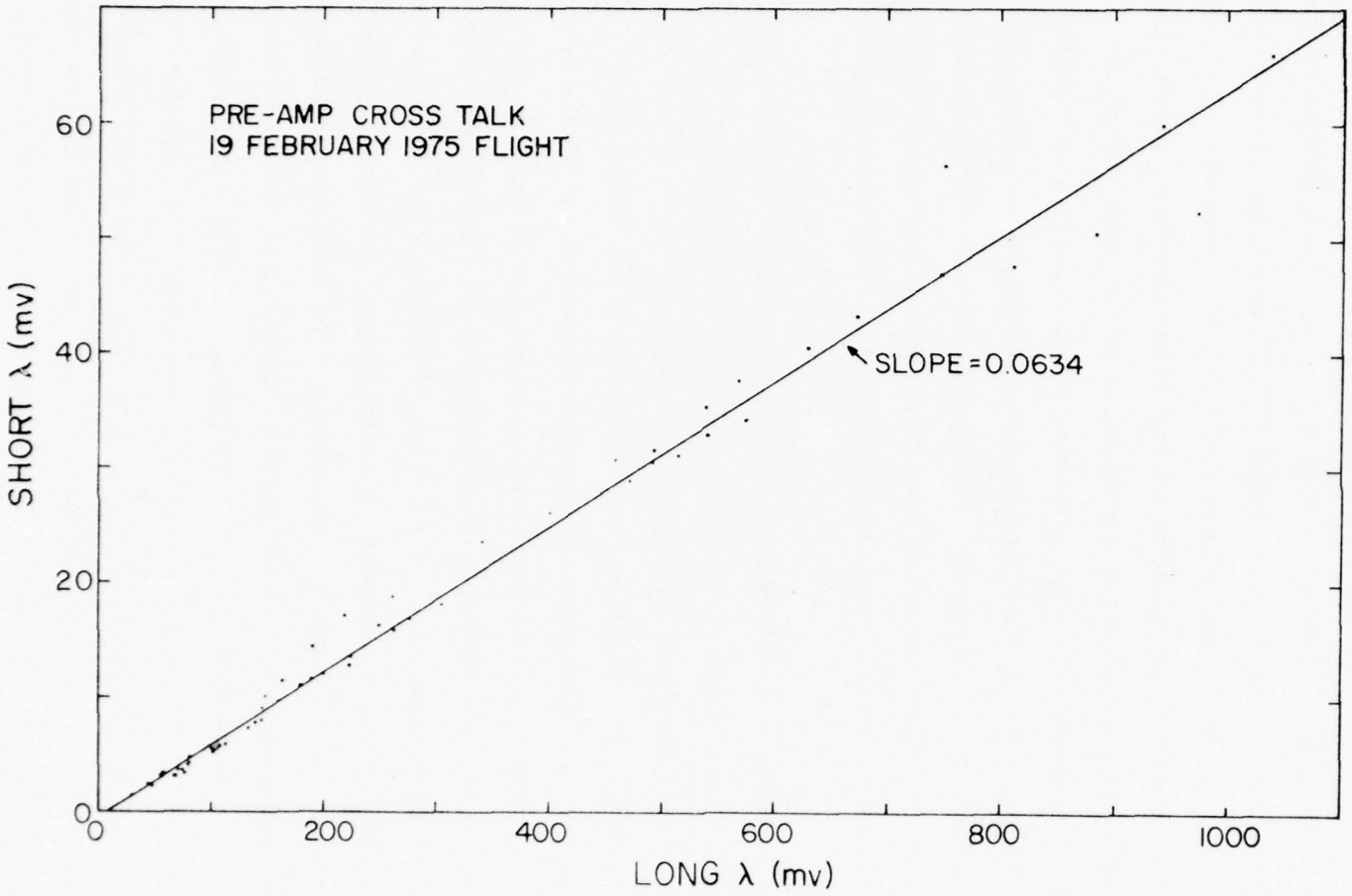

Figure 16. Plot of Electronic cross talk from long wavelength pre-amp to short wavelength pre-amp

Every effort was made to eliminate another persistent problem, microphonic noise due to vibrating detector leads. This problem has not yet been completely solved, although the level of the problem has been greatly reduced. The microphonics are partially related to the pre-amp suspension in its thermal box. Until recent changes this suspension has tended to loosen with repeated thermal cycles and with parachute impact shock. In addition, certain elevation angles of the instrument allowed more microphonic coupling than others. During ascent on the June flight this coupling developed a resonance at certain elevation angles resulting in what appeared as a constant frequency and amplitude. An example is shown in the first 10 seconds of Figure 17a. It was largely possible to remove this pseudo constant frequency from the data before further reduction (see Figure 17b).

Once the electrical artifacts are removed from the observed spectra, the voltage as a function of wavelength can be converted to spectral radiance. This process is basically the inverse of the calibration procedure and can be expressed in the following way:

$$N = KV^{*} - N_{W}^{*},$$

where V^{*} is the measured voltage corrected for cross talk, microphonics and zero references (both electrical and optical). N_{W}^{*} is the radiance correction for window emission and reflection. (Actually $N + N_{W}^{*}$ is initially calculated and a lengthy procedure is then followed to determine the most likely value for N_{W}^{*} for each spectral scan.)

The initial design of the spectral radiometer called for a cooled window with low emissivity such that $N_{W}^{*} \ll N$, particularly in the 10-12μm region. However, this condition was not realized until the sixth balloon flight with the spectrometer. (See Instrumentation, Optical Design.) Some method was therefore necessary to remove the radiance associated with the window (N_{W}^{*}) from the measured spectral radiance.

There are several sources of the radiance attributed to the window. The first is the emissivity due to the bulk window material and surface contamination. This is held to a minimum by cooling the window and

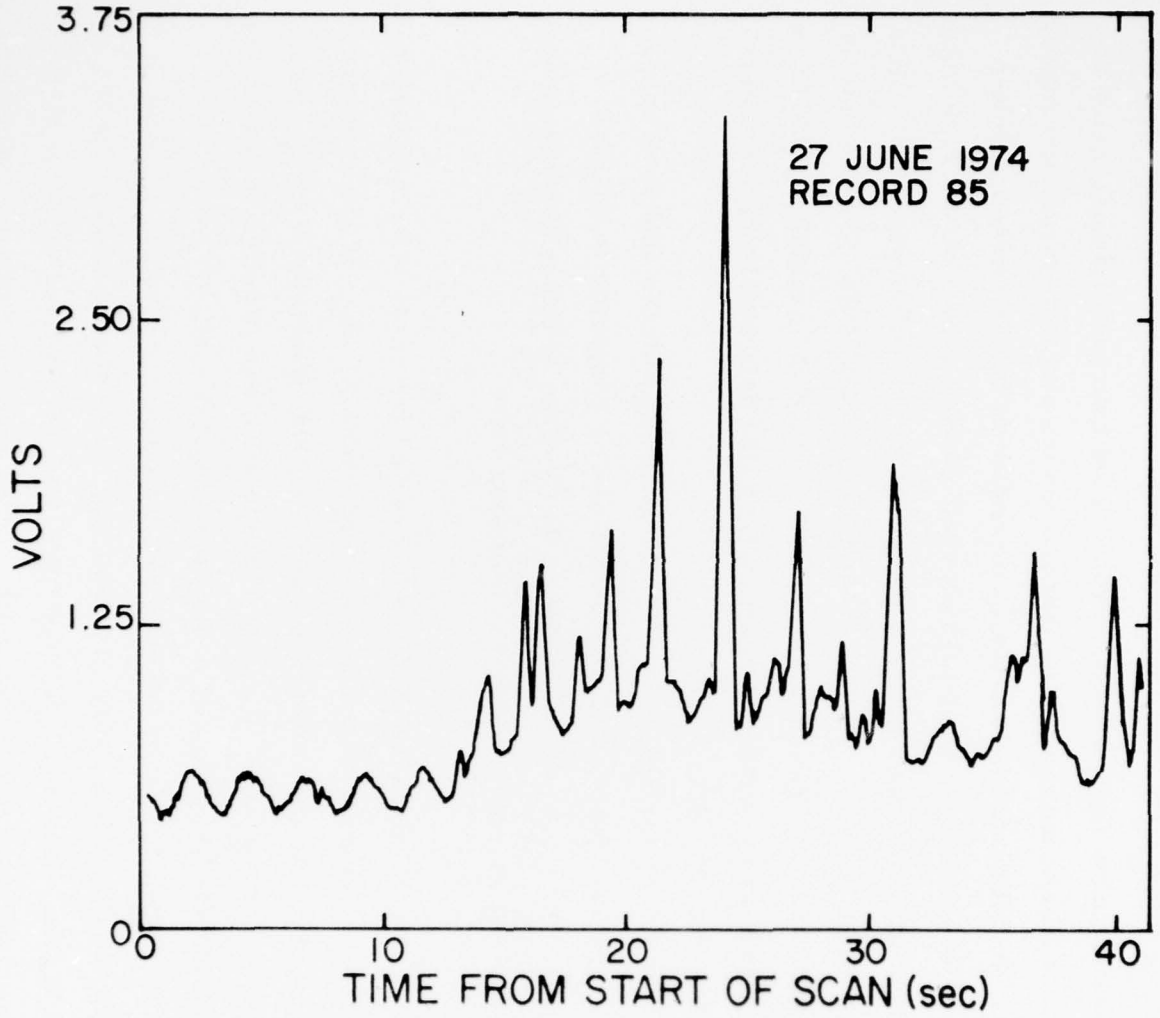

Figure 17a. Plot of unreduced and uncorrected spectrum (No. 85) from 27 June 1974

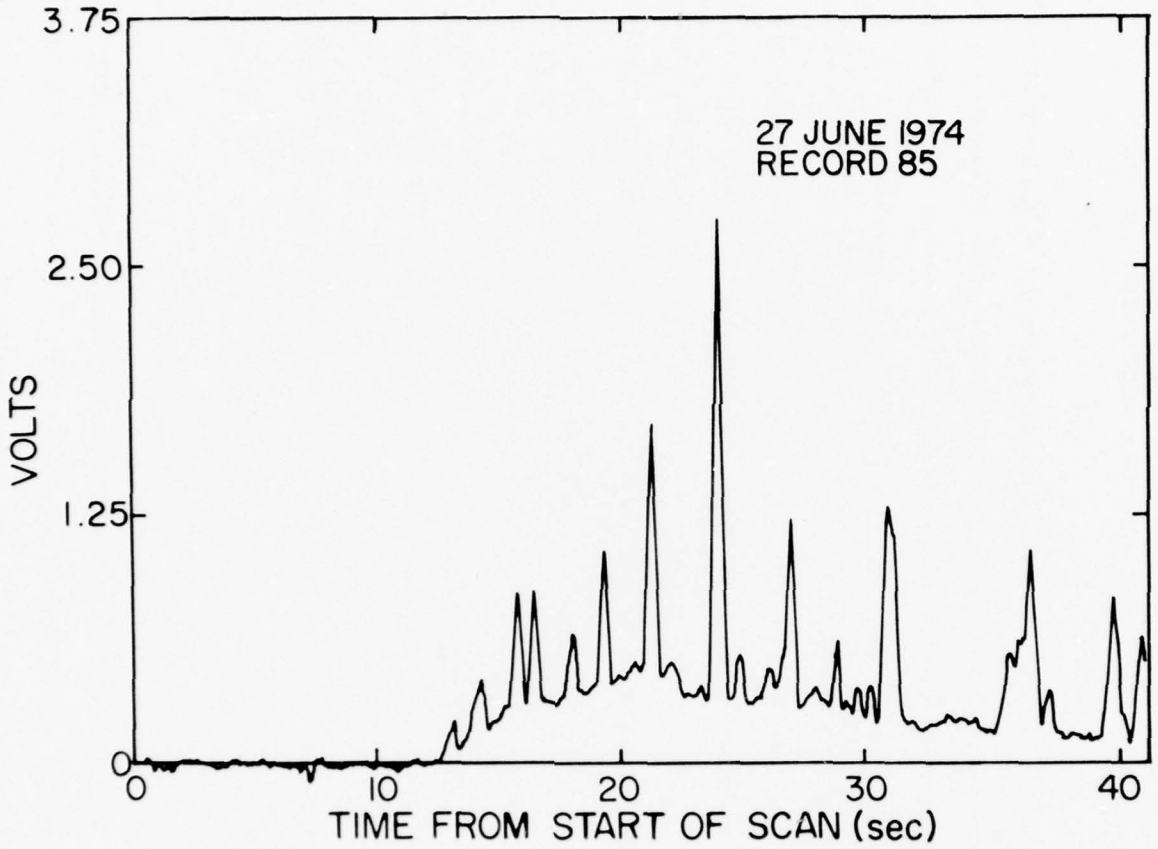

Figure 17b. Plot of unreduced spectrum (No. 85) of short wavelength region corrected for periodic noise.

selecting the window material. The second is the several sources of radiance reflected or scattered off the window into the optical path. With properly constructed and cooled baffles this source is also held to a minimum, but small openings in the baffle system can permit large fluxes of radiation from warm sources to be reflected into the optical path.

The window radiance for the February and June flights was related to radiance bypassing the baffle system. Further, the reflected radiance did not appear to be from a single temperature source where a single "gray" body correction could apply to all wavelengths. Nevertheless "gray" type corrections were attempted over shorter wavelength intervals where they represented a good approximation. These temperatures were calculated using the assumed residual radiance from pairs of wavelengths in the following fashion. Using the black body equation for radiance and taking the ratio of the radiance at two wavelengths and the same temperature,

$$\frac{N_1}{N_2}\frac{\lambda_1^5}{\lambda_2^5} = \frac{e^{c_2/\lambda_2 T} - 1}{e^{c_2/\lambda_1 T} - 1} .$$

Since we are looking for "gray" body temperatures, it is desirable to retain the ratio N_1/N_2 through the derivation. This can be accomplished and solved for the temperature by approximating $e^x - 1$ with e^x and is accurate to 5% for $\lambda T \leq 4800$ (μm K). Then solving for the temperature,

$$T = \frac{c_2(1/\lambda_2 - 1/\lambda_1)}{\ln \frac{N_1}{N_2}\left(\frac{\lambda_1}{\lambda_2}\right)^5} .$$

Temperatures derived in this fashion and tested against the measured data are listed in Tables IV and VI under the column labeled skin temperature. On later flights (Alaska 1975) the temperature of the spectrometer skin was actually measured and compared with this calculated temperature. The two temperatures seem to track in time with a constant offset, the calculated temperature being lower. Expressions for the window correction, N_W^*, for the two flights reported are:

$$N_W^* = 0.0013\ N(T_s) \text{ for 27 June 1974}$$

and

$$N_W^* = 0.008\ N(T_s) \text{ for 19 February 1975.}$$

It is important to remember that the purpose of the corrections for window-emission and reflection was not primarily to have good spectral window data, but rather to obtain good base line data in the regions where constituents of interest were emitting. Thus the required input on removing N_W^* is to limit the residual radiance error to < 10% of N in a constituent band. In addition it is desirable to limit this error to < 10% of N in the atmospheric windows to permit analysis of aerosol effects on long wavelength radiation. This criterion cannot be met here since assumptions were made as to the expected atmospheric window radiance in order to calculate T_s which was not measured on these flights. Consequently, for the two flights reported here, great care should be exercised in deriving conclusions from the fine detail of the height vs radiance profiles of the atmospheric window regions.

Once the window corrections are determined, the atmospheric radiance is calculated for all the spectral scans made during each flight. To facilitate presentation here and to reduce the noise somewhat, the spectral scans were grouped in uniform altitude increments and coadded. Samples of the resulting spectral radiance for the 27 June 1974 flight are shown in Figures 18 to 22 for the short wavelength region and Figures 23 to 27 for the long wavelength region. In addition, samples of the 19 February 1975 flight are shown in Figures 28 to 48 for the short wavelength region and Figures 49 to 71 for the long wavelength region.

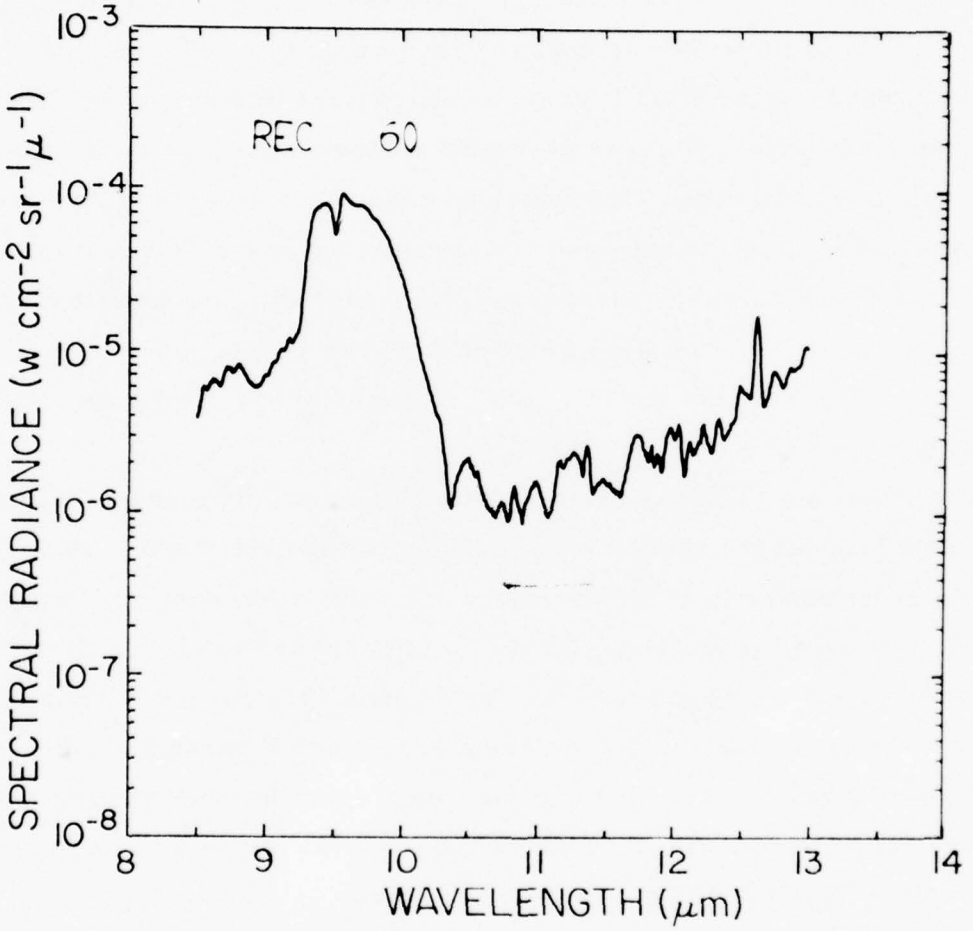

Figure 18. Sample spectrum of short wavelength region observed at an altitude of 10.0 km and a zenith angle of 63° on 27 June 1974.

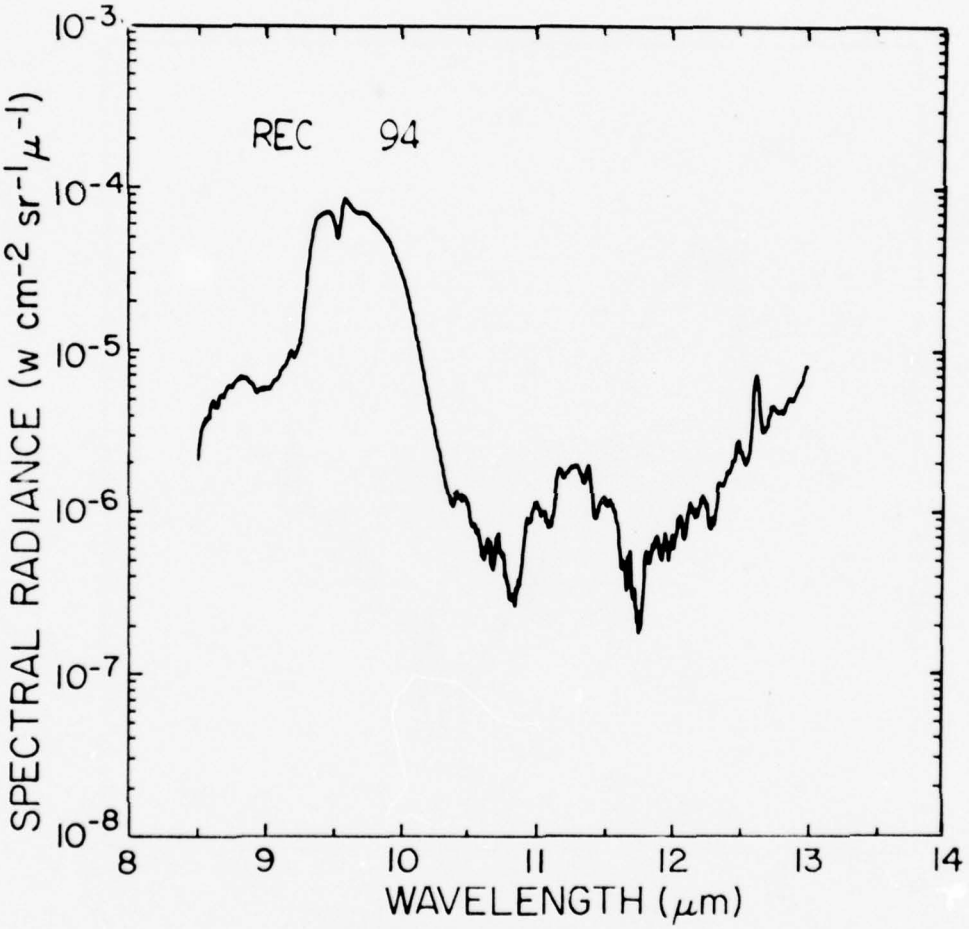

Figure 19. Sample spectrum of short wavelength region observed at an altitude of 17.0 km and a zenith angle of 63° on 27 June 1974.

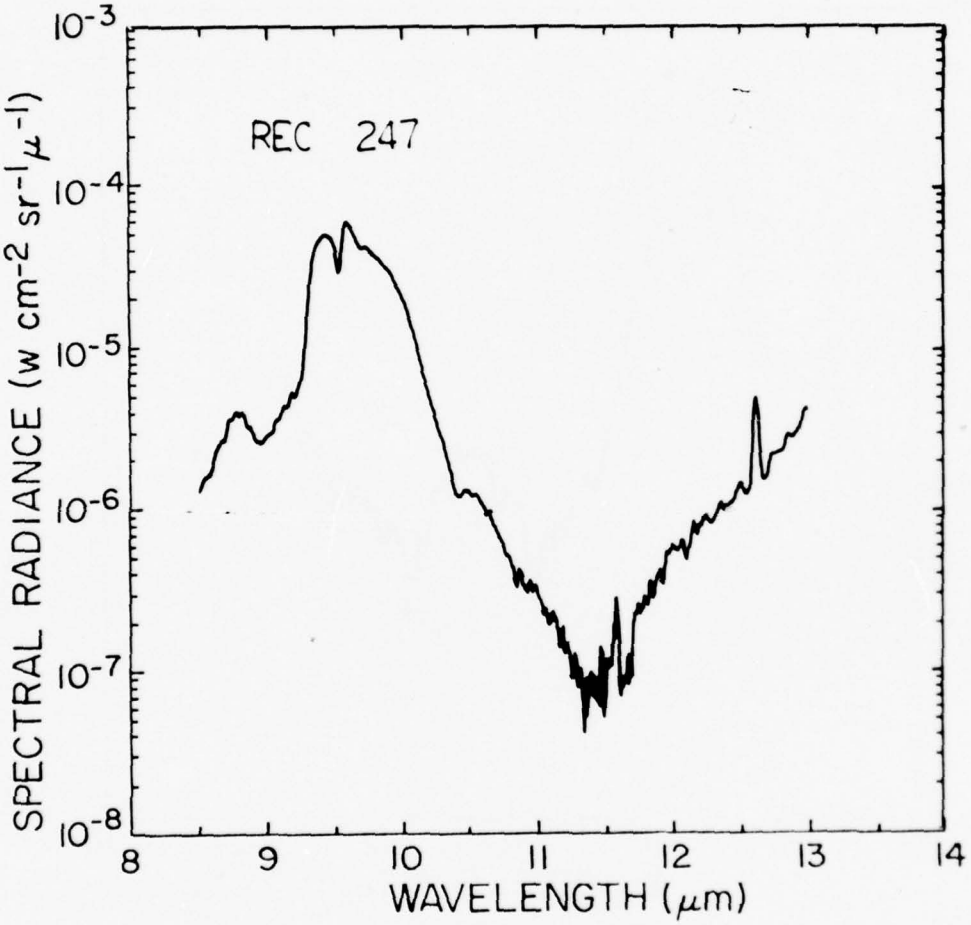

Figure 20. Sample spectrum of short wavelength region observed at an altitude of 38.0 km and a zenith angle of 83° on 27 June 1974.

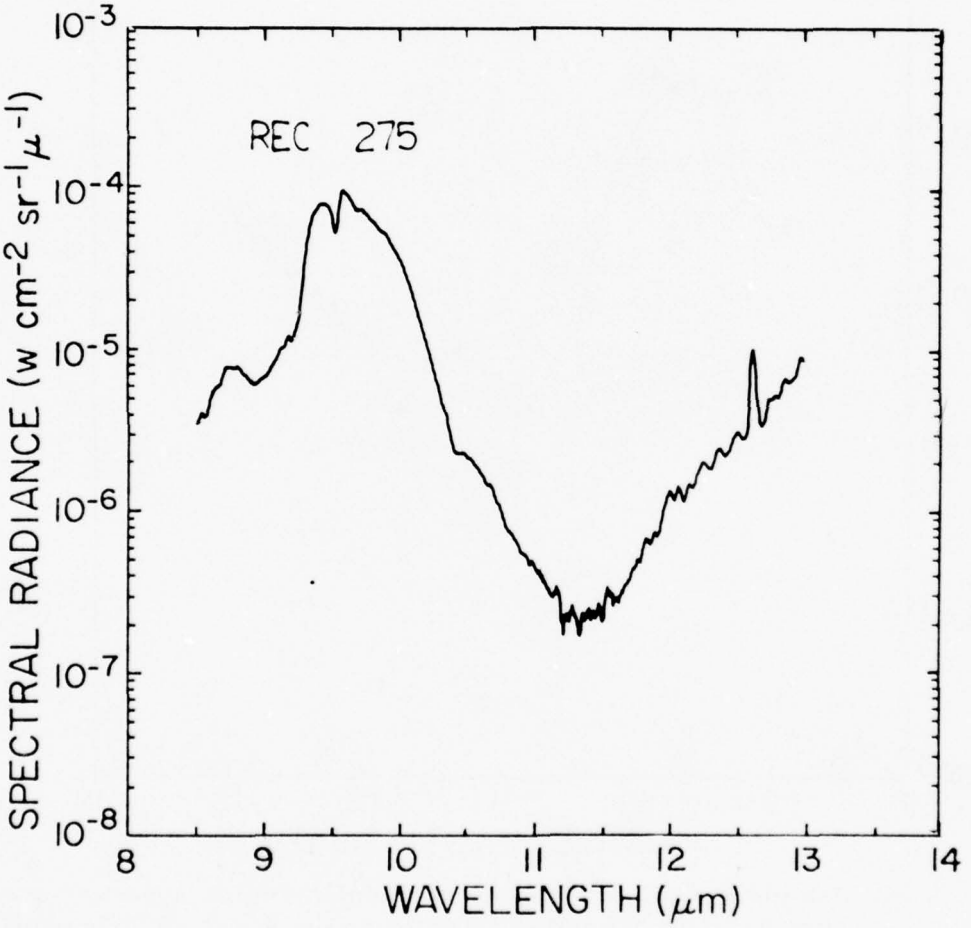

Figure 21. Sample spectrum of short wavelength region observed at an altitude of 38.0 km and a zenith angle of 88° on 27 June 1974.

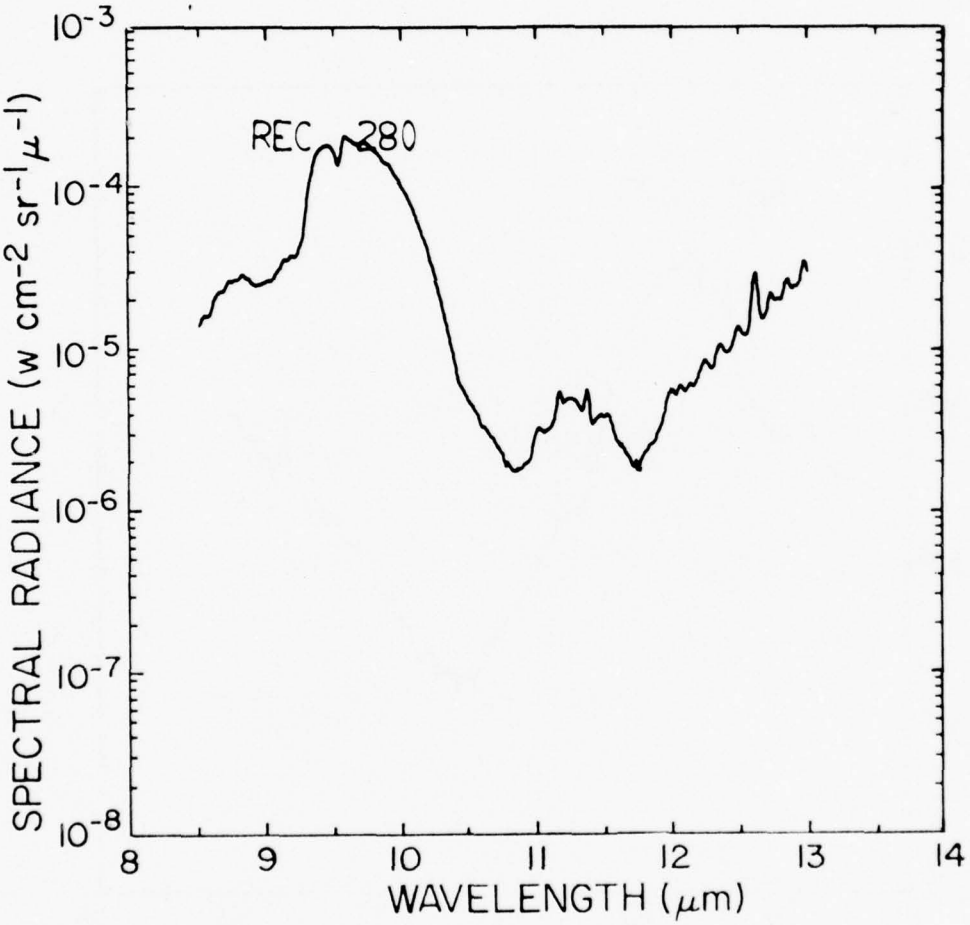

Figure 22. Sample spectrum of short wavelength region observed at an altitude of 38.0 km and a zenith angle of 93° on 27 June 1974.

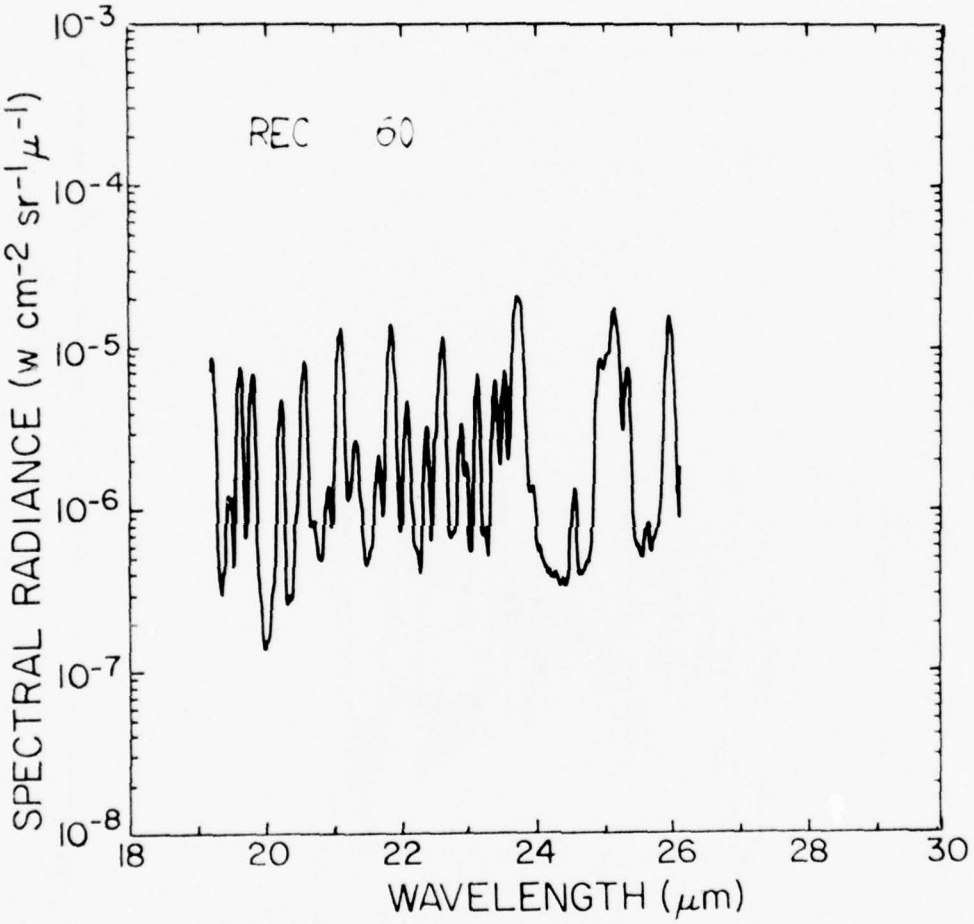

Figure 23. Sample spectrum of long wavelength region observed at an altitude of 10.0 km and a zenith angle of 63° on 27 June 1974.

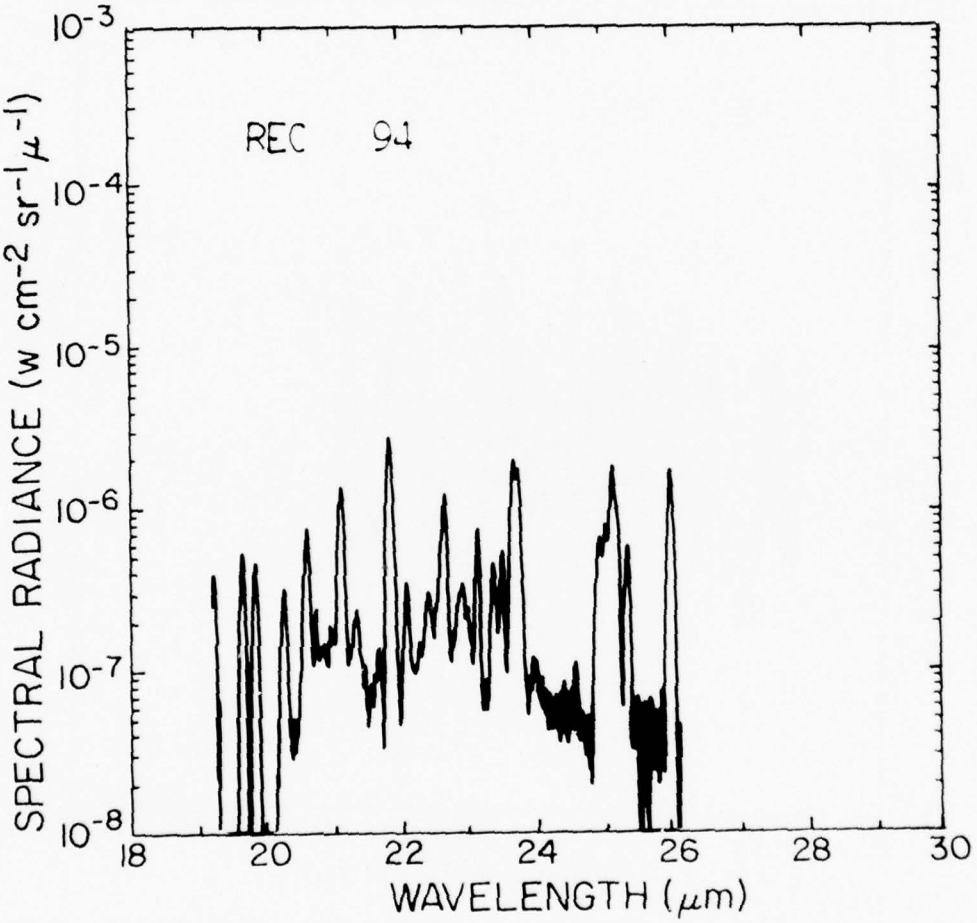

Figure 24. Sample spectrum of long wavelength region observed at an altitude of 17.0 km and a zenith angle of 63° on 27 June 1974.

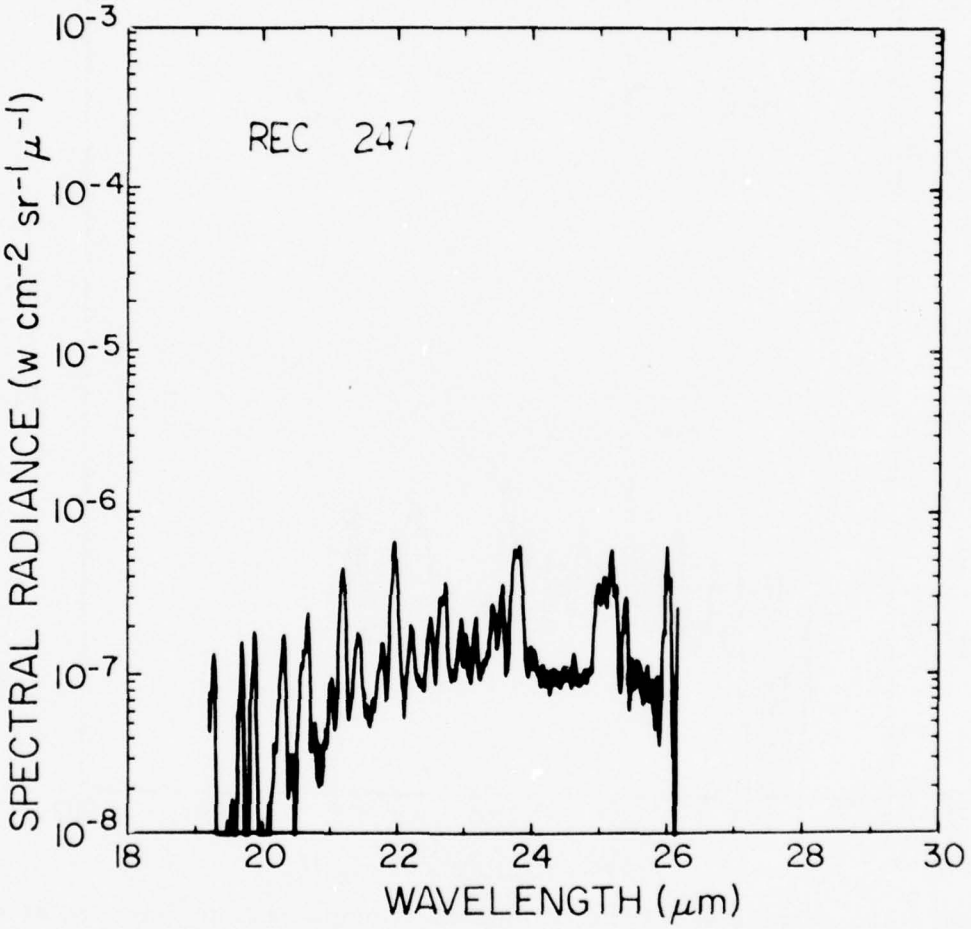

Figure 25. Sample spectrum of long wavelength region observed at an altitude of 38.0 km and a zenith angle of 83° on 27 June 1974.

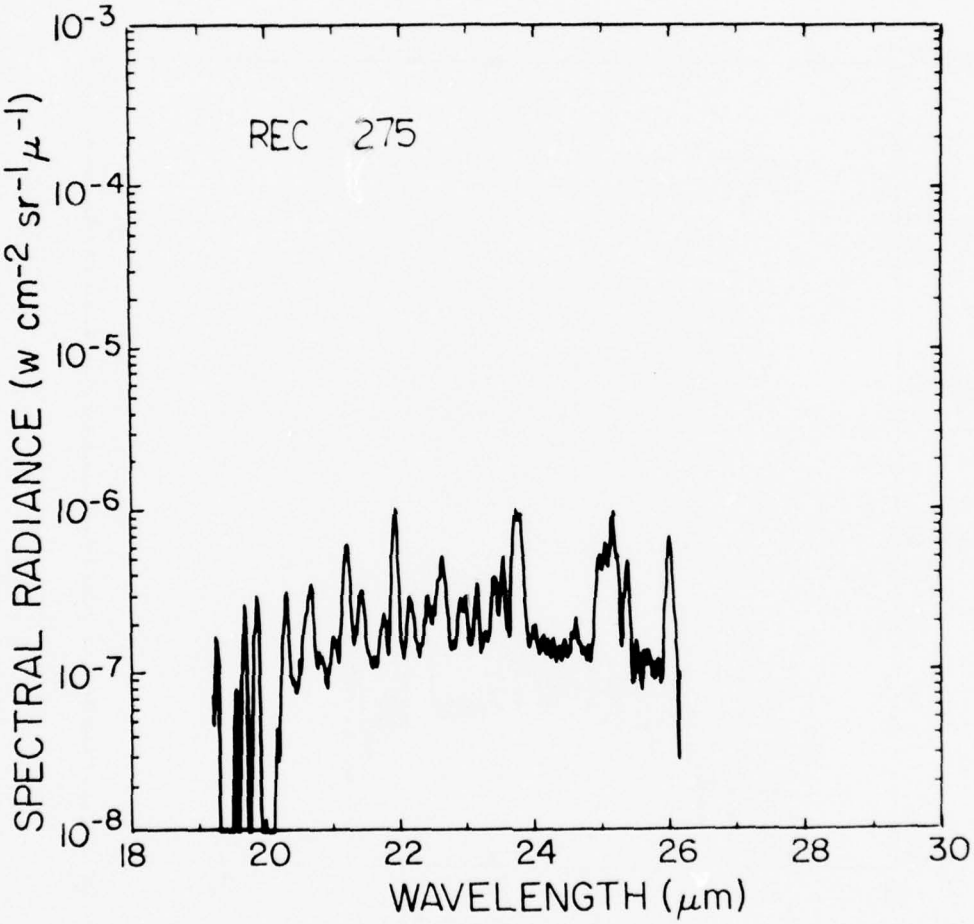

Figure 26. Sample spectrum of long wavelength region observed at an altitude of 38.0 km and a zenith angle of 88° on 27 June 1974.

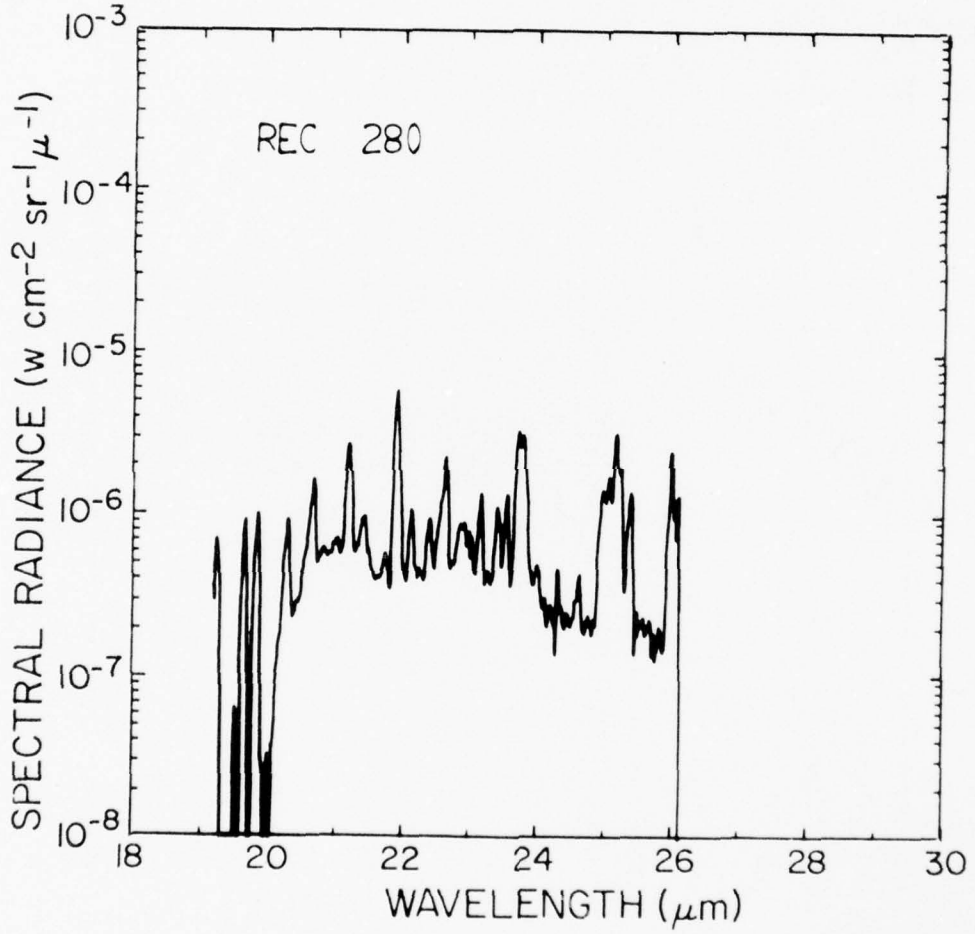

Figure 27. Sample spectrum of long wavelength region observed at an altitude of 38.0 km and a zenith angle of 93° on 27 June 1974.

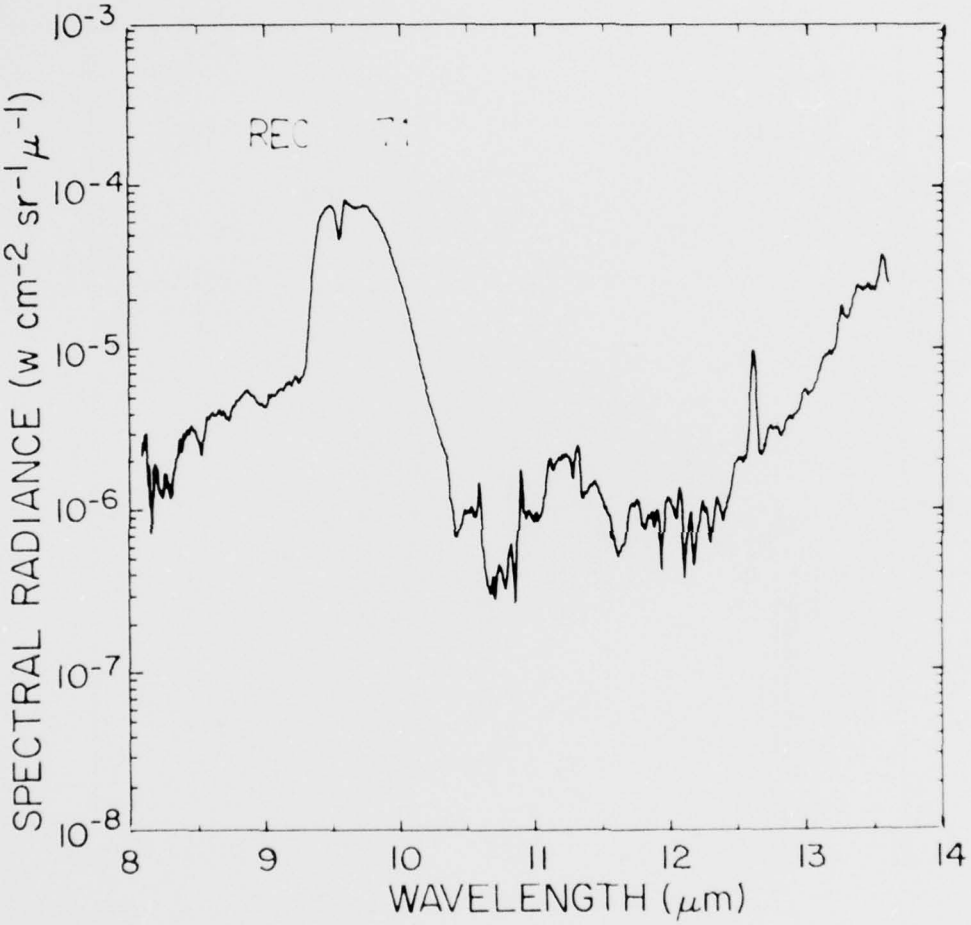

Figure 28. Sample spectrum of short wavelength region observed at an altitude of 9.5 km and a zenith angle of 63° on 19 February 1975.

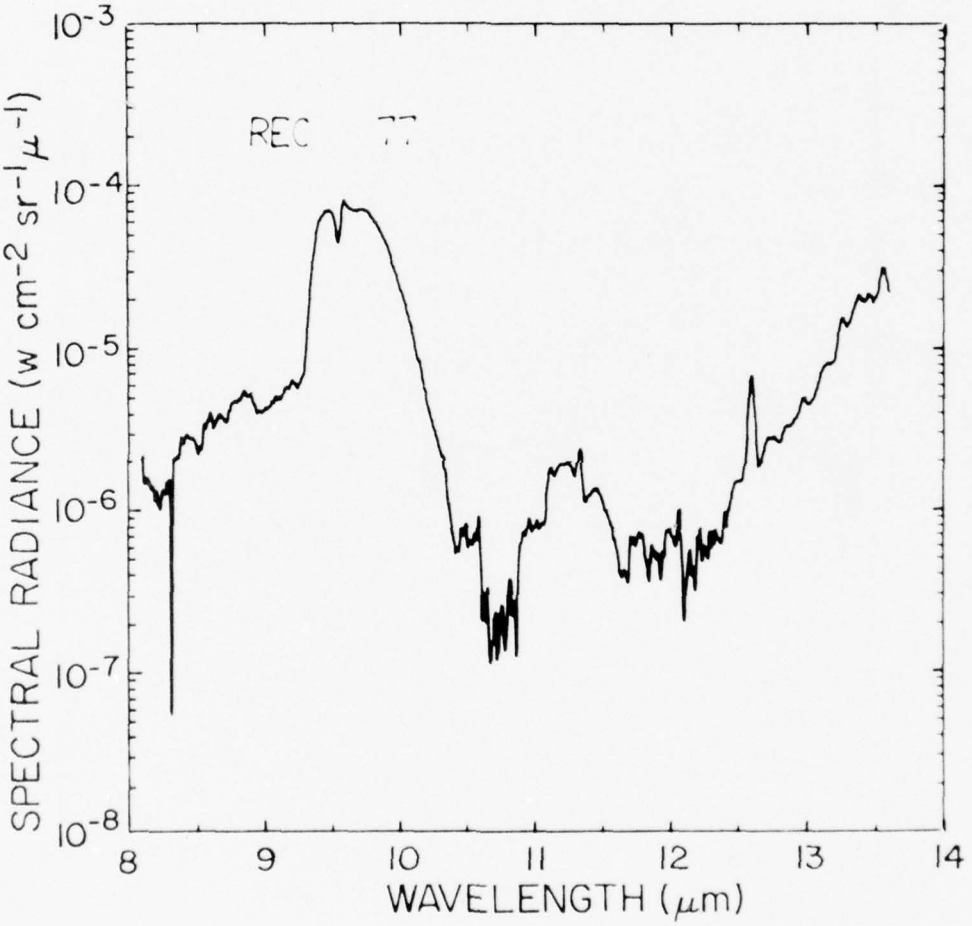

Figure 29. Sample spectrum of short wavelength region observed at an altitude of 11.0 km and a zenith angle of 63° on 19 February 1975.

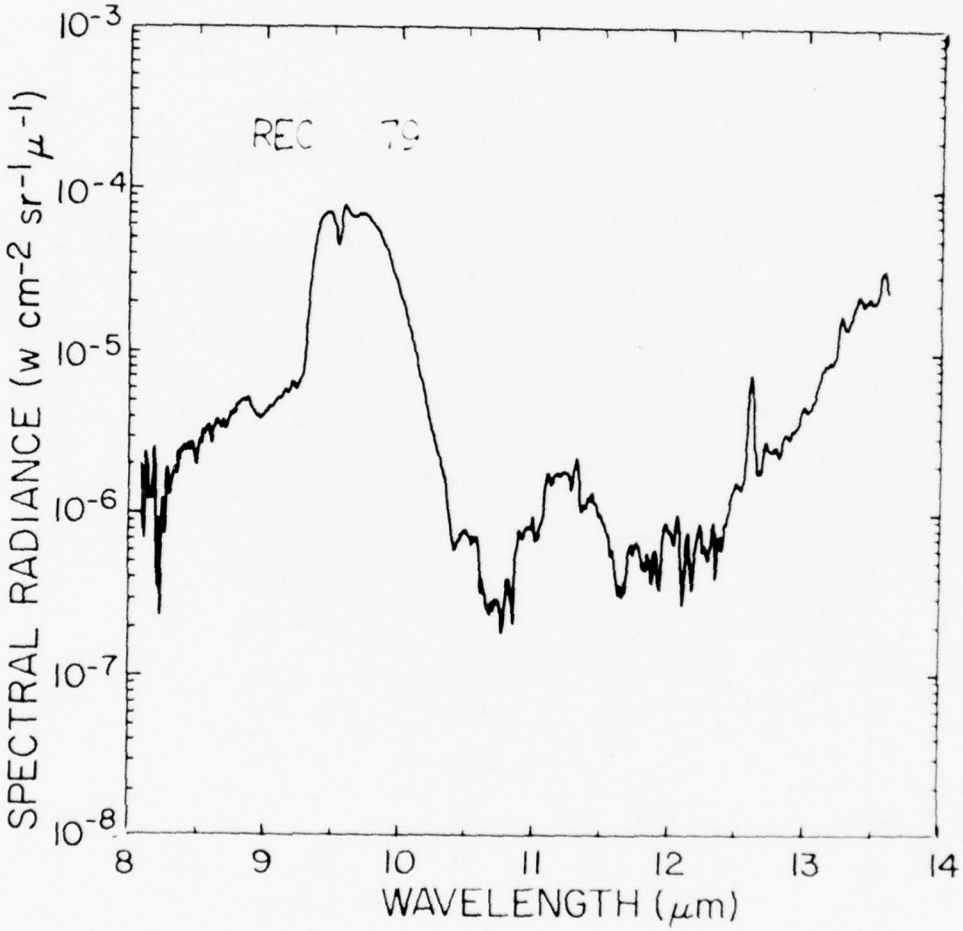

Figure 30. Sample spectrum of short wavelength region observed at an altitude of 11.5 km and a zenith angle of 63° on 19 February 1975.

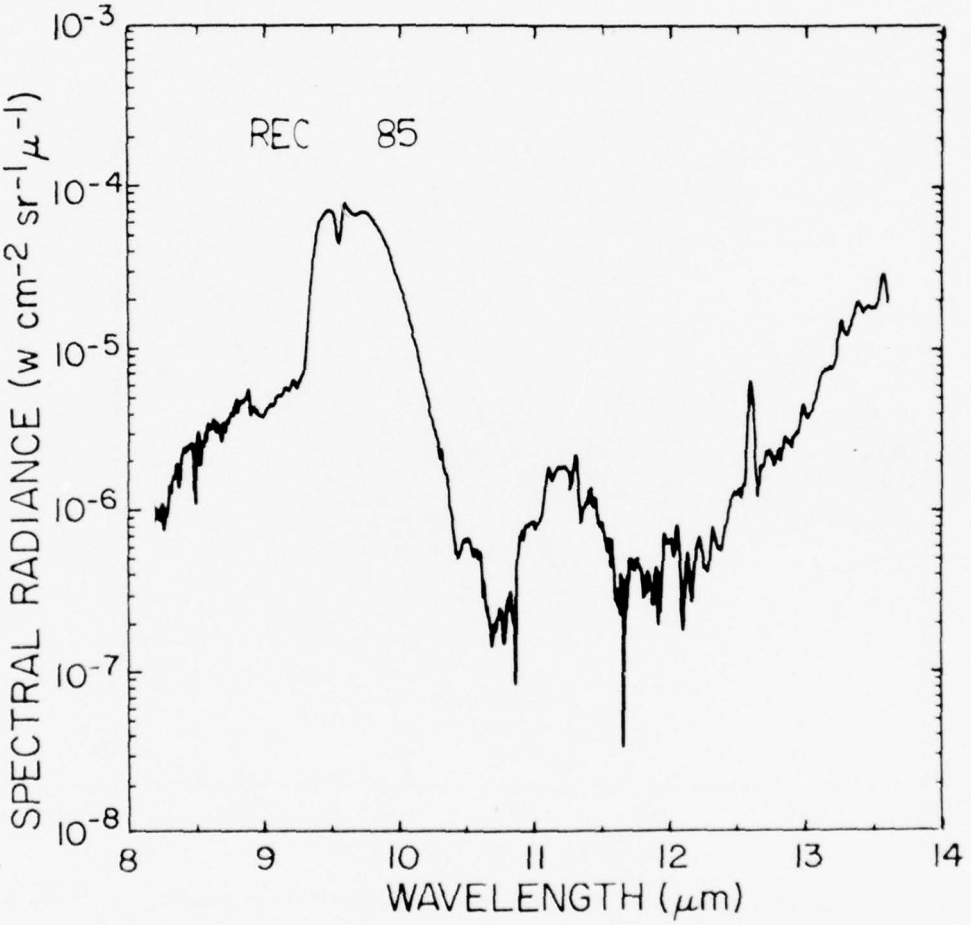

Figure 31. Sample spectrum of short wavelength region observed at an altitude of 12.2 km and a zenith angle of 63° on 19 February 1975.

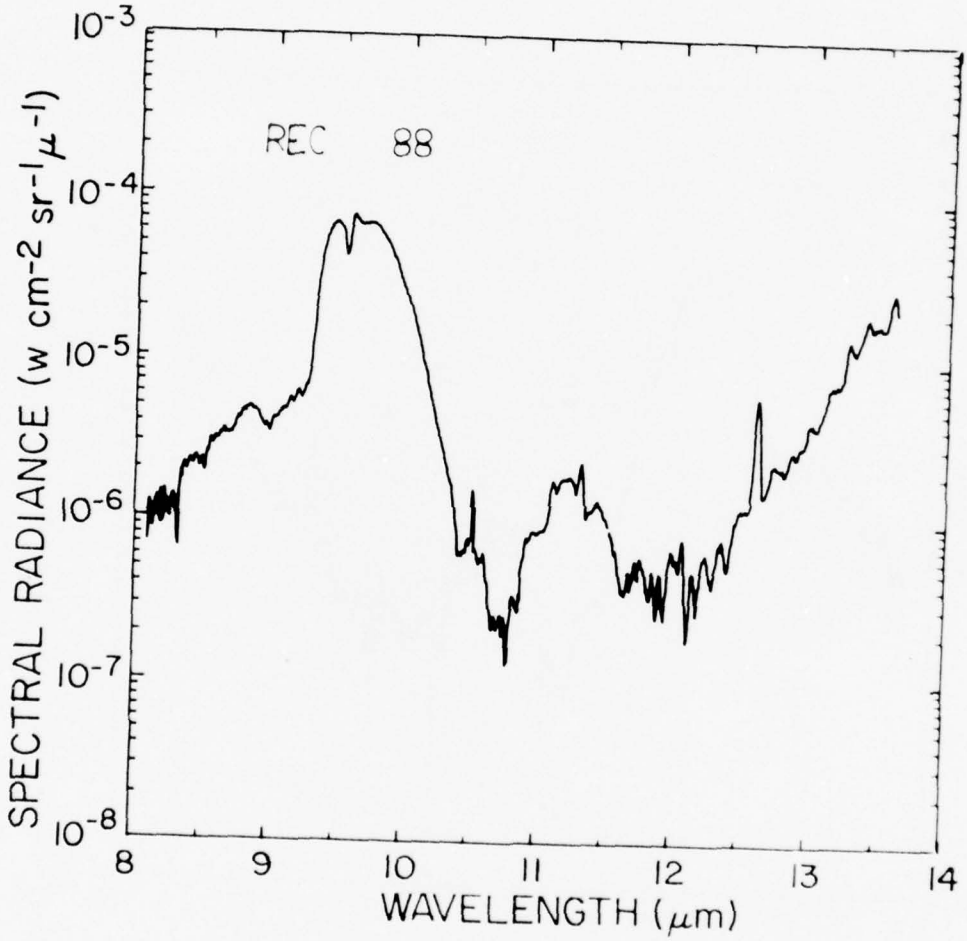

Figure 32. Sample spectrum of short wavelength region observed at an altitude of 12.5 km and a zenith angle of 63° on 19 February 1975.

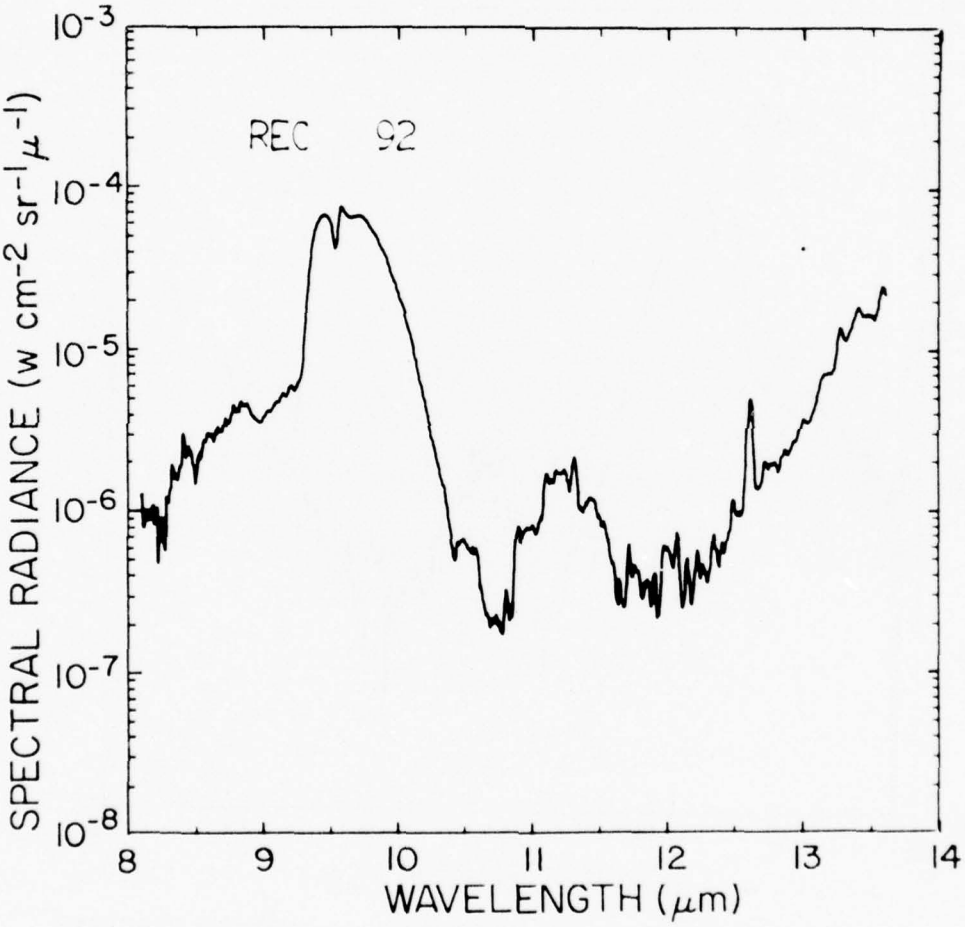

Figure 33. Sample spectrum of short wavelength region observed at an altitude of 12.9 km and a zenith angle of 63° on 19 February 1975.

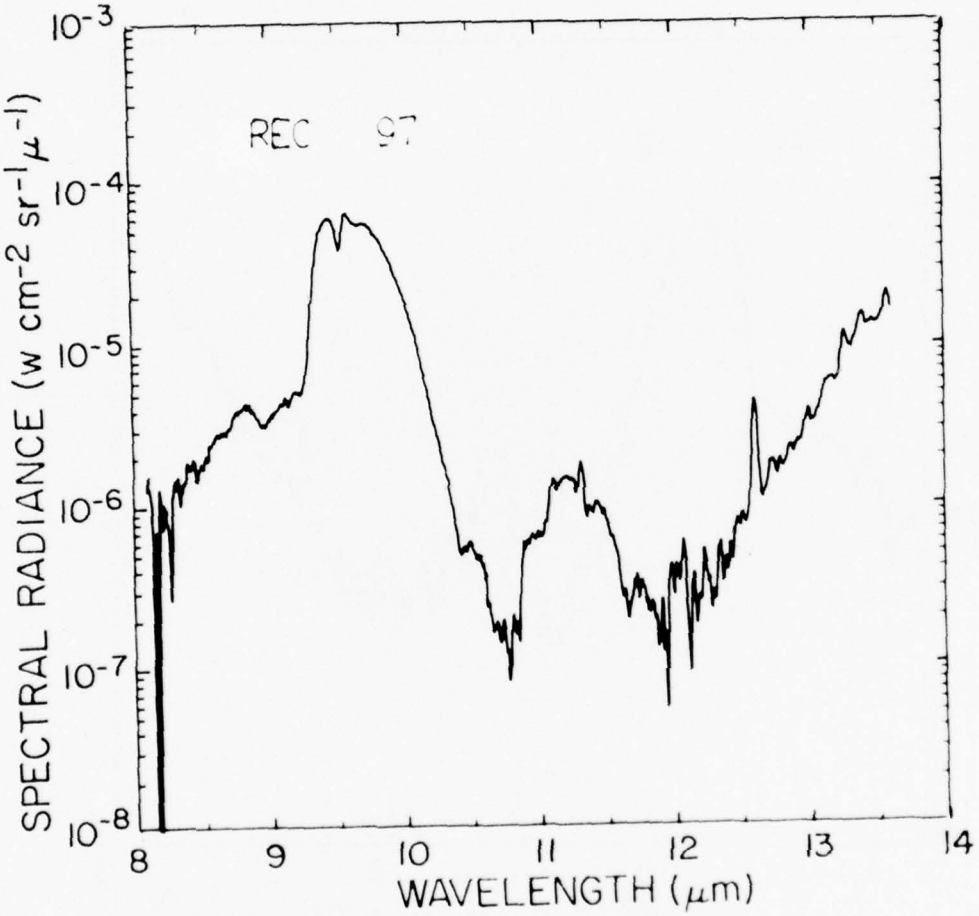

Figure 34. Sample spectrum of short wavelength region observed at an altitude of 13.5 km and a zenith angle of 63° on 19 February 1975.

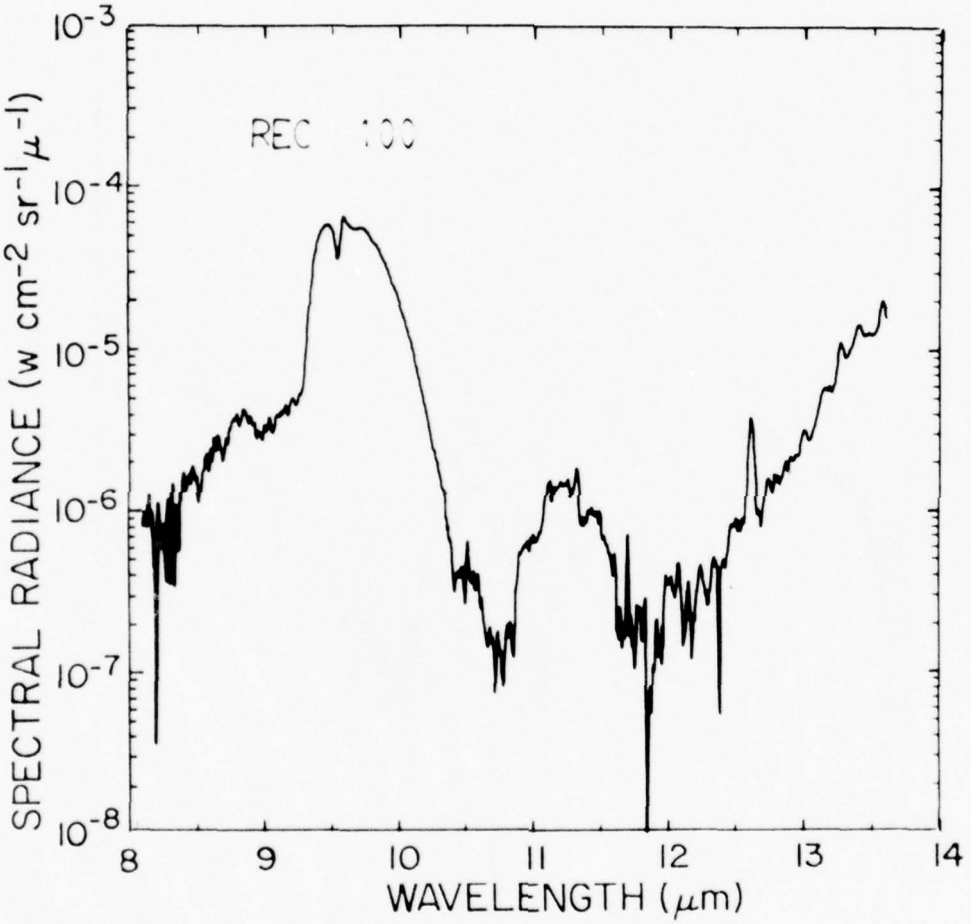

Figure 35. Sample spectrum of short wavelength region observed at an altitude of 14.5 km and a zenith angle of 63° on 19 February 1975.

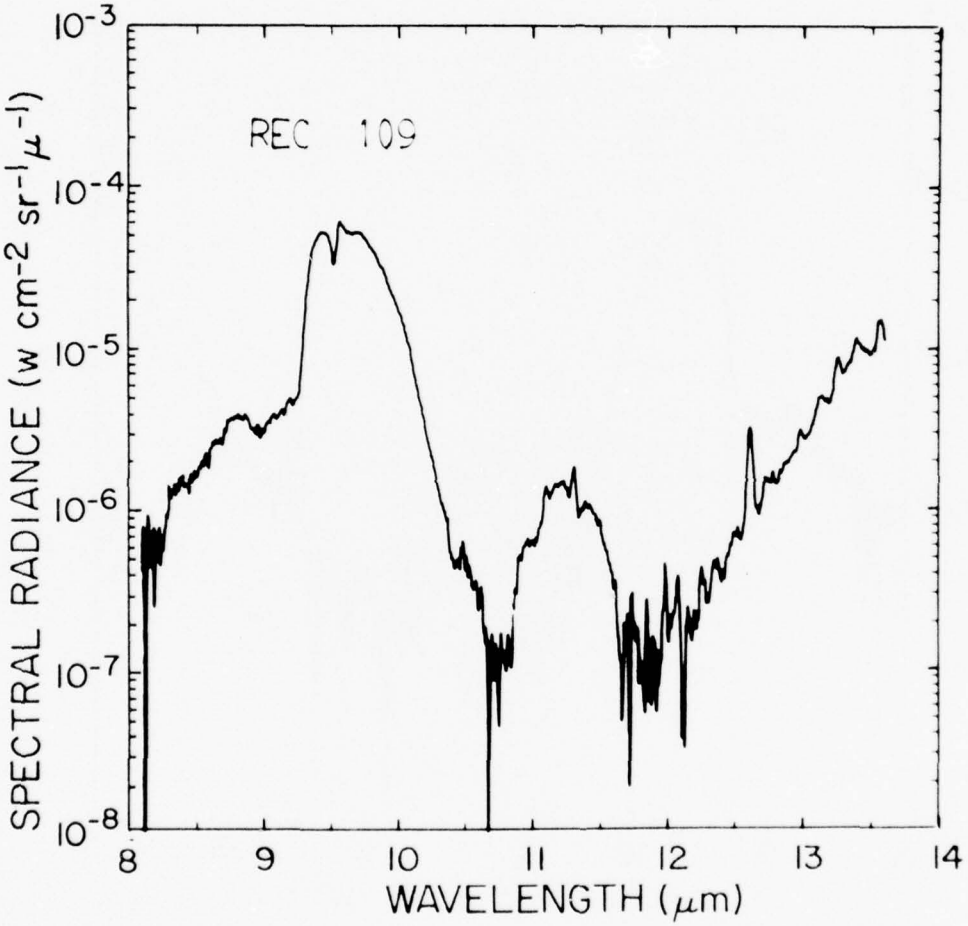

Figure 36. Sample spectrum of short wavelength region observed at an altitude of 16.5 km and a zenith angle of 63° on 19 February 1975.

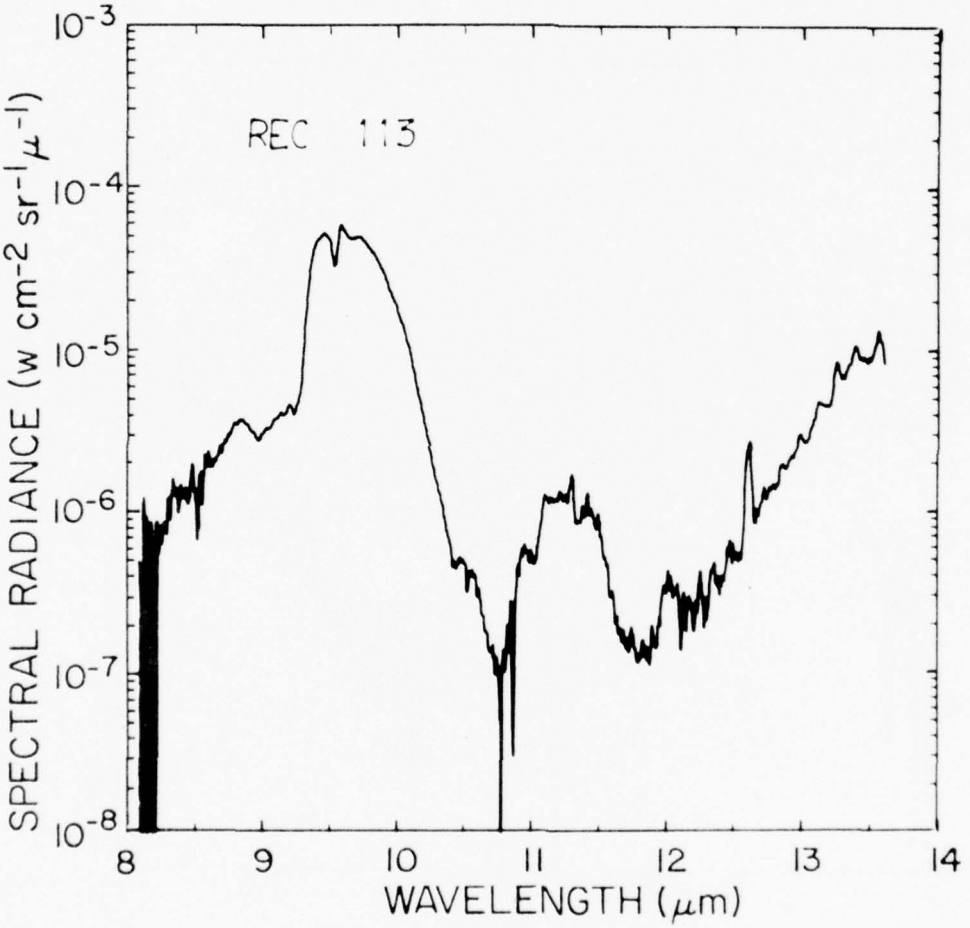

Figure 37. Sample spectrum of short wavelength region observed at an altitude of 17.0 km and a zenith angle of 63° on 19 February 1975.

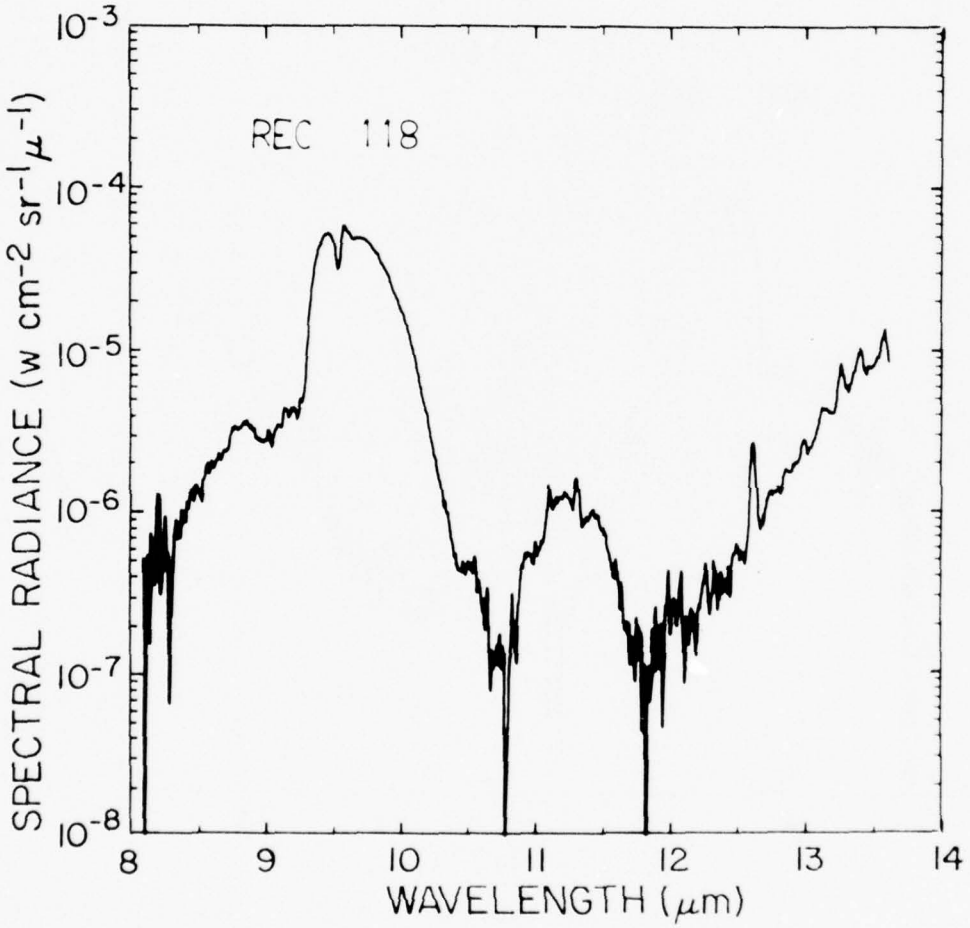

Figure 38. Sample spectrum of short wavelength region observed at an altitude of 18.0 km and a zenith angle of 63^{o} on 19 February 1975.

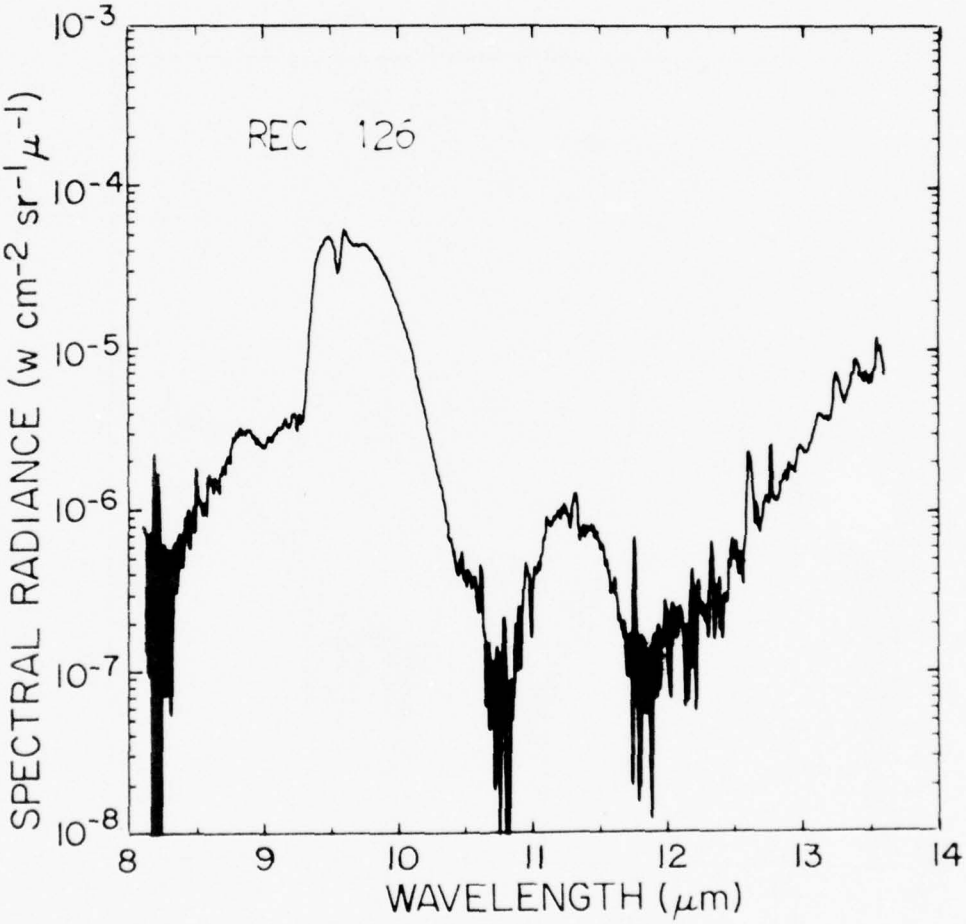

Figure 39. Sample spectrum of short wavelength region observed at an altitude of 19.6 km and a zenith angle of 63° on 19 February 1975.

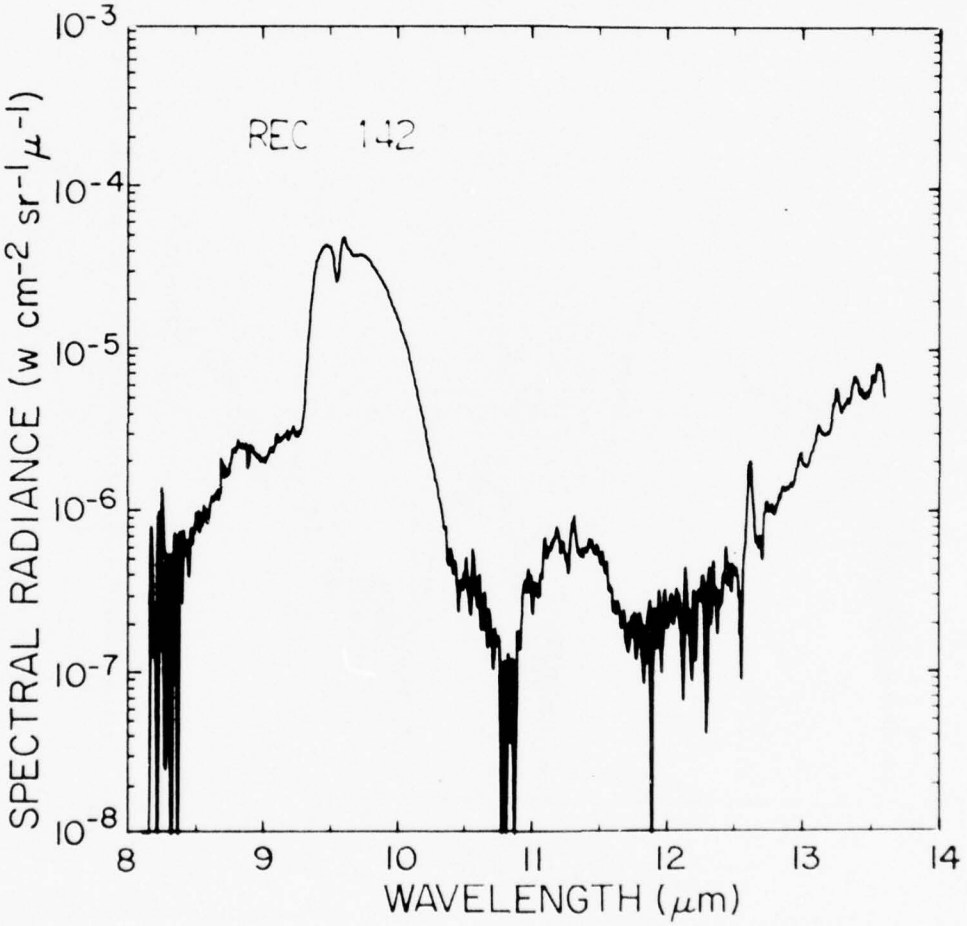

Figure 40. Sample spectrum of short wavelength region observed at an altitude of 21.9 km and a zenith angle of 63° on 19 February 1975.

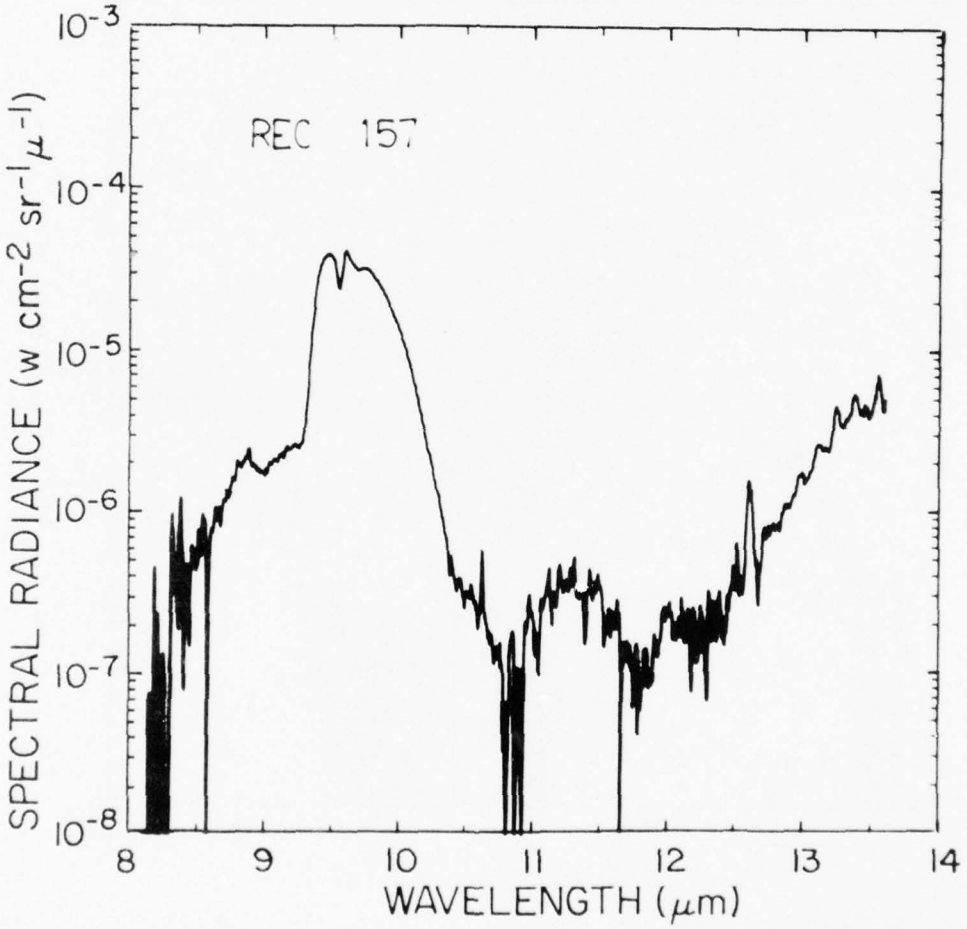

Figure 41. Sample spectrum of short wavelength region observed at an altitude of 24.0 km and a zenith angle of 63° on 19 February 1975.

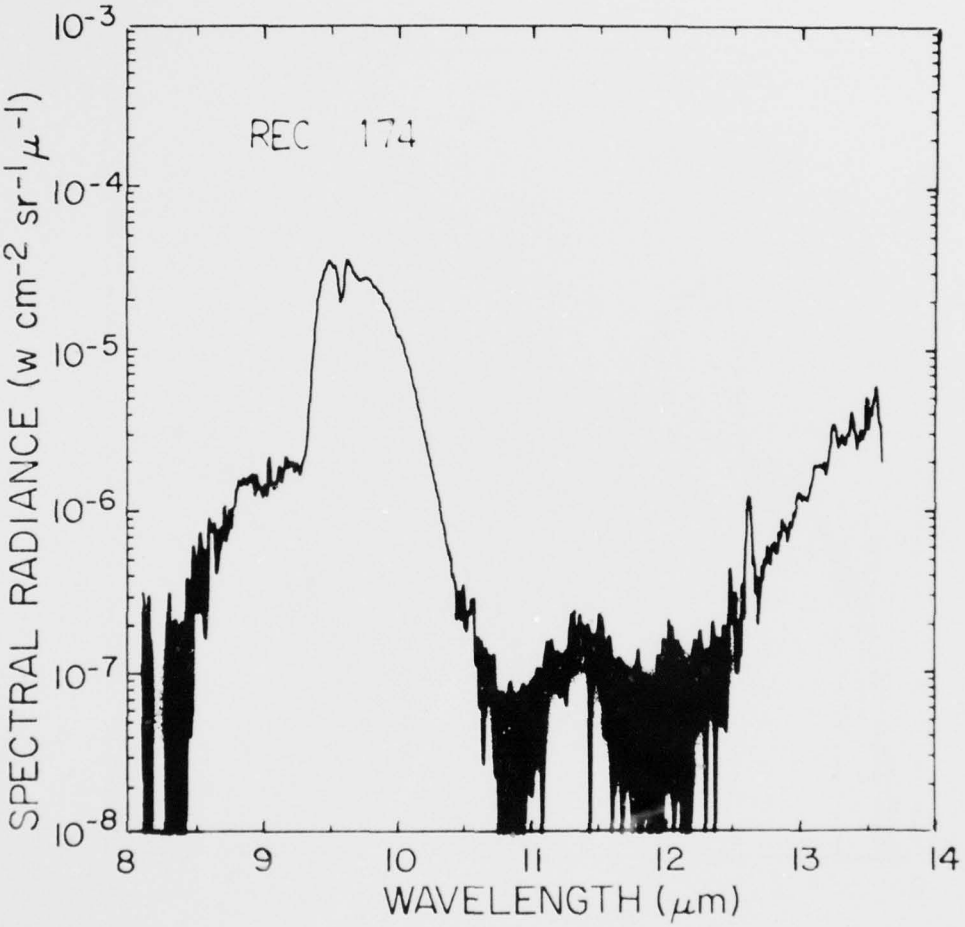

Figure 42. Sample spectrum of short wavelength region observed at an altitude of 26.5 km and a zenith angle of 63° on 19 February 1975.

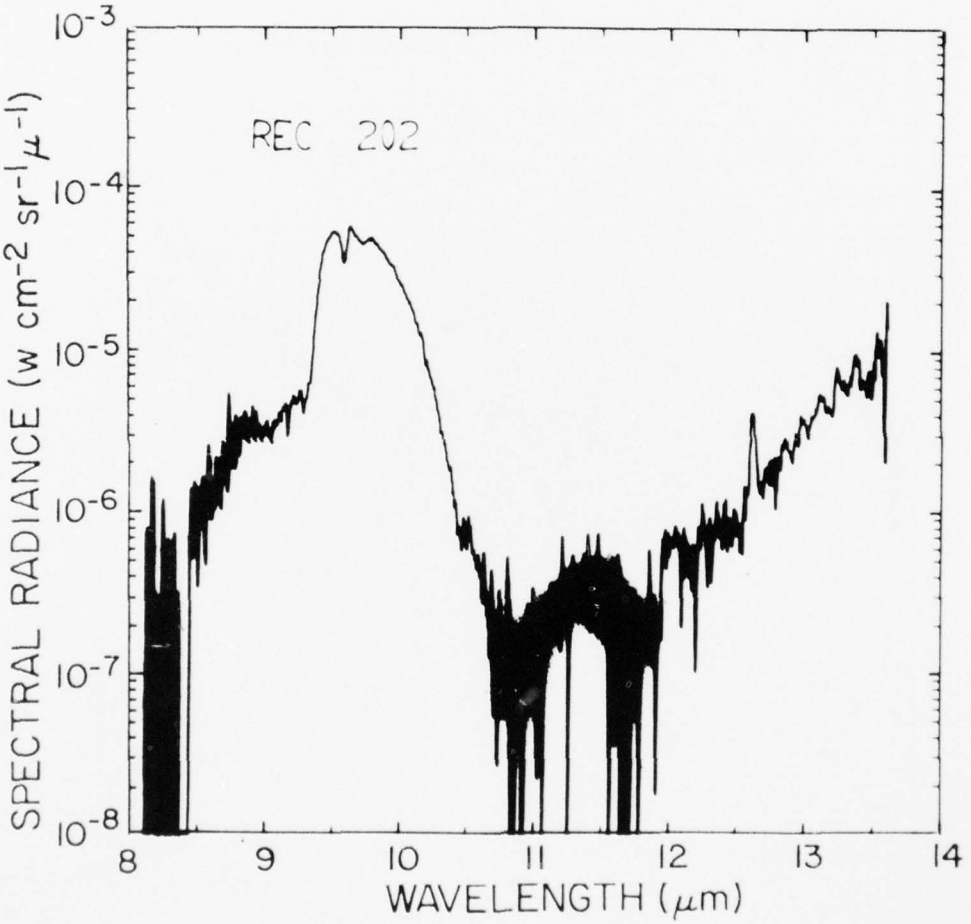

Figure 43. Sample spectrum of short wavelength region observed at an altitude of 29.1 km and a zenith angle of 83° on 19 February 1975.

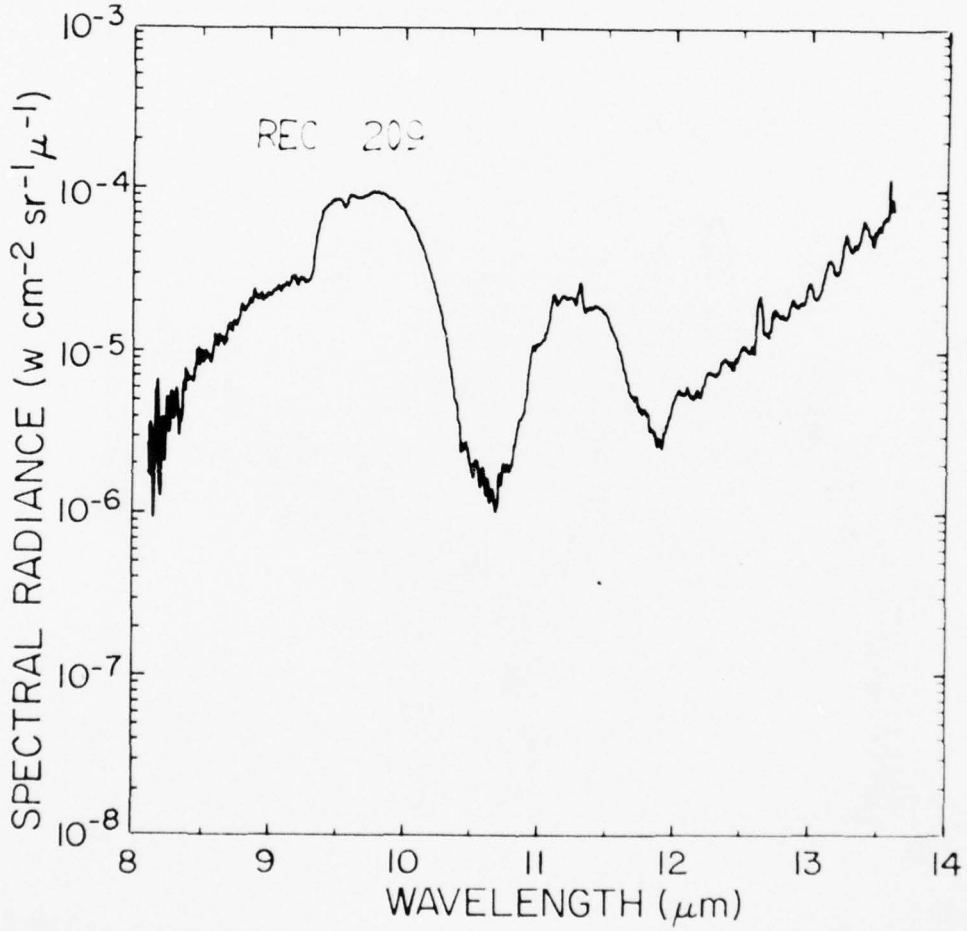

Figure 44. Sample spectrum of short wavelength region observed at an altitude of 29.1 km and a zenith angle of 93° on 19 February 1975.

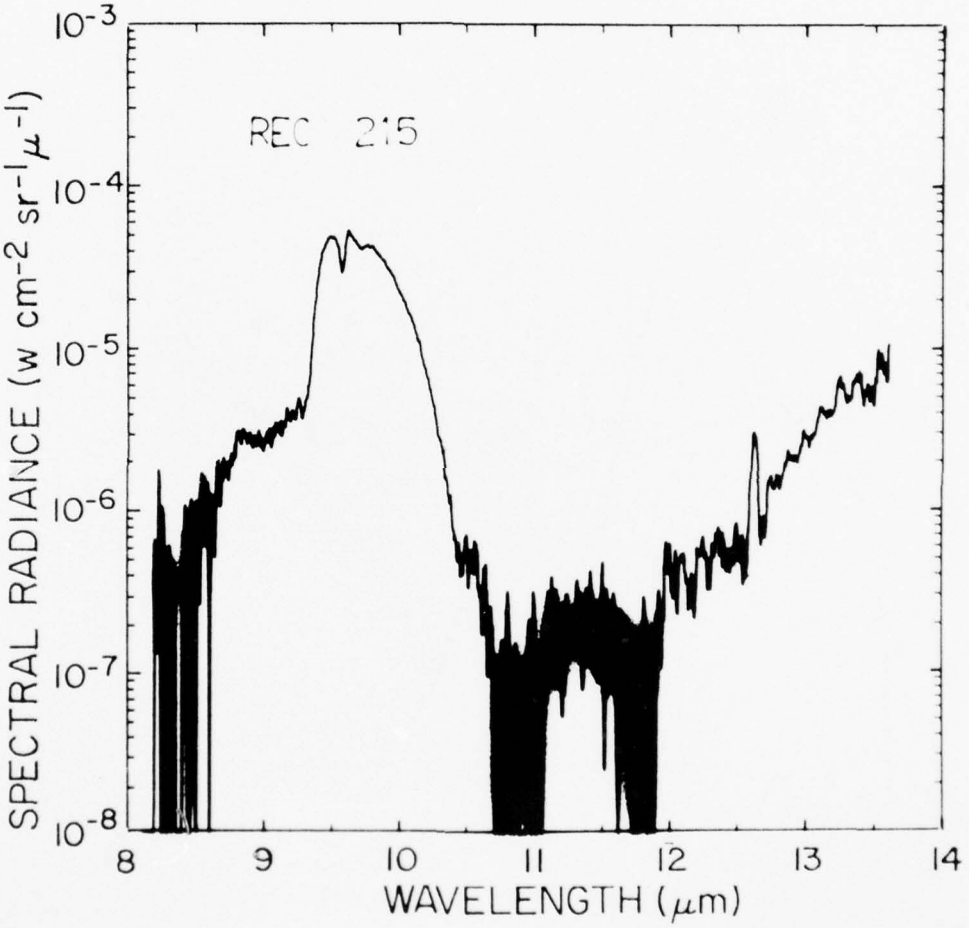

Figure 45. Sample spectrum of short wavelength region observed at an altitude of 29.1 km and a zenith angle of 81° on 19 February 1975.

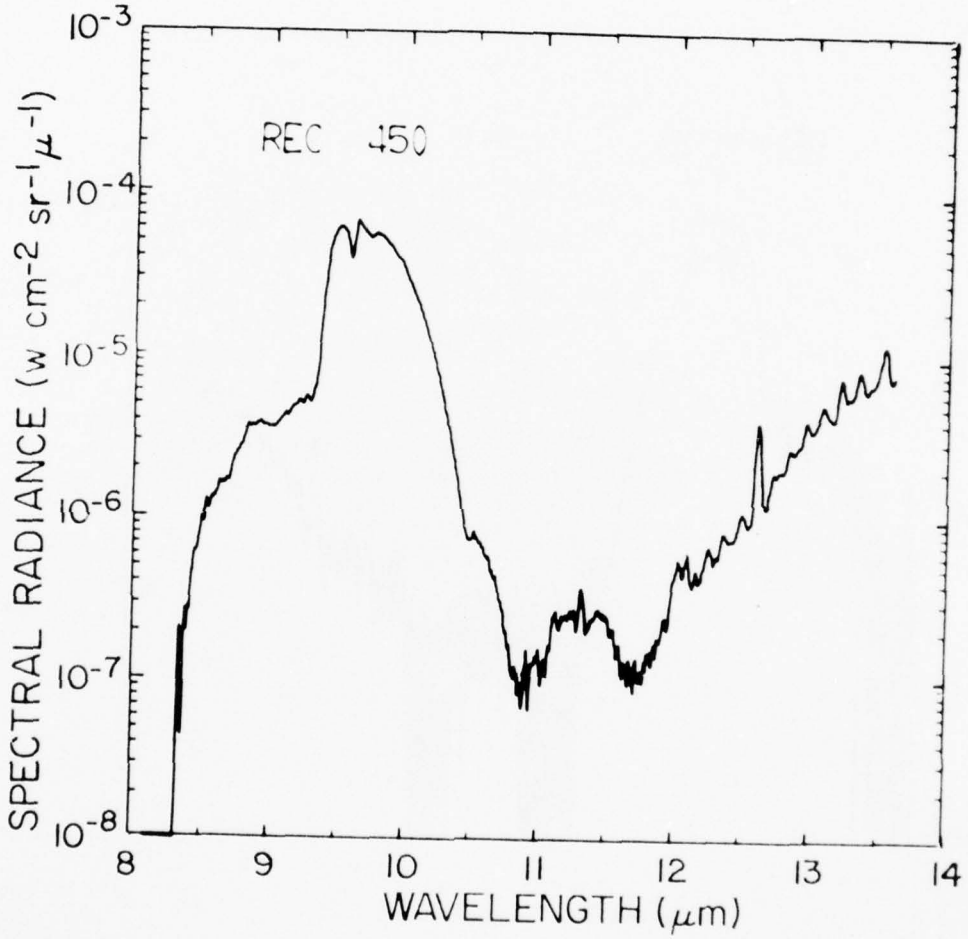

Figure 46. Sample spectrum of short wavelength region observed at an altitude of 29.1 km and a zenith angle of 81° on 19 February 1975.

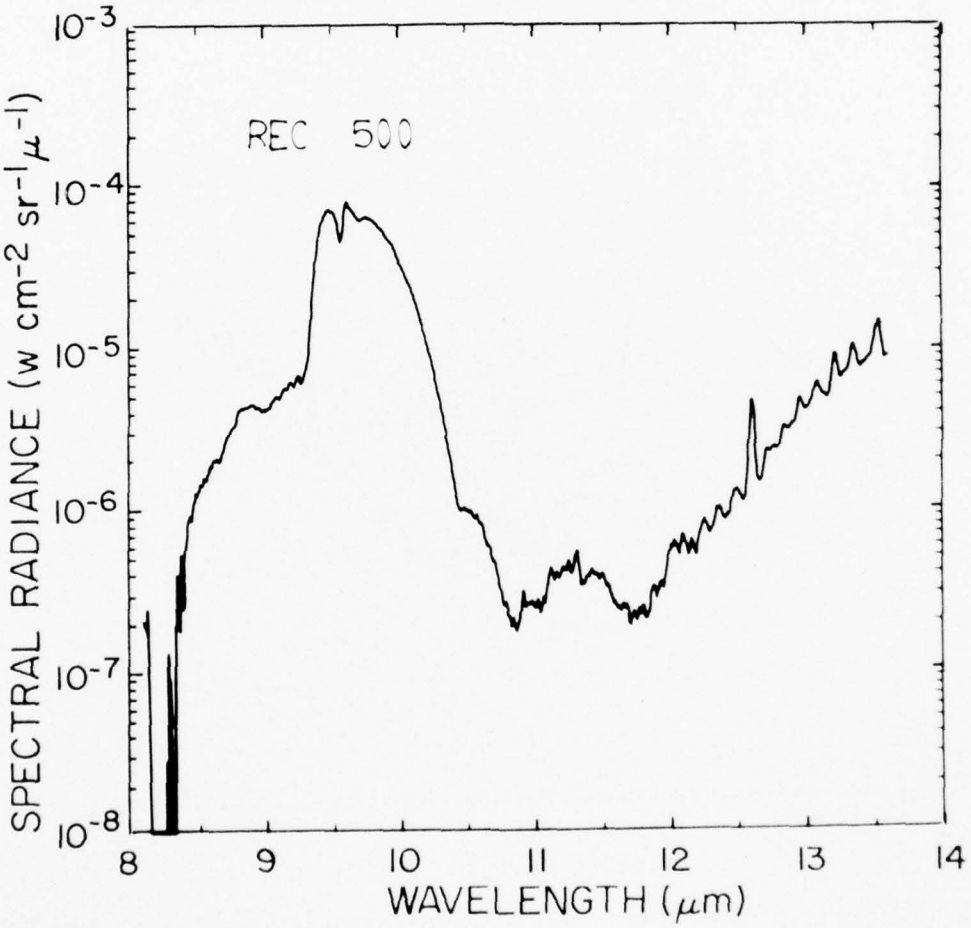

Figure 47. Sample spectrum of short wavelength region observed at an altitude of 29.1 km and a zenith angle of 81° on 19 February 1975.

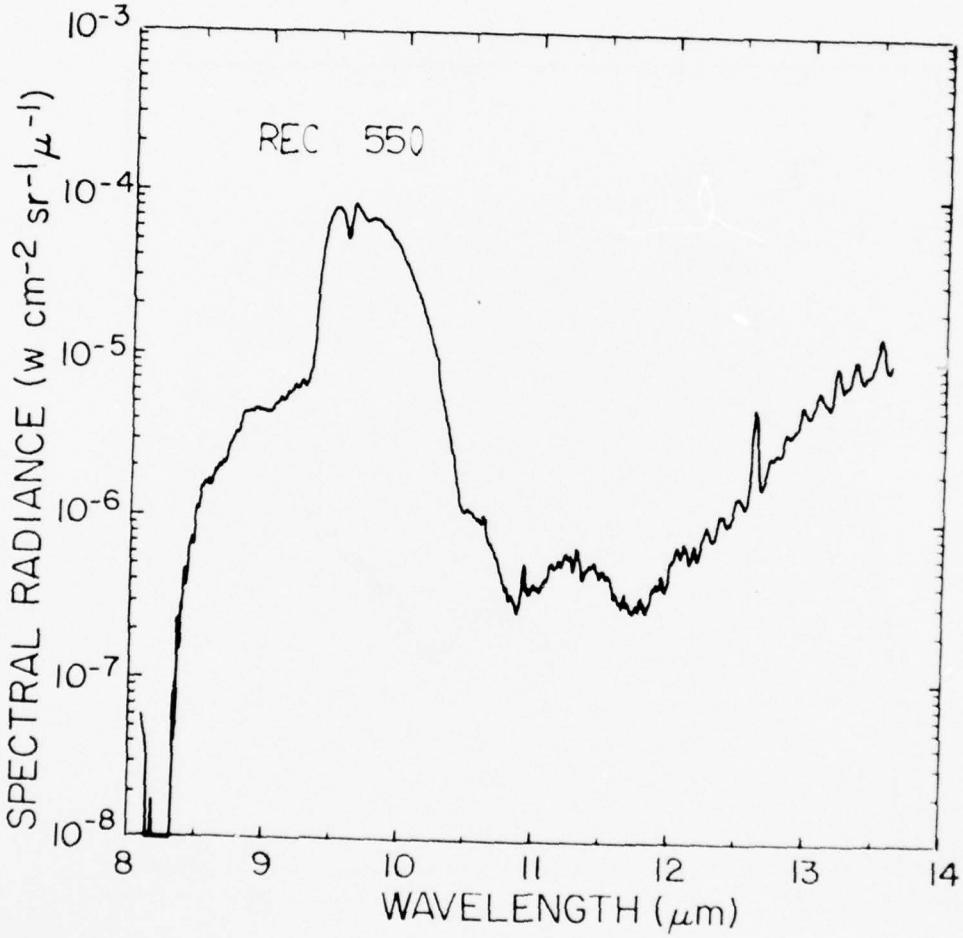

Figure 48. Sample spectrum of short wavelength region observed at an altitude of 29.1 km and a zenith angle of 81° on 19 February 1975.

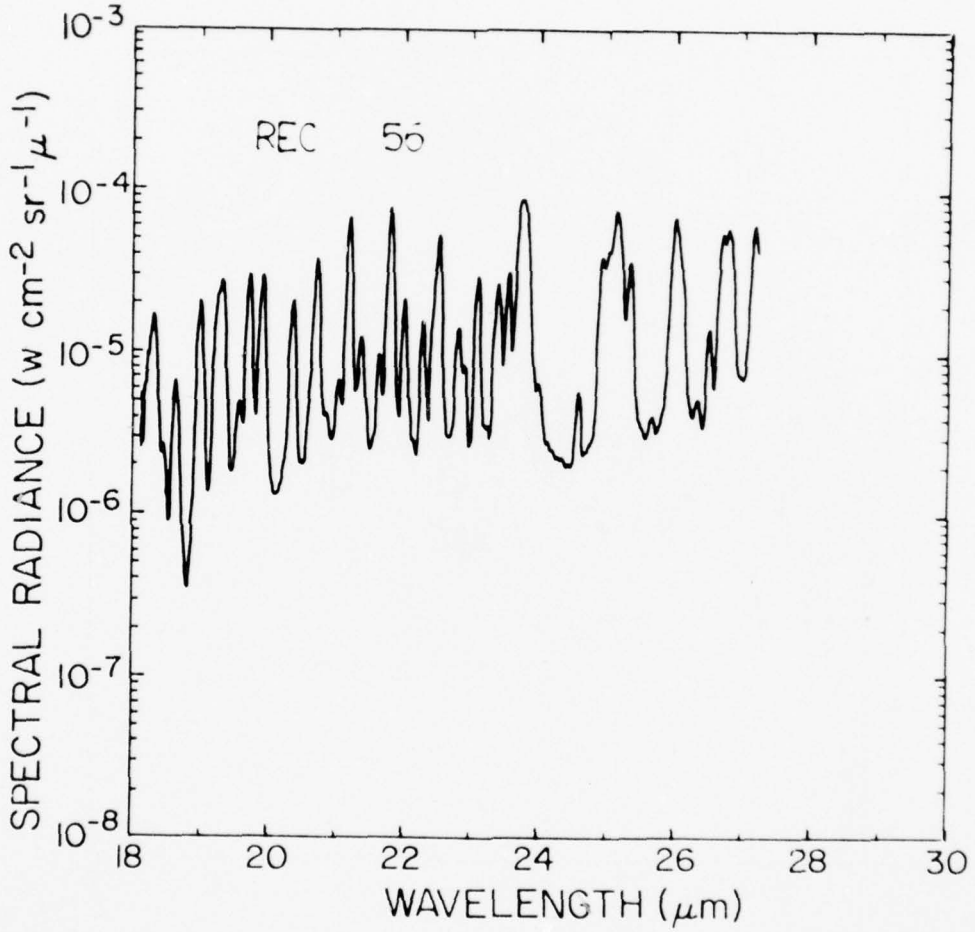

Figure 49. Sample spectrum of long wavelength region observed at an altitude of 7.0 km and a zenith angle of 63° on 19 February 1975.

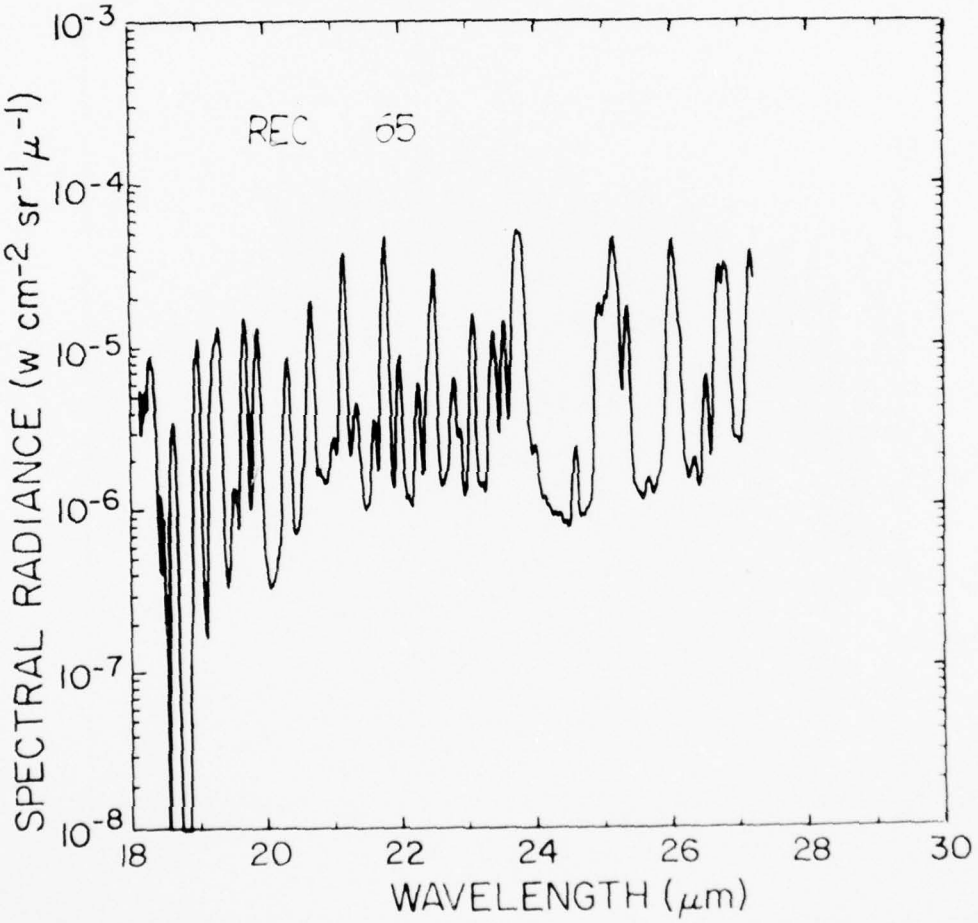

Figure 50. Sample spectrum of long wavelength region observed at an altitude of 8.5 km and a zenith angle of 63° on 19 February 1975.

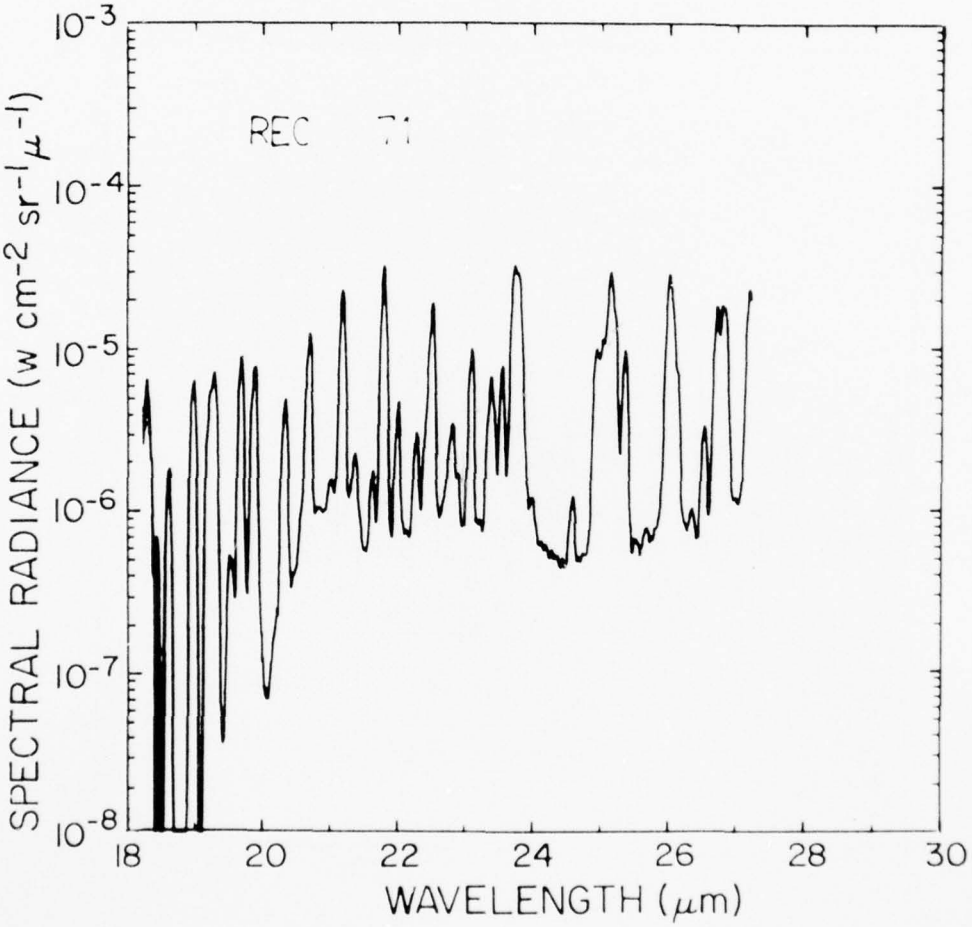

Figure 51. Sample spectrum of long wavelength region observed at an altitude of 9.5 km and a zenith angle of 63° on 19 February 1975.

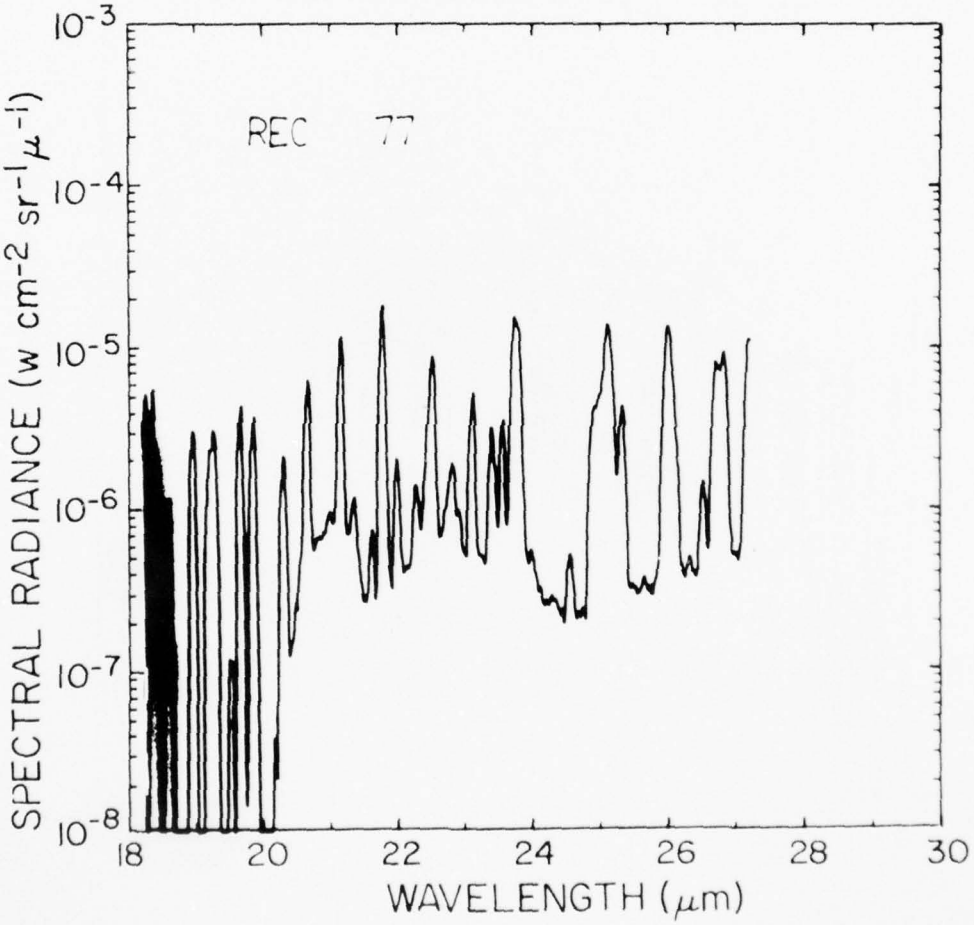

Figure 52. Sample spectrum of long wavelength region observed at an altitude of 11.0 km and a zenith angle of 63° on 19 February 1975.

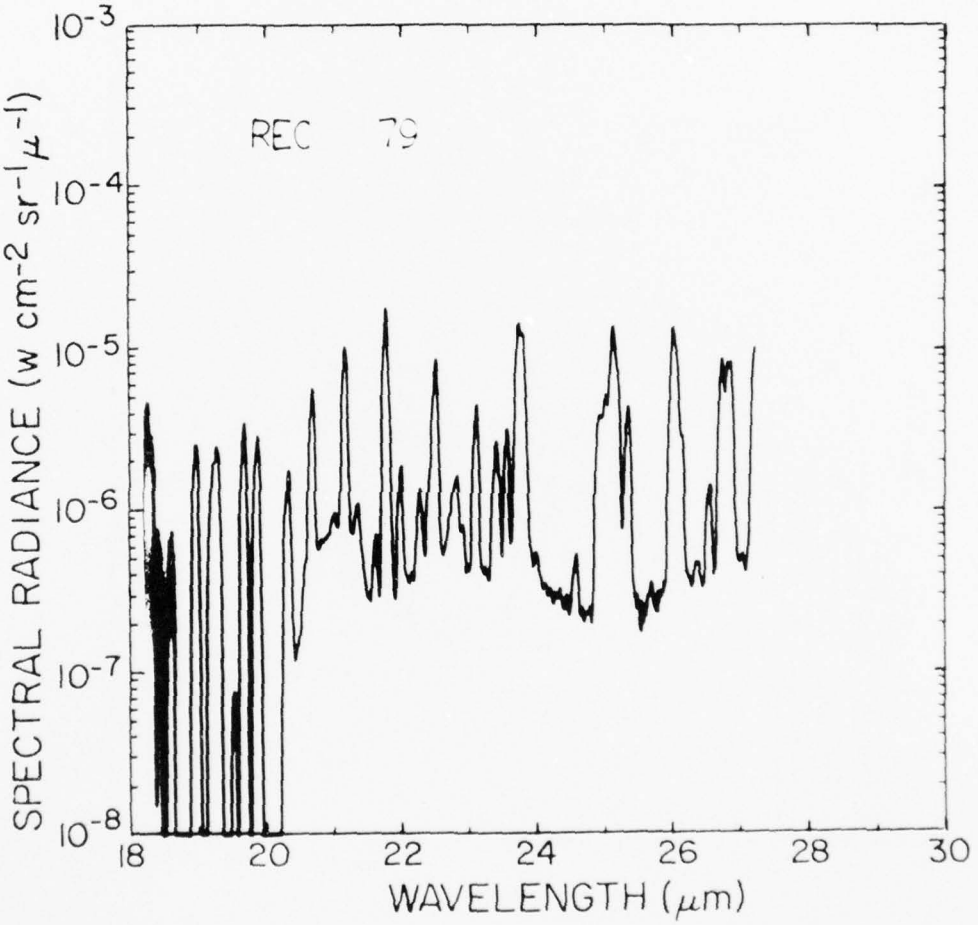

Figure 53. Sample spectrum of long wavelength region observed at an altitude of 11.5 km and a zenith angle of 63° on 19 February 1975.

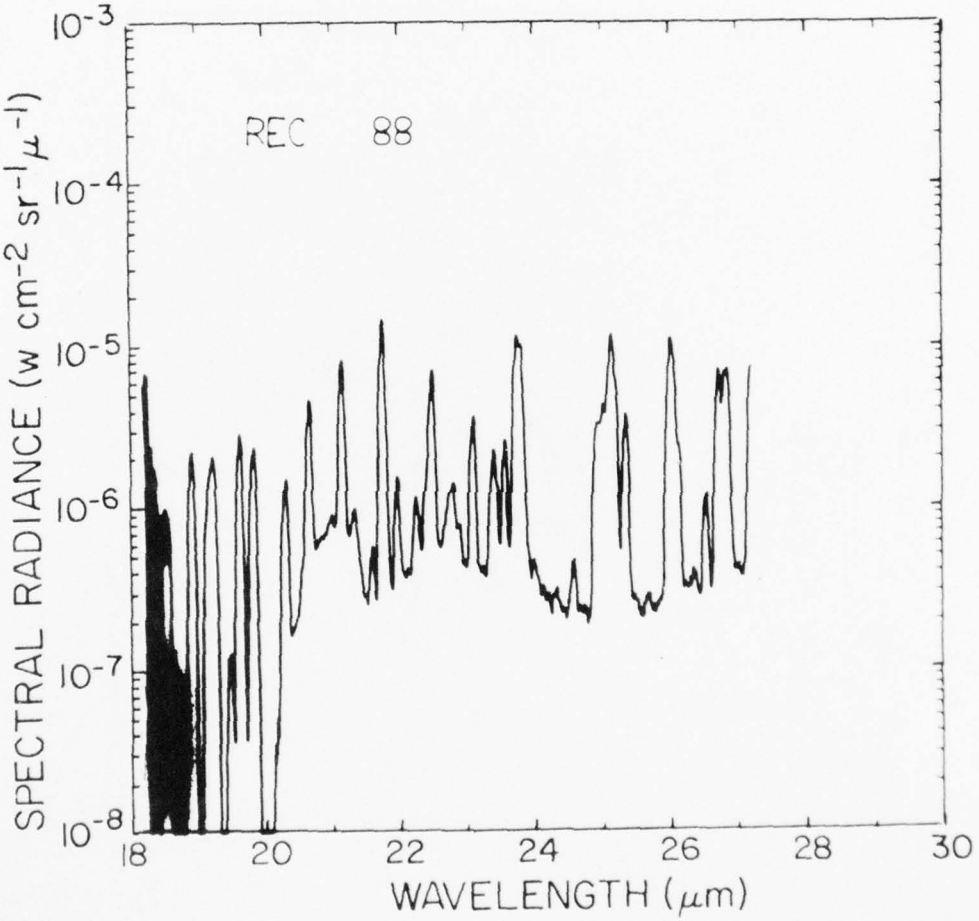

Figure 54. Sample spectrum of long wavelength region observed at an altitude of 12.5 km and a zenith angle of 63° on 19 February 1975.

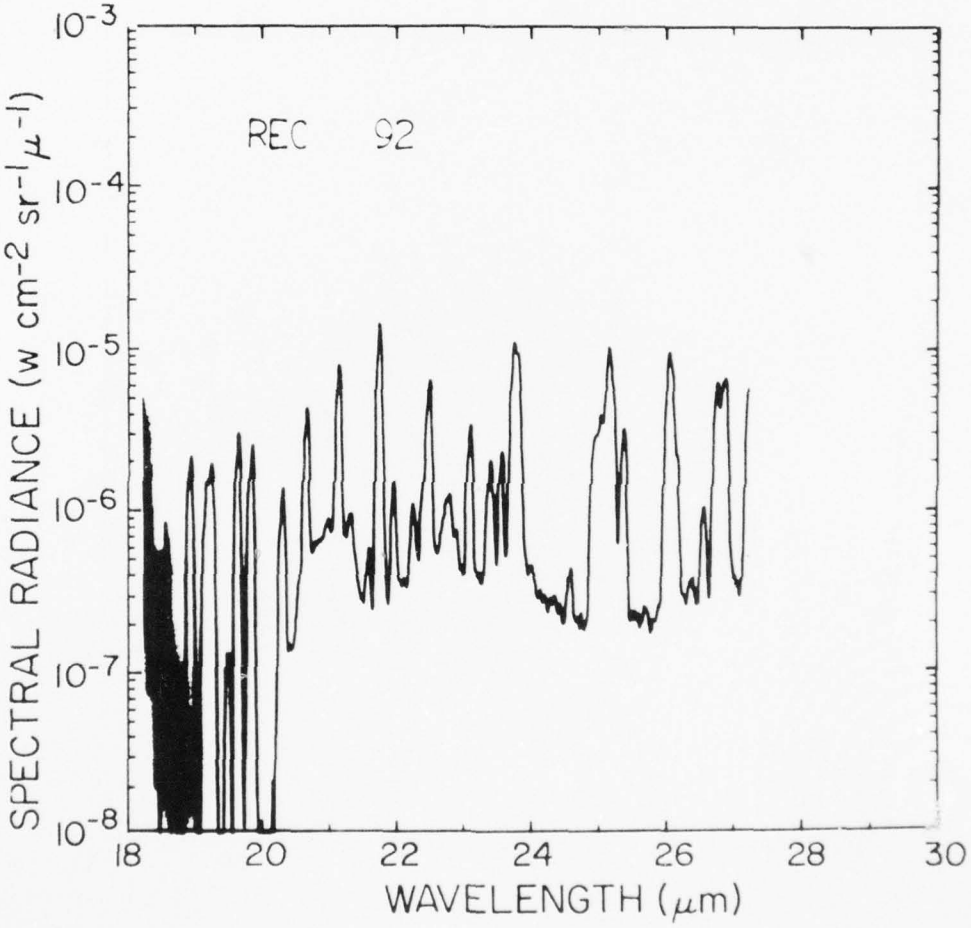

Figure 55. Sample spectrum of long wavelength region observed at an altitude of 12.9 km and a zenith angle of 63° on 19 February 1975.

AD-A037 375 DENVER UNIV COLO DEPT OF PHYSICS AND ASTRONOMY F/G 4/1
WATER VAPOR, NITRIC ACID AND OZONE MIXING RATIO HEIGHT PROFILES--ETC(U)
FEB 77 D G MURCRAY, J N BROOKS, A GOLDMAN DAAD05-74-C-0795
UNCLASSIFIED BRL-CR-332 NL

2 OF 2
ADA037375

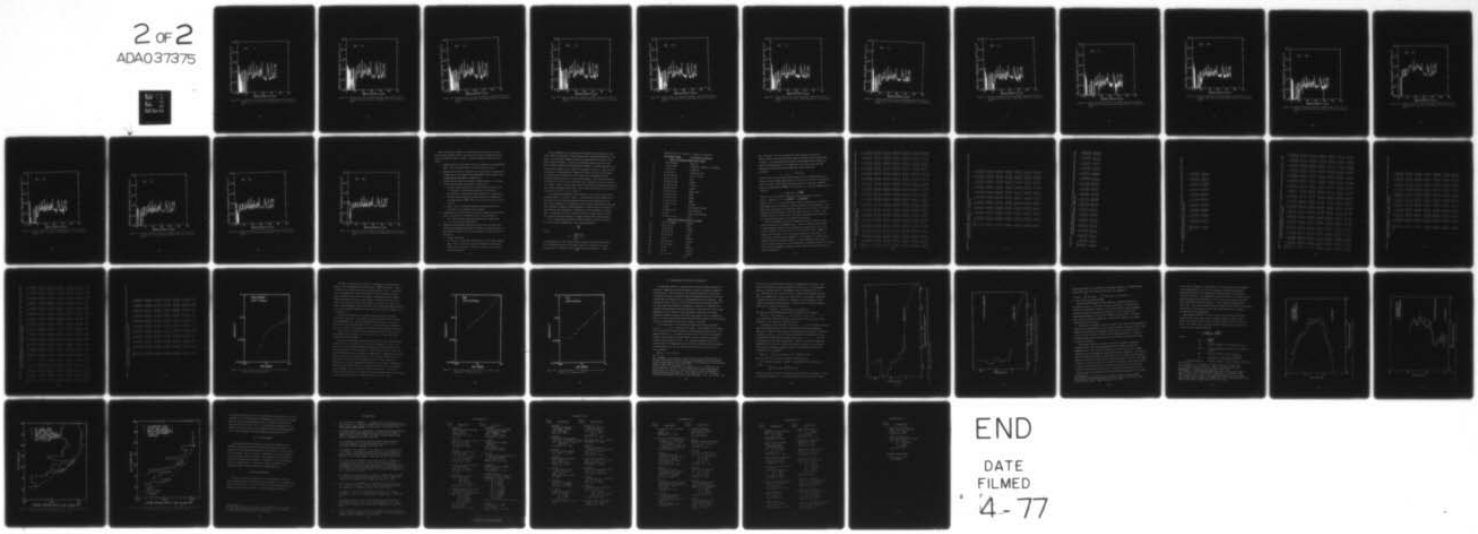

END

DATE
FILMED
4-77

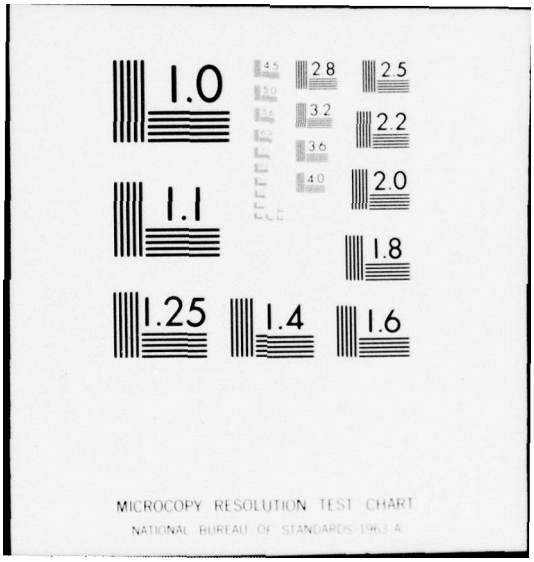
1.0
1.1
1.25
1.4
1.6
1.8
2.0
2.2
2.5
2.8
3.2
3.6
4.0
4.5
5.0
5.6
MICROCOPY RESOLUTION TEST CHART
NATIONAL BUREAU OF STANDARDS-1963-A

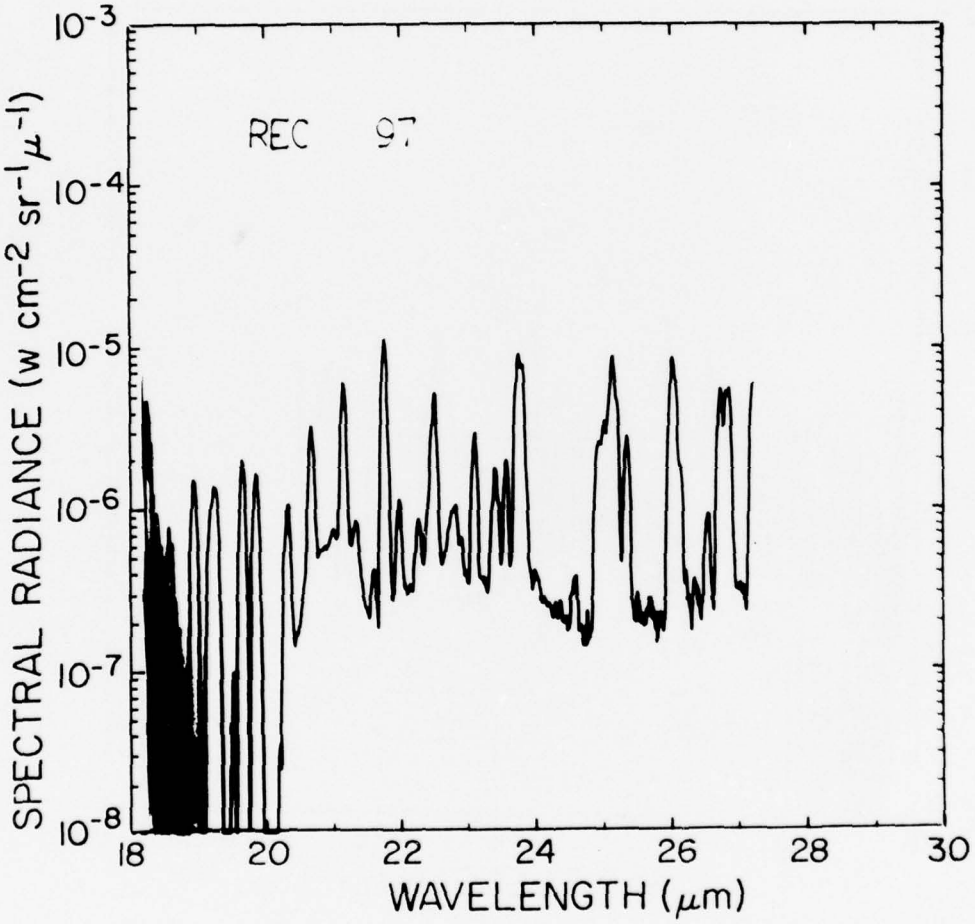

Figure 56. Sample spectrum of long wavelength region observed at an altitude of 13.5 km and a zenith angle of 63° on 19 February 1975.

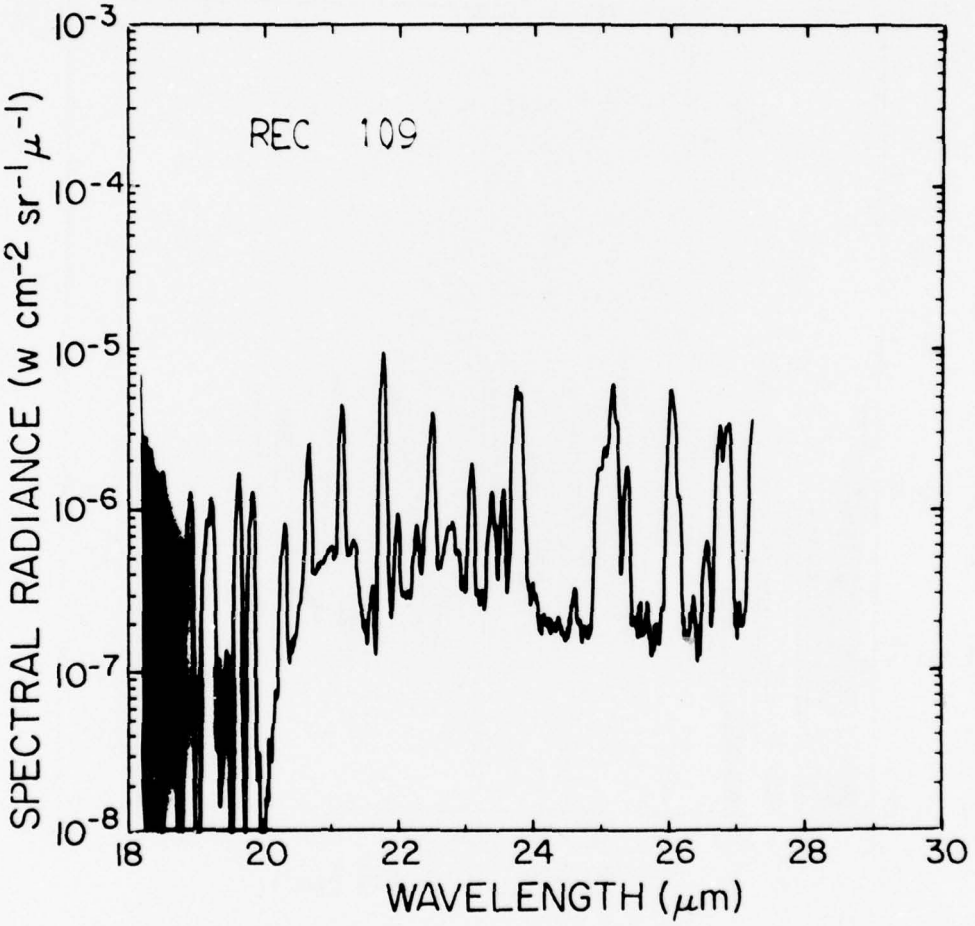

Figure 57. Sample spectrum of long wavelength region observed at an altitude of 16.5 km and a zenith angle of 63° on 19 February 1975.

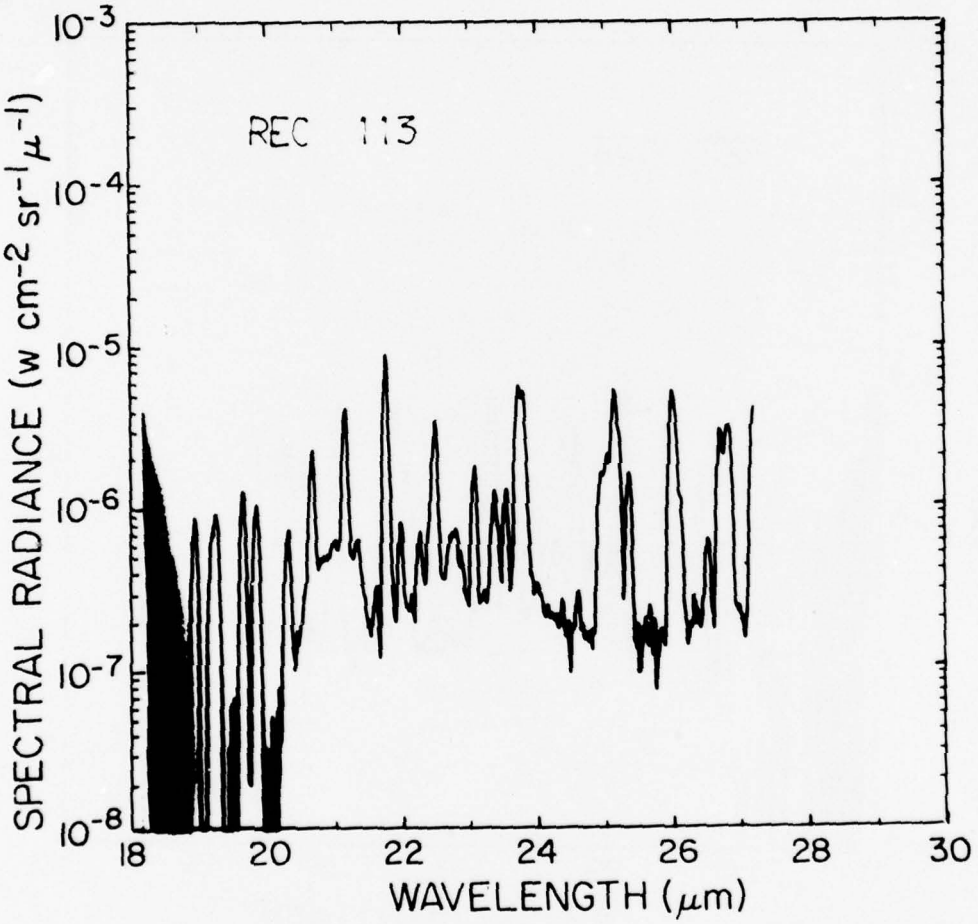

Figure 58. Sample spectrum of long wavelength region observed at an altitude of 17.0 km and a zenith angle of 63° on 19 February 1975.

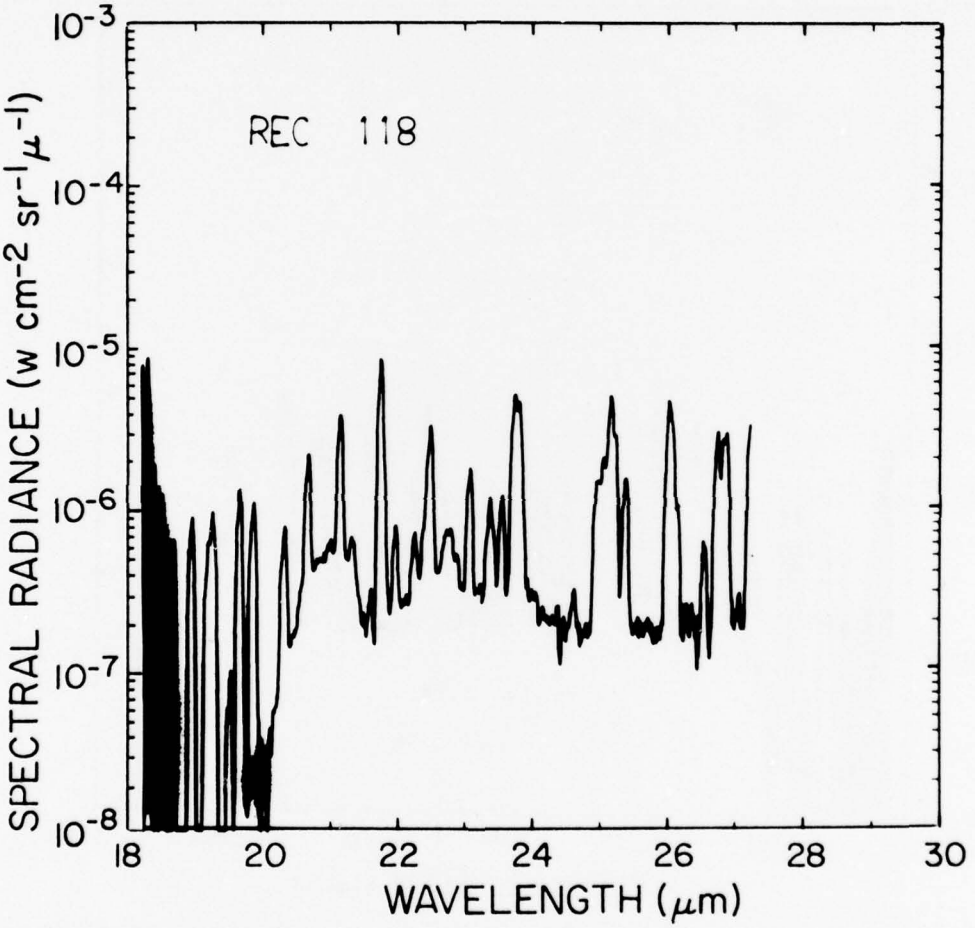

Figure 59. Sample spectrum of long wavelength region observed at an altitude of 18.0 km and a zenith angle of 63° on 19 February 1975.

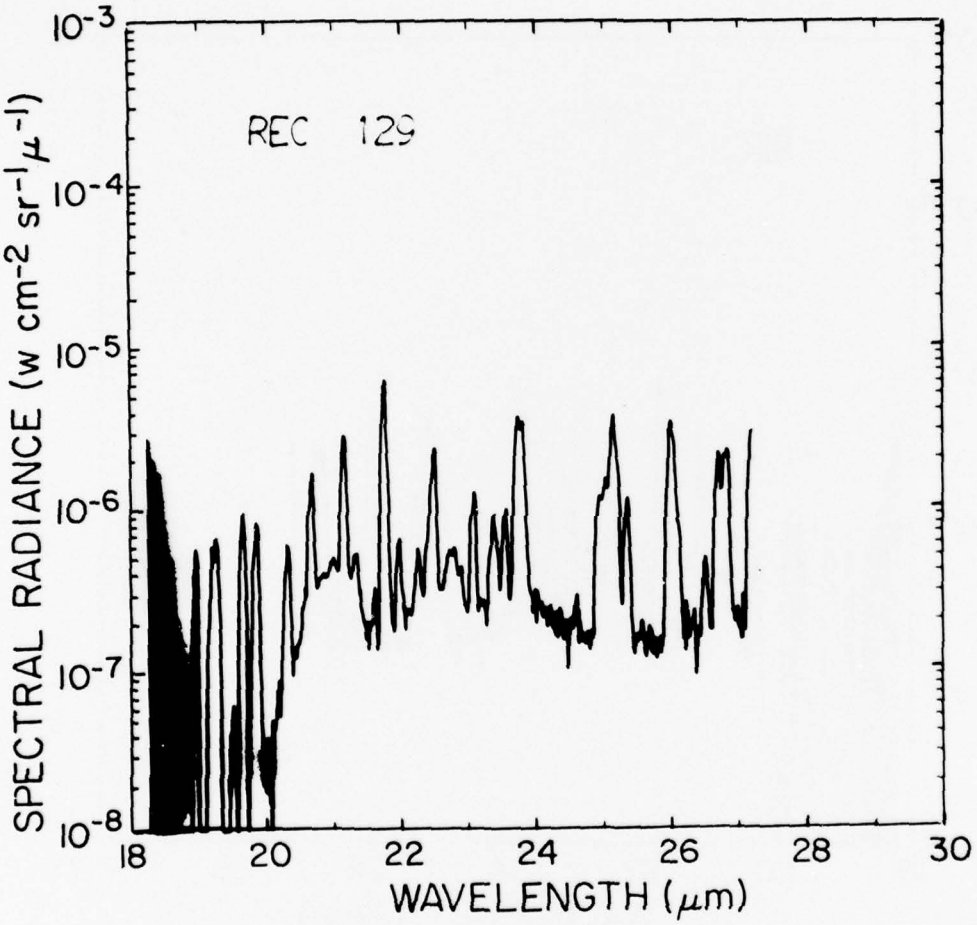

Figure 60. Sample spectrum of long wavelength region observed at an altitude of 20.0 km and a zenith angle of 63° on 19 February 1975.

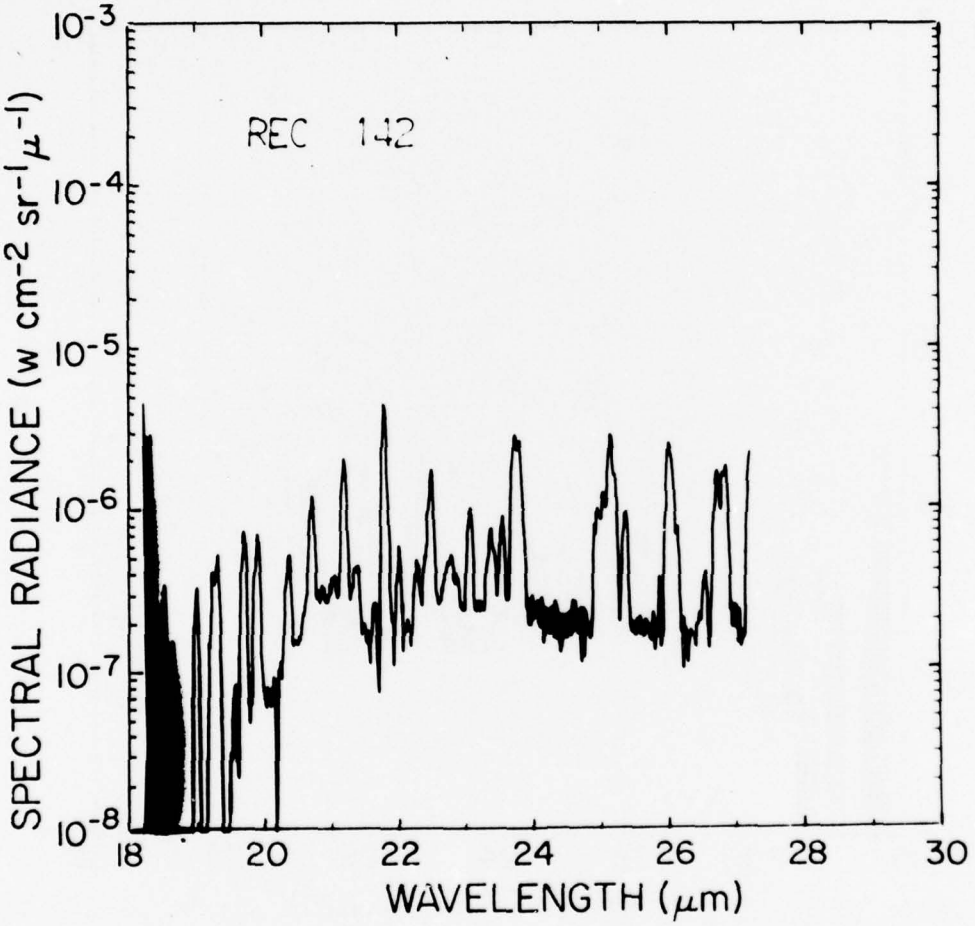

Figure 61. Sample spectrum of long wavelength region observed at an altitude of 21.9 km and a zenith angle of 63° on 19 February 1975.

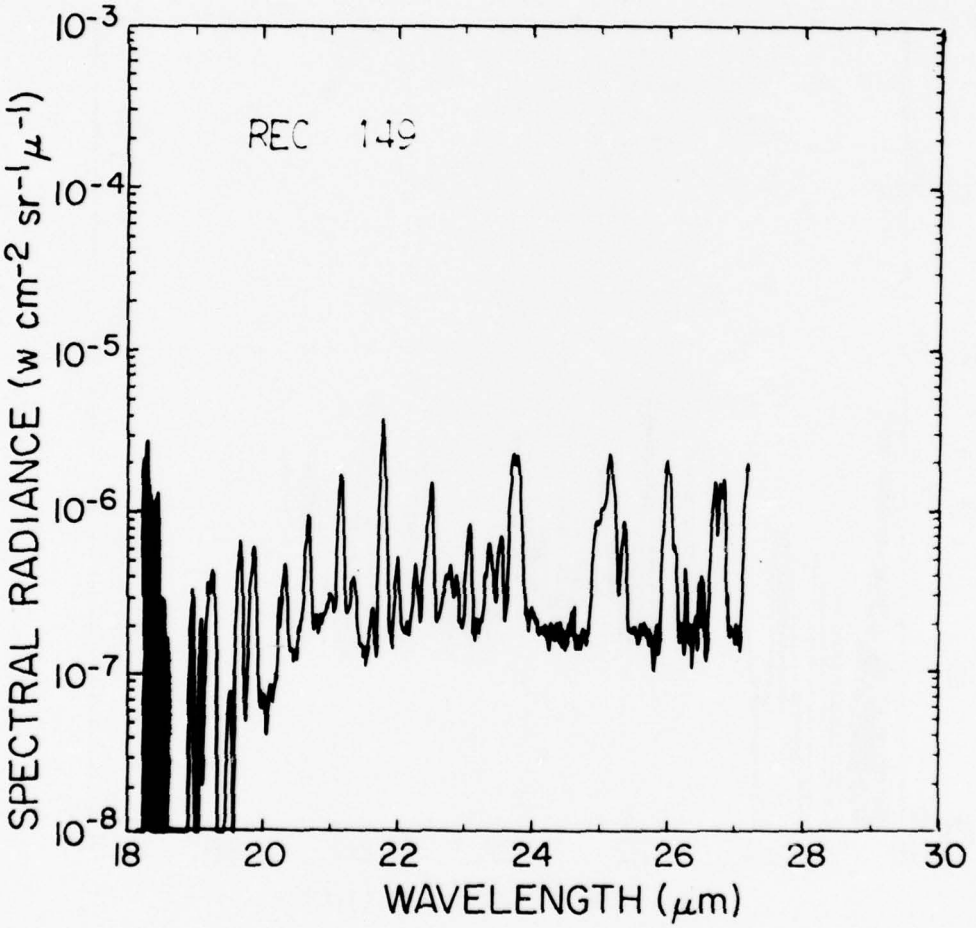

Figure 62. Sample spectrum of long wavelength region observed at an altitude of 23.0 km and a zenith angle of 63° on 19 February 1975.

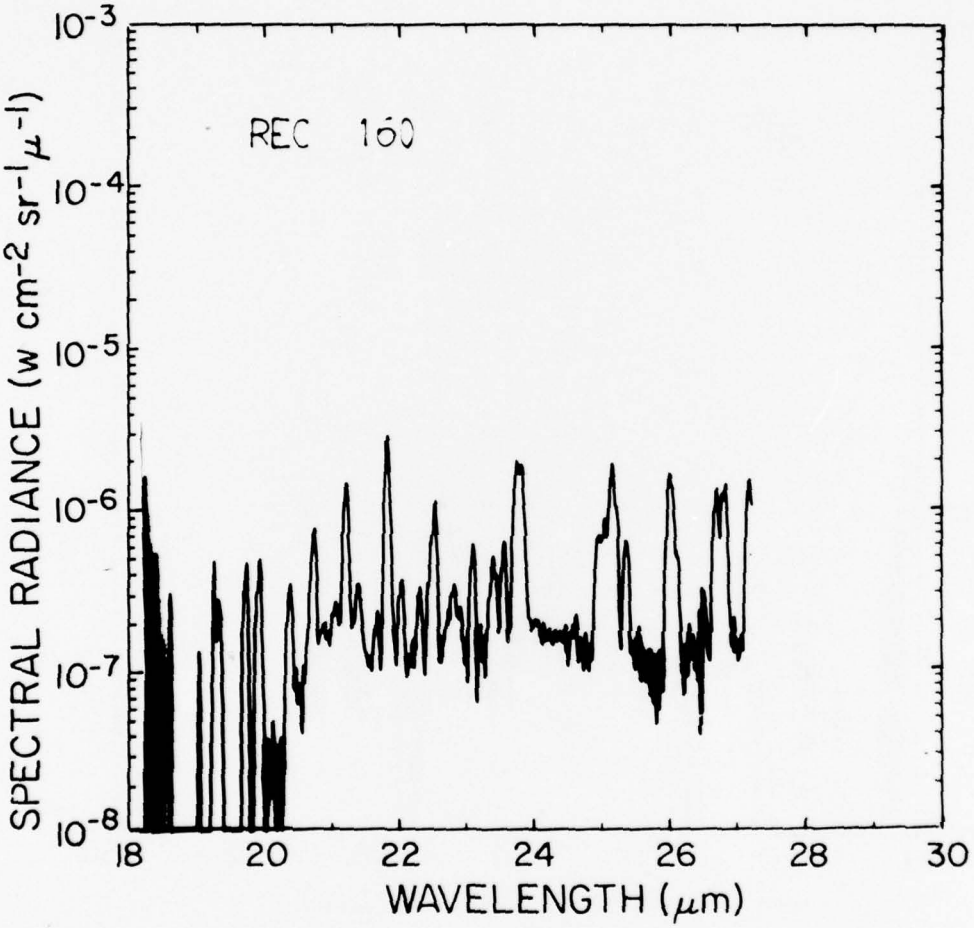

Figure 63. Sample spectrum of long wavelength region observed at an altitude of 24.6 km and a zenith angle of 63° on 19 February 1975.

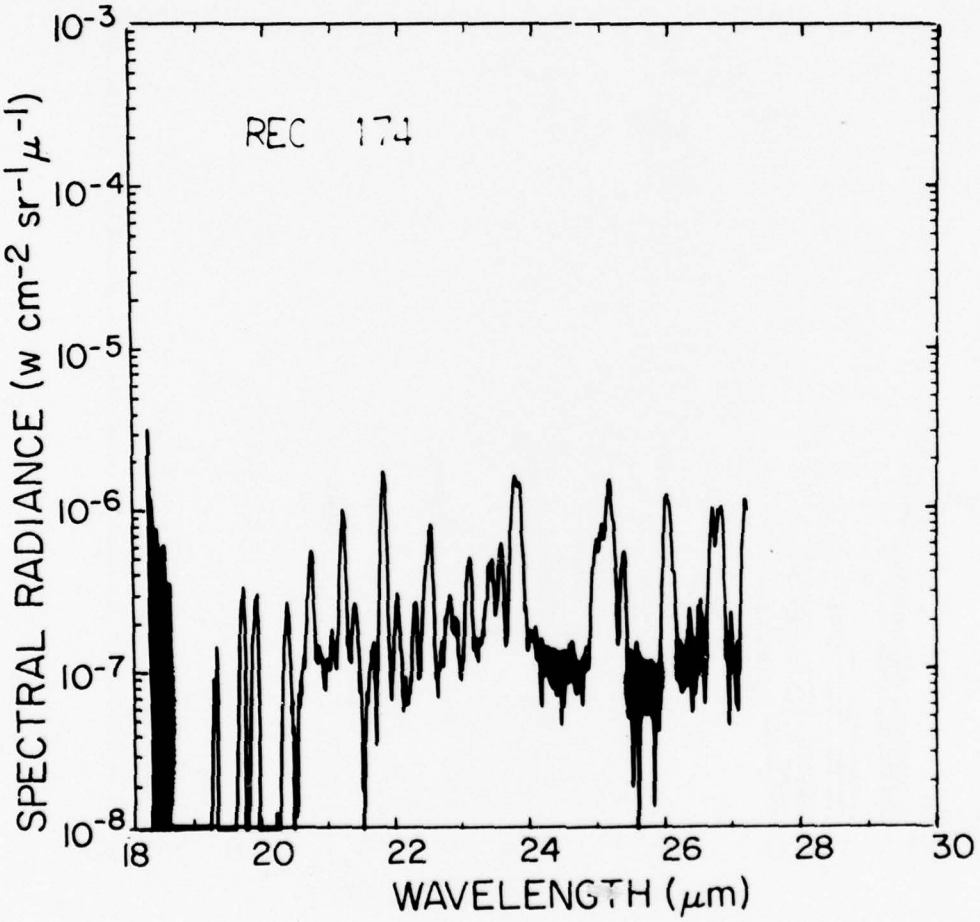

Figure 64. Sample spectrum of long wavelength region observed at an altitude of 26.5 km and a zenith angle of 63° on 19 February 1975.

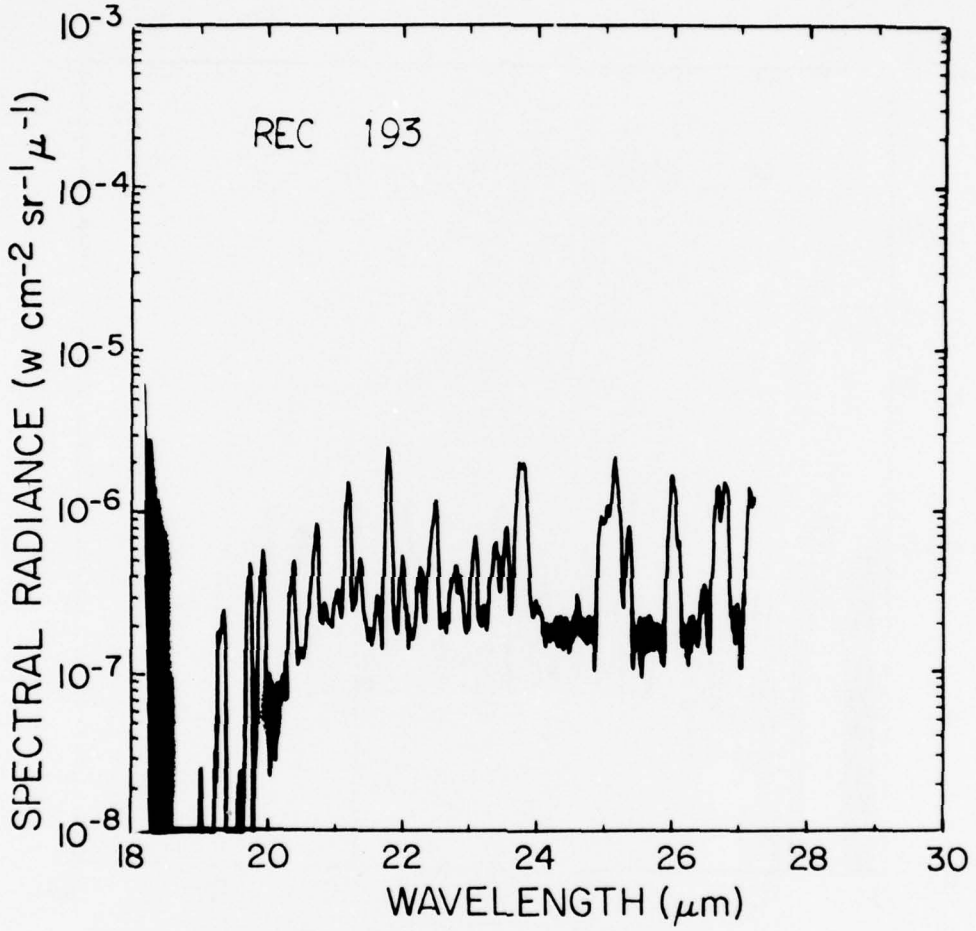

Figure 65. Sample spectrum of long wavelength region observed at an altitude of 28.6 km and a zenith angle of 78° on 19 February 1975.

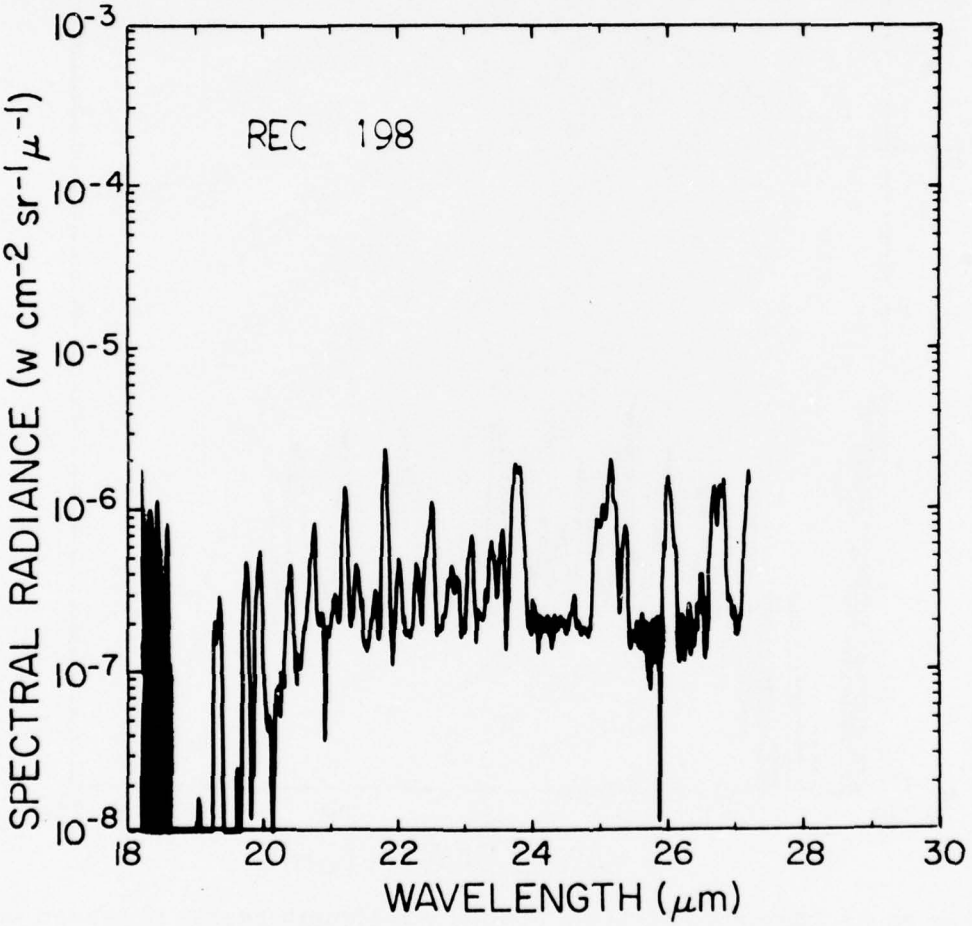

Figure 66. Sample spectrum of long wavelength region observed at an altitude of 29.0 km and a zenith angle of 78° on 19 February 1975.

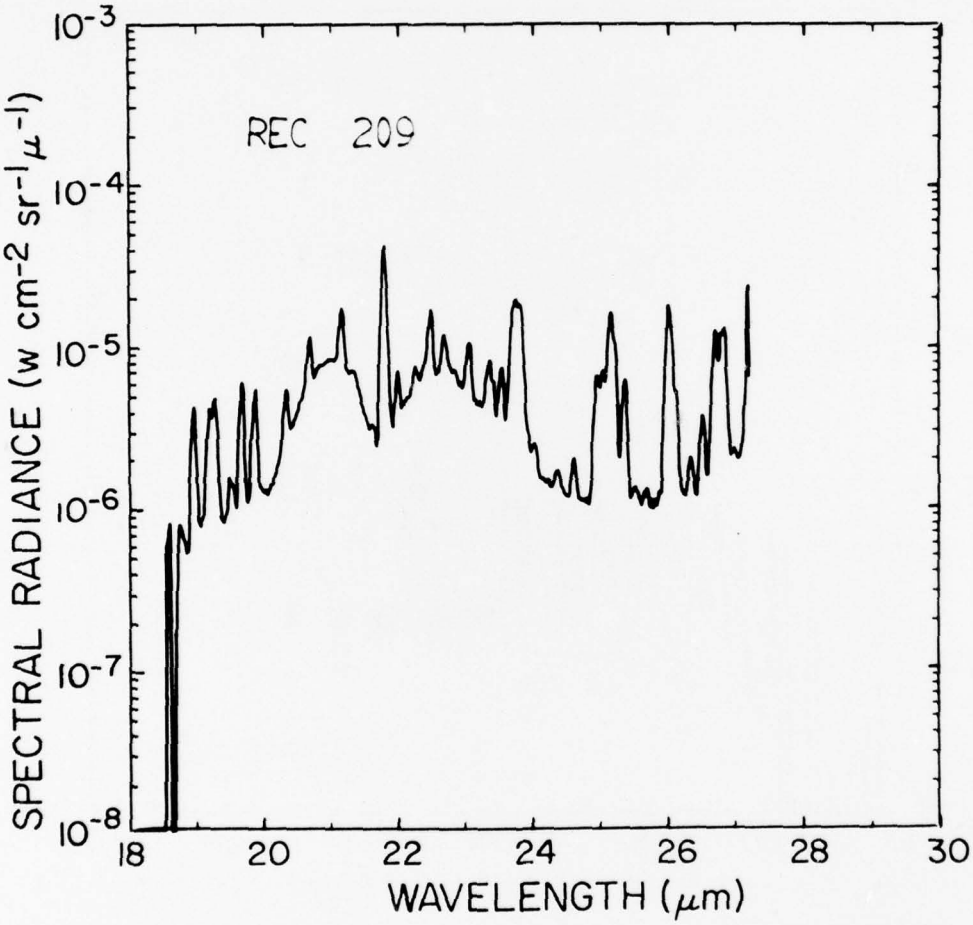

Figure 67. Sample spectrum of long wavelength region observed at an altitude of 29.1 km and a zenith angle of 93° on 19 February 1975.

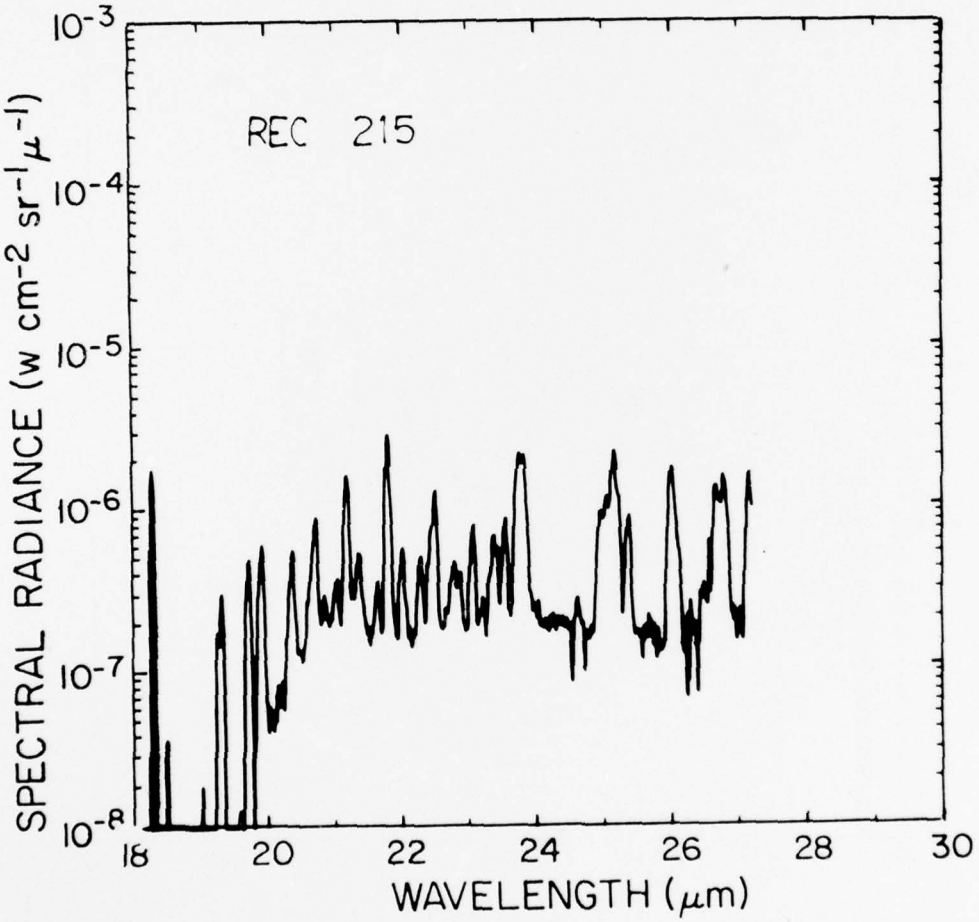

Figure 68. Sample spectrum of long wavelength region observed at an altitude of 29.1 km and a zenith angle of 81° on 19 February 1975.

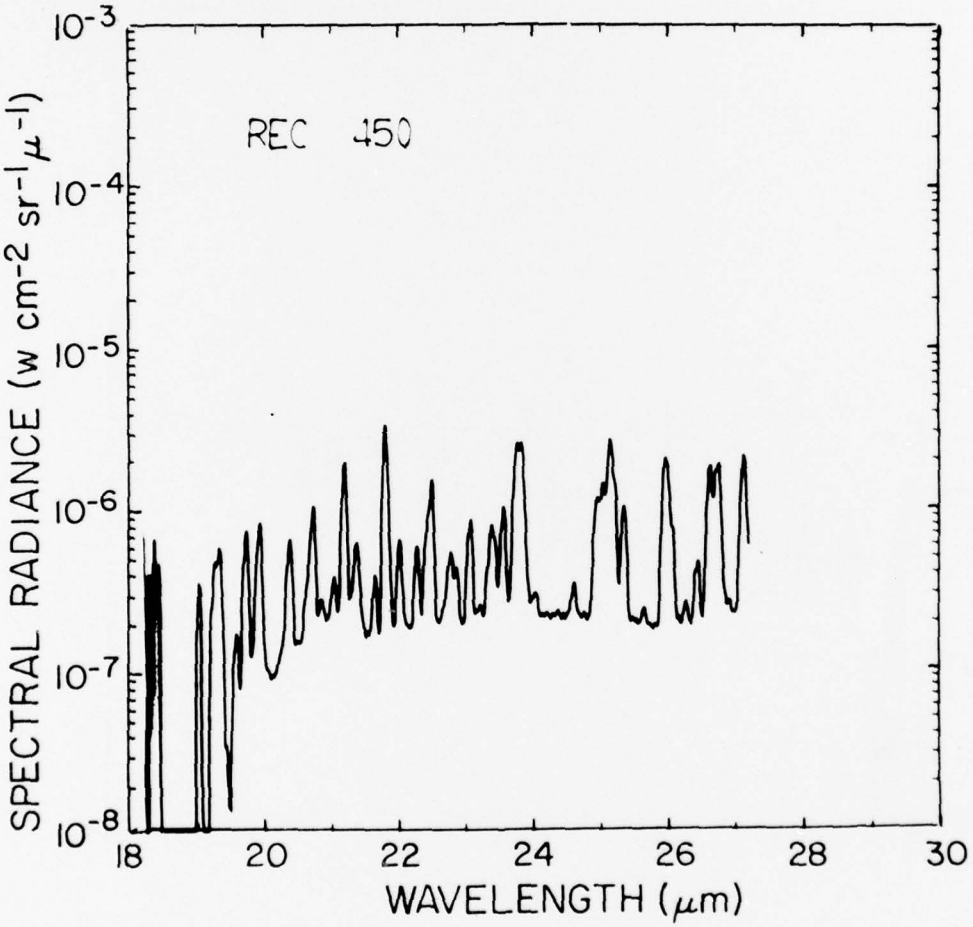

Figure 69. Sample spectrum of long wavelength region observed at an altitude of 29.1 km and a zenith angle of 81° on 19 February 1975.

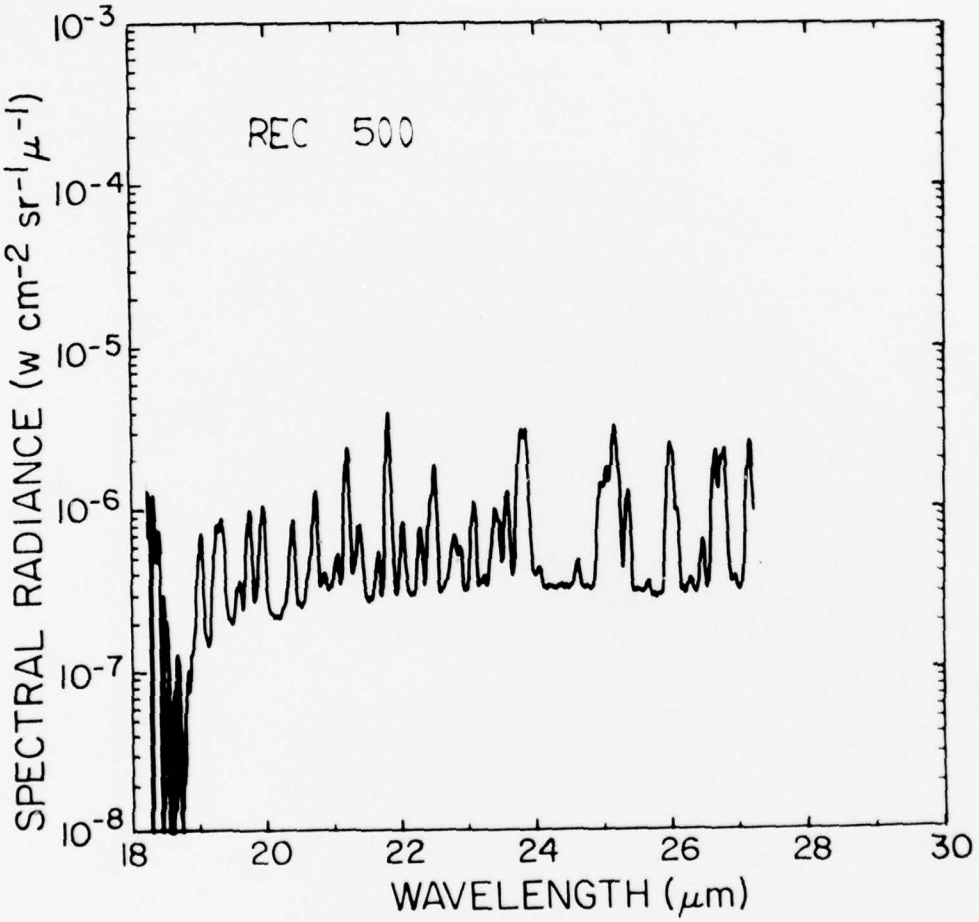

Figure 70. Sample spectrum of long wavelength region observed at an altitude of 29.1 km and a zenith angle of 81° on 19 February 1975.

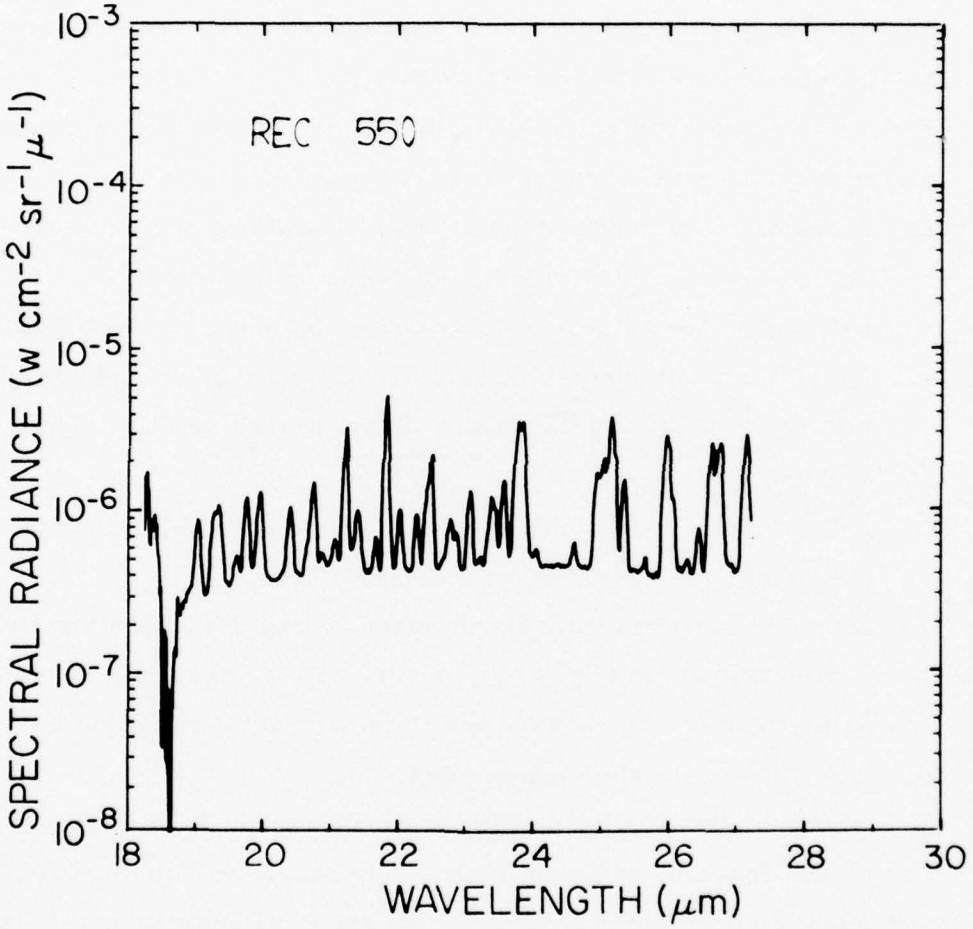

Figure 71. Sample spectrum of long wavelength region observed at an altitude of 29.1 km and a zenith angle of 81° on 19 February 1975.

After the spectral radiance is calculated some test of the accuracy of the values should be made. Such tests may contain comparisons with known or expected radiance values. Several examples of these tests are listed.

1. Comparison with a well made real time calibration (on-board black body). Care should be taken to avoid systematic errors.
2. Examination of spectral radiance for strong emission regions and comparison of this radiance with Planck black body radiance from an appropriate atmospheric temperature.
3. Fitting selected spectral regions to simple models over a range of emission parameters (pressure, secant, etc.).
   i. A linear mass model may fit weakly emitting regions such as "windows," provided the emission in the region is primarily due to uniformly mixed molecules (or particles).
   ii. Emission associated with selected strong line groups may be proportional to $\sqrt{Pw}$, where P is pressure and w is concentration.
   iii. Both i. and ii. and other models have predictable secant functions at a constant pressure altitude.
4. Repeatibility of measurements in spectral regions associated with known constituent concentrations such as CO_2 emissions
   i. over the duration of one experimental observing period,
   ii. over several observing periods.
5. Exploring the possibility that there may be specific known functional relationships between basic atmospheric parameters (P, T) and integrated radiance over selected spectral regions which can be used as
   i. pseudo calibration,
   ii. to infer an average black body radiance for the observational path. This is especially useful when adequate temperature profile data is missing. Again CO_2 regions may be suited for these purposes.

These examples are just that and each experiment will dictate its own tests. Spectral radiometric measurements offer many possibilities for such tests. In an attempt to explore some of these possibilities for the 27 June and 19 February flights, a number of wavelength regions were selected. Some of these regions have been labeled atmospheric windows and some contain emitted radiance from a specific atmospheric species. Table VII lists the regions investigated and the apparent dominant feature of each region. Average spectral radiances for each region were calculated from the measured radiances for all records of both flights. This data is presented in Table VIII for the 27 June 1974 flight and in Table IX for the 19 February 1975 flight. These average radiances are used in all the following discussions and constituent profile derivations. The average radiances have an arbitrary lower limit of 10^{-8} w cm^{-2} sr^{-1} μm^{-1}.

The following development is an attempt to test the data in the manner proposed under 3. i. and 3. ii. above. This discussion is not related to the derivation of the constituent profiles discussed in the following section. The inclusion here is of an exploratory nature with the possibility of developing techniques for quickly evaluating specific radiance data, techniques for inferring the mean atmospheric temperature when soundings are unavailable, or techniques to look for small variations in large amounts of data (i.e. possible seasonal changes in window radiance due to particulates.)

The average spectral radiances ($\overline{N}$) calculated in Tables VIII and IX were converted to emissivities in the following manner:

$$\epsilon = \frac{\overline{N}}{\overline{B}}$$

where

$$\overline{B} = \frac{\int_h^\infty f(B, n)\, dn}{\int_h^\infty dn}.$$

The integral $\int_h^\infty dn$ is the column density along the optical path and f(B, n) is the weighting function for the black body term related to successive density layers. Initially a linear weighting was used (f(B, n) = B(n)) in

Table VII. List of Spectral Regions of Interest

	Wavelength Range	Constituent of Interest
	Short Wavelength Region (2nd order)	
1.	8.85-8.90μm	9μm O_3
2.	9.475-9.500	9.6μm O_3 compare with Snider
3.	9.74-9.78	9.6μm O_3
4.	10.00-10.05	9.6μm O_3 wing
5.	10.405-10.410	center of CO_2
6.	10.465-10.550	CO_2
7.	10.690-10.700	window
8.	10.700-10.800	Freon 12
9.	10.800-10.815	window
10.	10.87-11.765	HNO_3 Band
11.	11.035-11.065	HNO_3
12.	11.215-11.315	HNO_3
13.	11.415-11.465	HNO_3
14.	11.845-11.925	window
15.	12.540	CO_2 Q-Branch edge
16.	12.540-12.670	CO_2 Q-Branch
17.	12.670	CO_2 Q-Branch edge
18.	13.205-13.265	CO_2
	Long Wavelength Region (1st order)	
19.	18.70-18.72μm	window
20.	20.75-21.02	HNO_3
21.	24.42-24.46	window
22.	24.67-24.78	window
23.	24.78-25.56	H_2O
24.	26.56	window
25.	25.72-25.76	window
26.	25.76-26.20	H_2O
27.	26.20	window
28.	26.37	window
29.	27.33-27.56	window

this calculation. $\bar{B}$ was calculated for each altitude of observation using at least 10 layers because the temperature lapse rate was generally not linear. Various possible functional relationships between emissivity and the emitting medium can be explored to determine which spectral regions can be described with simple extinction coefficients.

In general

$$\tau = 1 - \epsilon = e^{-f(m, p, T)},$$

where f(m, p, T) may be determined by line-by-line or band model calculations or some simple approximation to these more elaborate calculations, such as a linear coefficient with optical mass (m) or pressure weighted square root dependance ($\sqrt{Pm}$). For emissivities < 10% such approximations reduce to

$$\epsilon = a\beta m \text{ or } \epsilon = b\sqrt{P\beta m},$$

where $m = P \sec\theta$ and βm is the optical mass of a specific species.

Thus $\epsilon = a\beta P\sec\theta$ or $\epsilon = bP\sqrt{\beta\sec\theta} = bm\sqrt{\beta/\sec\theta}$.

Plots of ln ϵ vs ln m were made of some of the spectral regions for both flights and a few of these are discussed here as representative. Since both linear and square root regions are linear with air mass, such regions should be characterized by curves of slope 1 on a ln vs ln plot. This assumes that $\sec\theta$ is not varied. The $\sec\theta$ relationship can be identified by varying this parameter at a constant float altitude.

In the stratosphere a number of spectral regions should fit a linear model of weak non-overlapping lines. However, most of these regions are dominated by radiance from atmospheric constituents such as O_3 at 8.9μm and HNO_3 at 11.3μm, which are not uniformly mixed. Figure 72 shows a plot for HNO_3 where a linear mass function is assumed. The layering of the HNO_3 is quite apparent. The atmospheric window regions should fit the linear model; however, on these flights the effects due to the instrument window were removed based on assumptions about the radiance levels in the atmospheric windows so that a plot of that region only shows these assumptions.

Table VIII. Average radiance ($\mu w\ cm^{-2}\ sr^{-1}\ \mu m^{-1}$) calculated for each spectral region listed in Table VII for the 27 June 1974 flight.

Record	1	2	3	4	5	6	7	8	9	10	11	12	13	14	15	16	17	18
60	6.92	74.0	75.9	27.6	1.35	2.11	1.04	1.08	.948	1.79	1.36	2.32	1.49	2.25	5.80	9.07	4.84	0.00
64	6.75	67.3	71.8	26.5	1.22	1.55	.605	.711	.656	1.40	.863	2.29	1.15	1.40	3.82	6.84	4.24	0.00
69	6.43	67.1	69.9	26.7	1.02	1.25	.176	.405	.483	1.13	.754	1.93	.833	.771	2.99	5.61	3.91	0.00
73	6.42	64.0	68.9	27.0	.916	.955	.309	.399	.359	1.03	.793	1.71	.934	.621	2.77	5.06	3.59	0.00
78	6.03	62.8	68.1	25.5	.671	1.18	.099	.178	.356	1.00	.718	1.94	.888	.735	2.84	4.99	3.14	0.00
82	6.21	64.8	67.9	26.7	.964	.906	.556	.359	.294	.986	1.07	1.55	1.16	.342	2.36	4.56	3.80	0.00
86	6.29	65.1	67.3	26.8	.933	1.09	.220	.339	.348	1.04	.749	1.53	1.45	.207	1.94	4.30	3.79	0.00
94	6.45	66.2	67.4	26.8	1.22	1.05	.460	.546	.332	1.10	.986	1.84	1.08	.619	2.17	4.01	3.28	0.00
102	6.11	66.9	67.0	25.2	1.09	.817	.482	.375	.145	1.03	.882	1.74	.951	.515	2.05	4.33	3.31	0.00
105	5.78	63.1	65.5	23.9	.870	1.28	.611	.494	.306	2.29	.959	1.78	.952	.638	2.61	4.19	2.04	0.00
111	10.5	71.9	66.3	24.5	1.05	1.09	.519	.365	.267	.933	.801	1.56	.942	.317	2.13	3.47	2.64	0.00
116	5.54	35.7	29.0	20.2	.660	.897	.298	.368	.422	.790	.827	1.25	.771	.390	1.93	3.22	2.68	0.00
119	5.28	26.8	19.6	19.9	1.24	.545	.386	.264	.074	.662	.352	.826	.687	.729	1.96	3.48	1.85	0.00
127	4.59	41.0	36.1	20.5	.391	1.05	.423	.468	.381	.544	.589	.907	.679	.195	1.52	2.90	3.01	0.00
132	4.48	47.5	42.6	19.2	.801	.766	.332	.220	.302	.439	.425	.681	.349	.183	1.35	2.64	2.03	0.00
135	4.42	50.9	43.9	18.8	.597	.763	.178	.322	.163	.372	.318	.527	.580	.354	1.45	2.64	1.98	0.00
142	6.25	73.0	67.1	27.9	1.35	1.02	.696	.465	.293	.512	.475	.820	.553	.458	2.48	4.07	3.15	0.00
147	5.90	34.4	23.3	19.7	.891	1.17	.564	.455	.200	.389	.526	.640	.209	.274	2.06	3.93	2.61	0.00
152	5.07	31.7	33.1	21.5	.763	.874	.601	.385	.305	.267	.274	.349	.232	.460	1.84	3.47	2.58	0.00
156	5.19	51.1	46.2	21.9	.942	.873	.281	.200	.178	.238	.016	.158	.412	.305	1.85	3.29	2.06	0.00
160	4.77	59.2	53.6	21.4	1.18	.802	.580	.362	.237	.166	.209	.238	.011	.268	1.37	2.90	2.01	0.00
168	5.54	62.6	58.6	25.4	1.19	1.37	1.02	.344	.244	.212	.139	.206	.248	.377	2.02	3.76	2.58	0.00
180	4.45	57.0	51.2	22.7	1.11	.946	.605	.392	.105	.096	.189	.073	.052	.285	1.67	3.32	2.28	0.00
191	3.85	53.2	46.4	20.9	1.01	1.05	.554	.372	.136	.066	.117	.011	.050	.231	1.43	2.79	1.90	0.00
204	3.18	44.6	39.4	17.5	.900	.945	.504	.397	.291	.055	.078	.010	.012	.192	1.07	2.34	1.38	0.00
226	3.19	44.7	38.5	17.9	.978	1.14	.566	.431	.355	.085	.172	.029	.011	.252	1.16	2.39	1.48	0.00
247	3.34	48.3	41.9	19.3	1.27	1.30	.775	.614	.478	.176	.243	.112	.081	.362	1.30	2.62	1.63	0.00
275	7.04	77.1	72.3	35.6	2.64	2.27	1.47	1.13	.822	.341	.420	.226	.233	.702	2.94	5.63	3.72	0.00
280	27.5	178.	186.	97.4	7.95	5.05	2.80	2.32	1.97	3.50	3.24	4.95	3.70	2.91	12.4	19.5	15.8	0.00
283	27.3	181.	186.	99.2	7.96	4.98	2.89	2.41	1.95	3.55	3.25	5.02	3.78	2.90	12.5	19.6	16.1	0.00
286	28.7	182.	191.	100.	8.42	5.26	2.92	2.50	2.20	3.99	3.67	5.75	4.27	3.12	13.0	20.5	16.7	0.00
289	27.7	180.	189.	99.1	8.23	5.21	2.84	2.27	2.02	3.32	3.24	4.56	3.63	2.81	12.4	19.6	16.0	0.00
292	27.5	181.	190.	98.7	7.77	5.05	2.84	2.43	2.08	3.30	3.16	4.50	3.56	2.79	12.5	19.9	16.4	0.00
295	28.9	186.	195.	103.	8.13	5.29	3.06	2.56	2.20	3.98	3.89	5.60	4.33	3.02	13.4	20.9	17.1	0.00
298	29.5	186.	196.	104.	7.89	5.39	3.00	2.60	2.31	4.09	3.84	5.86	4.44	3.14	13.6	21.2	17.3	0.00

Table VIII. Average radiance ($\mu w\ cm^{-2}\ sr^{-1}\ \mu m^{-1}$) calculated for each spectral region listed in Table VII for the 27 June 1974 flight (Continued).

Record	19	20	21	22	23	24	25	26	27	28
60	29.8	.840	.366	.432	6.26	.557	.594	4.72	0.00	0.00
64	29.8	.338	.128	.141	2.70	.147	.175	2.36	0.00	0.00
69	29.8	.197	.087	.044	1.64	.071	.145	1.44	0.00	0.00
73	29.8	.150	.043	.032	1.11	.057	.081	1.02	0.00	0.00
78	29.8	.148	.057	.031	.761	.035	.027	.717	0.00	0.00
82	29.8	.149	.025	.052	.618	.037	.027	.529	0.00	0.00
86	29.8	.135	.039	.049	.527	.010	.014	.416	0.00	0.00
94	29.8	.152	.062	.045	.500	.021	.043	.374	0.00	0.00
102	29.8	.152	.051	.105	.489	.040	.075	.394	0.00	0.00
105	29.8	.150	.126	.106	.481	.115	.115	.352	0.00	0.00
111	29.8	.158	.071	.077	.404	.049	.056	.316	0.00	0.00
116	29.8	.129	.082	.061	.374	.059	.061	.259	0.00	0.00
119	29.8	.108	.062	.061	.351	.041	.087	.246	0.00	0.00
127	29.8	.087	.082	.046	.309	.057	.031	.221	0.00	0.00
132	29.8	.064	.070	.072	.288	.012	.133	.195	0.00	0.00
135	29.8	.046	.044	.053	.257	.065	.112	.248	0.00	0.00
142	29.8	.111	.091	.060	.332	.010	.055	.226	0.00	0.00
147	29.8	.065	.078	.052	.308	.014	.028	.197	0.00	0.00
152	29.8	.059	.057	.058	.263	.024	.104	.179	0.00	0.00
156	29.8	.072	.063	.075	.233	.010	.092	.188	0.00	0.00
160	29.8	.059	.080	.039	.225	.076	.067	.159	0.00	0.00
168	29.8	.031	.073	.054	.260	.037	.057	.179	0.00	0.00
180	29.8	.034	.053	.051	.228	.059	.026	.135	0.00	0.00
191	29.8	.018	.029	.062	.197	.066	.061	.110	0.00	0.00
204	29.8	.019	.065	.036	.173	.017	.042	.104	0.00	0.00
226	29.8	.026	.086	.072	.191	.033	.080	.128	0.00	0.00
247	29.8	.044	.093	.095	.231	.108	.076	.144	0.00	0.00
275	29.8	.115	.140	.135	.357	.106	.104	.211	0.00	0.00
280	29.8	.597	.241	.211	1.03	.222	.158	.632	0.00	0.00
283	29.8	.613	.241	.210	1.08	.240	.187	.619	0.00	0.00
286	29.8	.695	.245	.235	1.10	.187	.194	.684	0.00	0.00
289	29.8	.582	.243	.220	1.03	.200	.160	.646	0.00	0.00
292	29.8	.599	.248	.231	1.04	.207	.159	.672	0.00	0.00
295	29.8	.718	.294	.259	1.13	.287	.167	.753	0.00	0.00
298	29.8	.729	.254	.254	1.13	.237	.128	.796	0.00	0.00

Table VIII. Average radiance ($\mu w\ cm^{-2}\ sr^{-1}\ \mu m^{-1}$) calculated for each spectral region listed in Table VII for the 27 June 1974 flight (Continued).

Record	1	2	3	4	5	6	7	8	9	10	11	12	13	14	15	16	17	18
301	28.6	184.	194.	102.	8.01	5.34	3.03	2.53	2.22	3.45	3.38	5.01	3.33	2.93	13.0	20.3	16.5	0.00
304	28.9	185.	195.	104.	8.27	5.43	3.05	2.67	2.26	3.92	3.76	5.46	4.65	3.00	13.5	21.2	17.6	0.00
318	2.10	33.8	29.6	9.92	1.80	1.73	1.27	1.22	1.13	.742	.906	.713	.682	.734	1.10	1.78	1.51	0.00
346	2.46	36.5	33.2	12.1	1.74	1.67	1.18	1.11	1.05	.602	.750	.542	.485	.611	1.25	1.93	1.50	0.00
361	3.00	41.5	38.4	16.8	1.52	1.50	.957	.810	.713	.327	.479	.247	.192	.416	1.27	2.37	1.59	0.00
375	3.74	44.3	41.2	19.8	1.50	1.40	.852	.728	.598	.168	.326	.082	.070	.201	1.35	2.73	1.84	0.00
389	5.71	56.8	57.2	29.0	1.87	1.69	.939	.725	.522	.067	.158	.010	.010	.230	2.13	4.38	2.86	0.00
396	20.3	118.	130.	70.7	5.20	3.04	1.45	1.18	1.12	2.15	2.19	3.45	2.62	.903	8.54	13.8	11.5	0.00
403	19.5	114.	125.	67.1	4.49	2.78	1.21	1.05	.969	1.94	2.09	3.27	2.42	.575	8.03	13.1	11.2	0.00
409	19.0	114.	121.	67.2	5.21	2.75	1.20	.973	.895	1.84	1.92	3.07	2.32	.529	7.61	12.5	10.7	0.00

Table VIII. Average radiance ($\mu w\ cm^{-2}\ sr^{-1}\ \mu m^{-1}$) calculated for each spectral region listed in Table VII for the 27 June 1974 flight (Continued).

Record	19	20	21	22	23	24	25	26	27	28
301	29.8	.647	.277	.267	1.09	.894	.163	.734	0.00	0.00
304	29.8	.675	.278	.259	1.13	.216	.135	.743	0.00	0.00
318	29.8	.213	.254	.230	.311	.215	.193	.179	0.00	0.00
346	29.8	.217	.260	.257	.338	.213	.217	.199	0.00	0.00
361	29.8	.147	.179	.165	.270	.124	.108	.137	0.00	0.00
375	29.8	.108	.138	.132	.244	.081	.073	.104	0.00	0.00
389	29.8	.069	.092	.079	.245	.068	.010	.079	0.00	0.00
396	29.8	.409	.072	.025	.635	.010	.010	.274	0.00	0.00
403	29.8	.384	.049	.038	.604	.010	.010	.248	0.00	0.00
409	29.8	.384	.035	.012	.570	.010	.010	.213	0.00	0.00

Table IX. Average radiance ($\mu w\ cm^{-2}\ sr^{-1}\ \mu m^{-1}$) calculated for each spectral region listed in Table VII for the 19 February 1975 flight.

Record	1	2	3	4	5	6	7	8	9	10	11	12	13	14	15	16	17	18
47	8.19	101.	99.6	31.2	2.64	4.44	3.26	2.77	3.67	3.64	1.80	4.23	2.81	4.15	14.5	17.3	9.48	39.6
50	7.78	97.6	96.7	30.5	2.36	3.71	2.29	2.43	3.05	3.34	1.82	5.39	2.72	7.93	11.9	14.7	6.99	34.0
53	7.28	93.4	91.7	31.2	2.31	2.90	1.81	1.91	2.19	2.76	1.63	4.20	2.33	7.88	8.27	12.0	5.59	29.0
56	6.78	87.0	88.1	30.3	2.15	2.54	1.54	1.65	1.94	2.32	1.51	3.17	2.02	5.82	6.15	9.93	4.91	24.6
59	6.58	84.6	85.0	30.2	1.96	2.14	1.26	1.38	1.60	2.05	1.39	2.71	1.93	4.06	4.74	8.19	4.28	21.3
62	6.15	83.2	83.5	28.2	1.43	1.62	.801	.910	1.18	1.76	1.23	2.43	1.72	3.03	3.73	6.87	3.54	19.4
65	5.70	80.4	81.1	25.9	.972	1.22	.528	.618	.828	1.45	1.04	2.13	1.49	2.12	2.98	5.82	2.99	17.6
68	5.49	77.9	78.0	25.2	.899	1.11	.453	.514	.741	1.41	1.05	2.17	1.48	1.46	2.59	5.26	2.76	16.0
71	5.47	75.9	76.3	23.5	.738	.975	.310	.391	.542	1.32	1.04	2.11	1.45	.884	2.03	4.52	2.21	14.5
73	5.19	74.5	72.2	21.0	.583	.795	.308	.343	.511	1.19	.996	2.02	1.30	.637	1.83	4.10	2.11	14.0
75	5.23	73.4	73.0	22.2	.592	.804	.064	.233	.373	1.12	.915	1.91	1.31	.614	1.69	3.89	1.95	13.3
77	5.29	71.3	71.3	21.4	.601	.685	.197	.203	.358	1.15	.835	1.91	1.35	.515	1.65	3.58	2.09	12.7
79	5.11	72.5	69.5	21.0	.630	.749	.274	.270	.394	1.07	.844	1.81	1.24	.502	1.45	3.47	1.84	12.2
85	5.00	72.7	69.7	21.7	.637	.631	.187	.210	.296	1.03	.978	1.85	1.13	.339	1.40	3.05	1.80	11.6
88	4.84	67.1	66.0	20.7	.624	.855	.219	.225	.340	1.12	1.00	1.91	1.30	.390	1.22	2.89	1.53	10.5
92	4.65	67.7	65.1	19.7	.560	.631	.210	.218	.298	1.03	.888	1.76	1.21	.342	1.01	2.47	1.41	9.45
97	4.19	60.0	55.6	18.1	.532	.540	.150	.147	.185	.875	.825	1.49	1.03	.187	.790	2.14	1.12	8.62
100	3.90	57.6	53.2	16.7	.333	.421	.152	.125	.174	.845	.755	1.46	.984	.095	.747	1.85	1.03	7.76
102	3.99	54.3	51.1	17.0	.528	.450	.146	.087	.136	.807	.657	1.38	.998	.078	.639	1.82	1.04	7.76
105	3.86	54.2	51.0	16.8	.514	.386	.080	.030	.245	.809	.661	1.39	1.03	.185	.663	1.66	1.01	6.93
109	3.75	49.1	48.3	15.8	.471	.474	.139	.111	.133	.816	.784	1.47	1.00	.134	.668	1.58	1.05	6.82
113	3.57	50.8	47.2	15.8	.521	.442	.136	.103	.135	.747	.663	1.35	1.02	.146	.505	1.36	1.04	6.85
115	3.25	53.6	48.3	16.8	.395	.557	.095	.078	.142	.740	.767	1.32	.949	.064	.524	1.37	.956	7.34
118	3.53	50.5	46.5	16.2	.515	.464	.122	.099	.136	.760	.672	1.32	.979	.141	.537	1.31	.789	6.24
121	3.44	51.4	45.4	16.1	.530	.426	.145	.092	.121	.670	.565	1.16	.884	.059	.428	1.26	.716	6.13
124	3.44	50.9	45.7	16.2	.426	.382	.100	.073	.069	.600	.514	1.05	.764	.088	.476	1.16	.736	5.59
126	3.16	50.2	44.9	16.4	.552	.413	.086	.097	.010	.591	.474	1.03	.779	.093	.521	1.18	1.07	5.76
129	3.03	49.4	42.7	14.8	.437	.378	.127	.119	.033	.560	.488	1.00	.765	.093	.469	1.11	.543	5.58
133	2.80	48.4	42.7	13.6	.379	.386	.129	.094	.117	.518	.454	.882	.692	.114	.405	1.06	.626	5.23
136	2.67	45.2	37.6	11.4	.474	.317	.057	.113	.279	.485	.530	.797	.577	.117	.734	.993	1.03	3.87
139	2.68	46.2	39.3	14.3	.394	.351	.114	.133	.073	.454	.360	.720	.612	.121	.437	1.10	.660	4.54
142	2.34	44.3	38.4	14.3	.533	.350	.185	.114	.050	.441	.339	.645	.613	.156	.172	.939	.638	4.64
147	2.36	44.6	35.7	13.3	.436	.352	.136	.130	.118	.371	.329	.618	.511	.136	.224	.852	.627	4.55
149	2.24	42.7	35.7	13.1	.362	.308	.163	.108	.090	.346	.281	.566	.449	.114	.350	.897	.435	4.11
152	2.29	41.0	34.7	13.5	.419	.301	.098	.092	.038	.299	.232	.481	.438	.071	.372	.814	.465	3.65

Table IX. Average radiance ($\mu w\ cm^{-2}\ sr^{-1}\ \mu m^{-1}$) calculated for each spectral region listed in Table VII for the 19 February 1975 flight (Continued).

Record	19	20	21	22	23	24	25	26	27	28
47	6.58	19.8	11.1	15.6	70.3	18.0	19.2	62.7	29.5	24.4
50	4.38	13.4	6.86	9.81	57.8	10.8	12.1	50.5	17.4	14.0
53	2.82	8.75	3.58	4.69	40.8	5.28	6.09	36.1	8.70	7.18
56	2.57	5.50	2.09	2.68	29.2	3.09	3.46	26.6	4.94	4.04
59	1.38	4.13	1.45	1.77	21.1	2.01	2.26	19.8	2.95	2.43
62	.590	2.80	1.08	1.30	17.2	1.51	1.69	16.7	2.19	1.94
65	.150	1.98	.797	.941	14.0	1.11	1.24	13.9	1.80	1.55
68	.179	1.44	.669	.737	11.1	.867	.913	11.1	1.29	1.22
71	.010	1.13	.483	.516	8.16	.590	.668	8.50	.934	.877
73	.014	.903	.367	.396	6.11	.431	.429	6.39	.693	.686
75	.010	.840	.282	.298	5.04	.362	.382	5.20	.561	.518
77	.010	.727	.222	.225	4.03	.301	.309	4.41	.453	.412
79	.010	.741	.273	.231	3.64	.202	.261	3.92	.436	.471
85	.012	.707	.240	.237	3.29	.199	.212	3.19	.364	.425
88	.045	.716	.229	.234	3.13	.215	.243	3.24	.320	.394
92	.044	.692	.241	.207	2.78	.218	.207	2.85	.570	.371
97	.081	.615	.203	.166	2.38	.222	.214	2.49	.346	.310
100	.024	.511	.215	.197	2.10	.194	.170	2.19	.467	.361
102	.010	.544	.158	.174	1.99	.169	.202	2.18	.362	.199
105	.010	.482	.183	.194	1.79	.155	.169	1.82	.265	.194
109	.052	.500	.169	.183	1.64	.242	.150	1.67	.196	.232
113	.025	.509	.169	.162	1.43	.160	.136	1.51	.195	.205
115	.010	.423	.184	.178	1.38	.166	.157	1.32	.045	.194
118	.053	.501	.191	.166	1.32	.157	.177	1.32	.226	.196
121	.010	.445	.195	.166	1.20	.201	.162	1.27	.187	.184
124	.010	.390	.180	.178	1.09	.146	.152	1.07	.122	.166
126	.010	.446	.187	.127	1.08	.139	.163	1.09	.197	.166
129	.059	.395	.179	.157	1.01	.197	.142	1.03	.165	.092
133	.010	.366	.201	.172	.944	.162	.154	.935	.106	.144
136	.087	.640	.202	.457	.815	.166	.392	.822	.146	.122
139	.010	.324	.198	.182	.853	.171	.147	.792	.128	.159
142	.010	.312	.182	.190	.814	.196	.163	.817	.202	.161
147	.010	.282	.196	.160	.741	.140	.153	.698	.153	.143
149	.010	.227	.174	.162	.734	.150	.162	.658	.176	.107
152	.010	.221	.107	.172	.687	.077	.167	.628	.045	.108

Table IX. Average radiance ($\mu w\ cm^{-2}\ sr^{-1}\ \mu m^{-1}$) calculated for each spectral region listed in Table VII for the 19 February 1975 flight (Continued).

Record	1	2	3	4	5	6	7	8	9	10	11	12	13	14	15	16	17	18
157	2.18	39.3	32.3	12.5	.438	.316	.158	.108	.024	.249	.184	.384	.352	.117	.308	.764	.389	3.87
160	1.83	40.1	31.3	12.1	.362	.266	.103	.095	.110	.188	.141	.279	.271	.133	.107	.679	.230	3.64
163	1.86	38.3	27.3	11.8	.439	.281	.136	.099	.129	.167	.072	.217	.303	.050	.288	.567	.164	3.38
166	1.59	38.3	28.9	12.2	.487	.290	.130	.096	.057	.161	.123	.212	.271	.038	.010	.593	.738	3.08
170	1.66	35.1	28.2	11.6	.394	.190	.145	.070	.033	.149	.124	.177	.274	.012	.173	.588	.308	3.02
174	1.55	35.2	28.0	11.5	.392	.241	.086	.049	.010	.099	.086	.145	.119	.030	.101	.572	.329	2.92
177	1.45	32.2	25.0	11.2	.443	.234	.058	.036	.010	.084	.016	.115	.171	.016	.031	.394	.234	2.65
182	1.28	29.7	24.6	10.9	.428	.152	.054	.026	.037	.062	.025	.070	.083	.011	.054	.447	.161	2.38
187	1.04	28.3	22.9	11.1	.448	.182	.112	.027	.045	.029	.012	.037	.033	.014	.065	.463	.289	2.08
190	1.29	29.4	23.2	10.8	.327	.197	.044	.035	.023	.028	.010	.025	.054	.019	.010	.427	.138	1.90
193	2.69	46.7	40.0	18.7	.772	.415	.126	.060	.099	.187	.259	.278	.268	.157	.224	1.19	.787	4.96
196	2.42	45.2	38.6	18.4	.595	.344	.269	.094	.028	.150	.083	.210	.103	.130	.408	1.18	.770	4.80
198	2.40	45.5	39.1	18.0	.729	.372	.094	.102	.106	.148	.037	.232	.299	.095	.508	1.26	.809	5.35
201	2.85	45.1	38.6	17.9	.338	.390	.010	.086	.010	.145	.093	.200	.250	.273	.900	1.56	.538	5.81
202	3.59	53.0	48.7	24.5	1.10	.762	.231	.159	.412	.260	.179	.329	.332	.237	.876	2.18	1.46	6.79
207	6.53	69.2	71.7	34.5	1.61	.929	.403	.275	.269	.673	.708	.953	.816	.487	2.28	3.98	3.48	11.4
209	22.0	87.7	96.8	67.2	3.56	2.08	1.57	1.89	2.43	14.6	13.5	22.8	19.2	2.91	10.2	14.6	13.3	44.0
215	2.80	48.3	42.8	20.6	.749	.523	.120	.067	.225	.158	.069	.196	.247	.115	.628	1.47	.603	5.82
222	2.86	47.8	43.0	19.2	.464	.430	.180	.111	.022	.156	.148	.208	.247	.106	.665	1.43	.949	5.26
235	2.69	45.9	41.3	19.3	.667	.372	.103	.079	.103	.154	.120	.208	.227	.039	.771	1.34	.887	5.59
248	2.51	45.5	39.8	18.7	.605	.378	.172	.104	.048	.148	.036	.155	.220	.077	.397	1.31	.850	5.50
256	2.59	44.1	38.5	18.3	.750	.339	.108	.060	.035	.144	.068	.188	.137	.072	.755	1.30	.732	5.02
271	2.46	43.1	38.1	18.4	.636	.396	.108	.064	.011	.120	.128	.155	.174	.045	.595	1.25	.837	5.13
282	2.31	42.5	37.3	18.0	.701	.401	.020	.146	.037	.114	.087	.153	.180	.027	.558	1.23	.590	4.97
300	2.61	44.4	39.9	19.1	.788	.408	.119	.079	.011	.103	.036	.162	.203	.061	.529	1.30	.865	5.27
350	2.86	47.6	44.0	21.0	.808	.470	.163	.094	.045	.092	.046	.148	.159	.060	.579	1.55	.853	5.72
400	3.23	52.5	48.7	23.6	.949	.562	.199	.104	.038	.104	.048	.164	.191	.090	.748	1.74	.997	5.93
450	3.72	61.5	56.3	28.1	1.31	.757	.326	.208	.110	.188	.123	.278	.267	.185	.939	2.06	1.22	6.65
500	4.36	71.9	65.0	32.0	1.50	.984	.477	.329	.219	.331	.260	.463	.405	.312	1.17	2.42	1.49	7.82
550	4.53	80.3	70.2	36.8	1.82	1.11	.616	.457	.326	.443	.400	.596	.517	.392	1.24	2.58	1.68	7.85
600	4.53	85.6	68.8	37.2	1.97	1.11	.682	.555	.455	.552	.543	.734	.620	.374	1.29	2.73	1.76	7.95
689	4.58	93.7	62.7	30.1	1.66	1.04	.764	.684	.586	.594	.638	.759	.635	.290	1.39	2.84	1.86	7.64
764	4.35	94.8	59.7	26.7	1.49	1.10	.695	.627	.552	.362	.467	.377	.386	.061	1.14	2.42	1.48	6.23

Table IX. Average radiance ($\mu w\ cm^{-2}\ sr^{-1}\ \mu m^{-1}$) calculated for each spectral region listed in Table VII for the 19 February 1975 flight (Continued).

Record	19	20	21	22	23	24	25	26	27	28
157	.010	.237	.129	.128	.613	.132	.125	.590	.127	.198
160	.010	.198	.165	.133	.567	.162	.076	.524	.070	.100
163	.010	.219	.154	.087	.462	.136	.118	.517	.074	.098
166	.010	.215	.153	.161	.528	.111	.087	.453	.291	.125
170	.010	.179	.092	.104	.490	.069	.078	.434	.077	.077
174	.010	.154	.096	.087	.467	.087	.090	.403	.130	.189
177	.010	.192	.088	.059	.419	.047	.070	.398	.092	.103
182	.010	.123	.091	.085	.395	.079	.076	.313	.089	.130
187	.010	.156	.104	.078	.384	.028	.047	.318	.060	.040
190	.010	.133	.090	.081	.370	.067	.072	.321	.048	.013
193	.010	.271	.175	.186	.679	.172	.157	.573	.176	.145
196	.010	.285	.190	.154	.673	.173	.111	.540	.130	.136
198	.010	.232	.201	.181	.671	.186	.136	.541	.168	.177
201	.010	.225	.177	.193	.736	.152	.188	.585	.182	.122
202	.010	.362	.204	.225	.823	.129	.241	.652	.151	.215
207	.010	.549	.281	.263	1.22	.264	.210	1.01	.195	.372
209	.061	7.70	1.33	1.13	5.23	1.25	1.08	5.48	1.37	1.86
215	.010	.271	.190	.153	.707	.144	.158	.571	.121	.133
222	.010	.240	.168	.163	.684	.173	.148	.538	.098	.117
235	.010	.278	.178	.165	.680	.143	.128	.511	.076	.086
248	.010	.264	.163	.167	.658	.153	.138	.498	.110	.105
256	.010	.253	.165	.164	.638	.140	.129	.488	.089	.132
271	.010	.244	.161	.156	.623	.132	.118	.473	.097	.098
282	.010	.231	.138	.140	.599	.103	.121	.463	.067	.096
300	.010	.233	.149	.143	.618	.115	.112	.472	.033	.121
350	.010	.204	.126	.119	.635	.102	.104	.497	.086	.093
400	.010	.218	.141	.134	.704	.121	.113	.562	.109	.136
450	.010	.346	.215	.221	.891	.196	.191	.722	.195	.225
500	.082	.445	.336	.333	1.11	.312	.298	.925	.309	.314
550	.125	.632	.450	.446	1.30	.414	.391	1.08	.417	.454
600	.122	.830	.604	.596	1.51	.537	.522	1.25	.511	.535
689	.010	1.00	.783	.774	1.74	.693	.672	1.44	.643	.653
764	.010	1.03	.762	.747	1.68	.677	.635	1.33	.576	.644

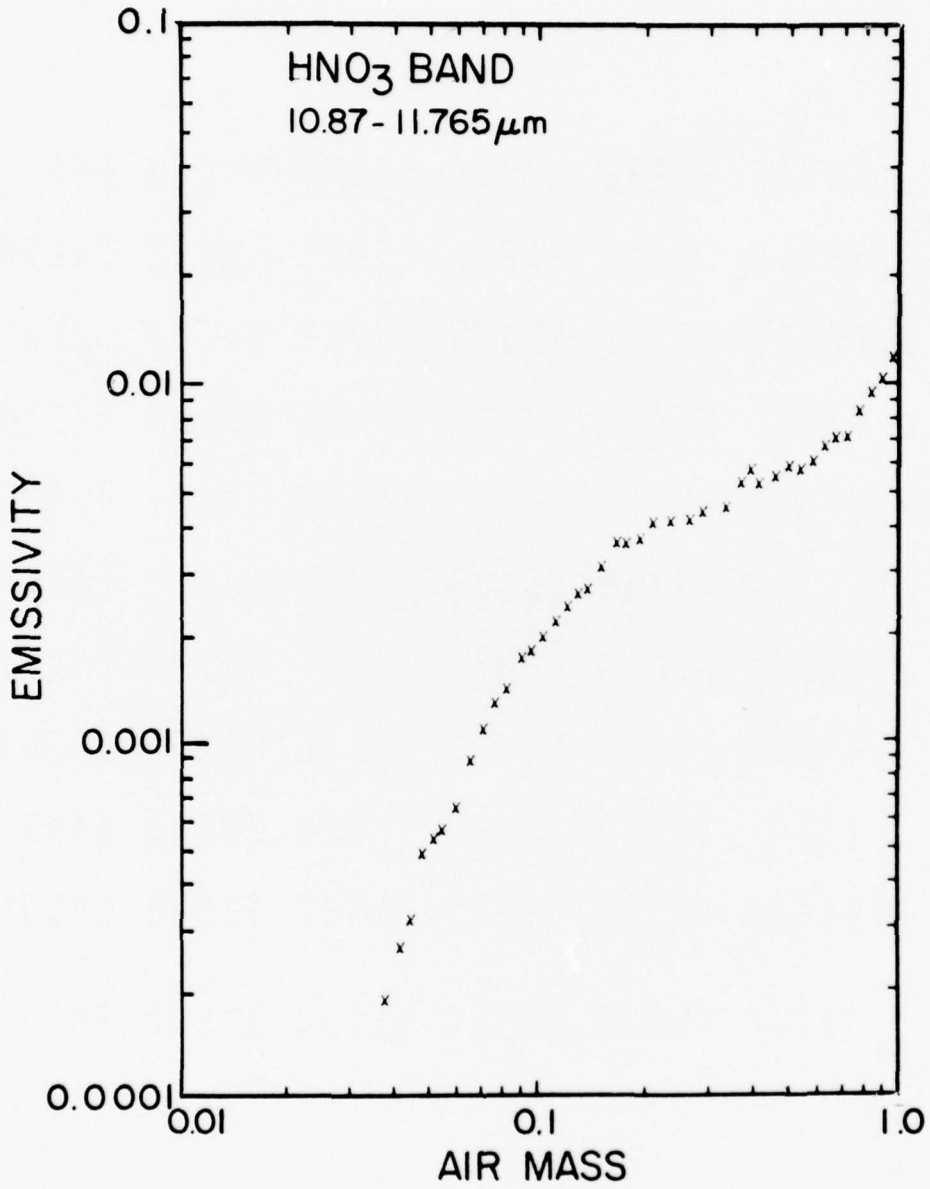

Figure 72. Plot of emissivity vs air mass for spectral region number 10, 19 February 1975.

The 25μm region of H_2O emission is composed of strong randomly spaced, non-overlapping lines and should fit a $\sqrt{Pm}$ type model. Figure 73 shows a plot of this region which is nearly linear with m. The square root relationship was confirmed with data from this and a later flight where several secant scans were made at a constant pressure altitude. These plots will be shown in a later report. Note that while the water vapor is not uniformly mixed with altitude, it is sufficiently close to uniform in the stratosphere that a functional relationship containing the square root of the mixing ratio plotted on the scale used in Figure 73 appears to be a straight line.

The spectral region which includes a CO_2 Q-Branch at 12.6μm is plotted in Figure 74. This region consists of a large number of weak but overlapping lines. The plot could be fit with a linear curve but the best slope is not 1 and plots of the secant variation indicate a slope less than one. Thus the overlapping lines modify the linear model as expected.

Figures 72 to 74 and the above discussion about them show some of the considerations necessary to use 3. i. and 3. ii. A later report will explore these points further.

A further test example using 2 above pertains to two strong absorption regions: one at 9.7μm due to O_3, the other at 25.2μm due to H_2O. The near center of the 9.6μm band becomes totally black when observed over long optical paths in the stratosphere. The measured radiance levels are therefore defined by the stratospheric temperatures at appropriate altitudes. Figure 44 illustrates this point as the center of the O_3 band lost much of its spectral characteristics and appears more as a short segment of a black body curve at an appropriate temperature for the lower stratosphere. Similarly, the 25.2μm emission from H_2O is totally black at low altitudes in the troposphere and can be used to check calibrations. This check has been made on some later flights but the spectral data shown in this report do not include data from low enough altitudes to show this effect.

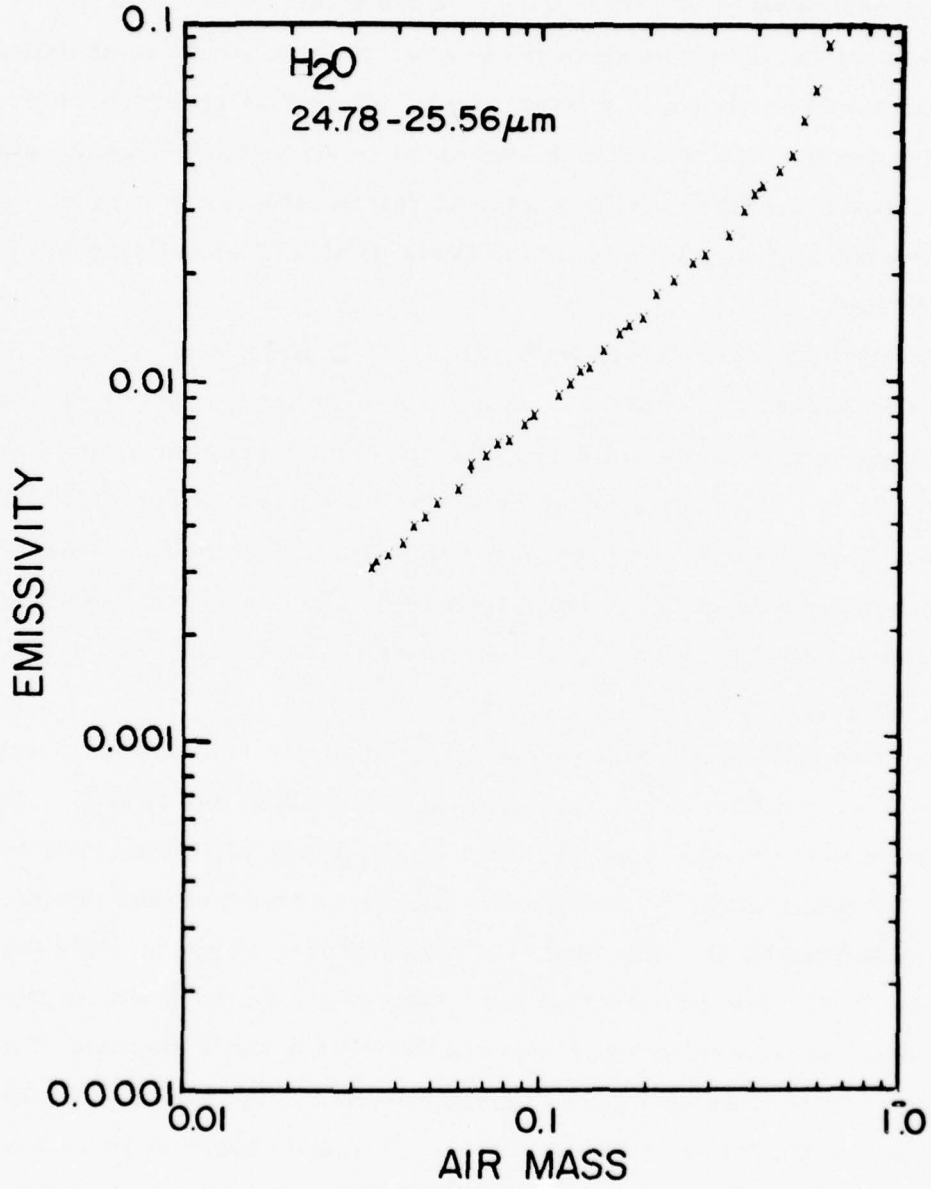

Figure 73. Plot of emissivity vs air mass for spectral region number 23, 19 February 1975.

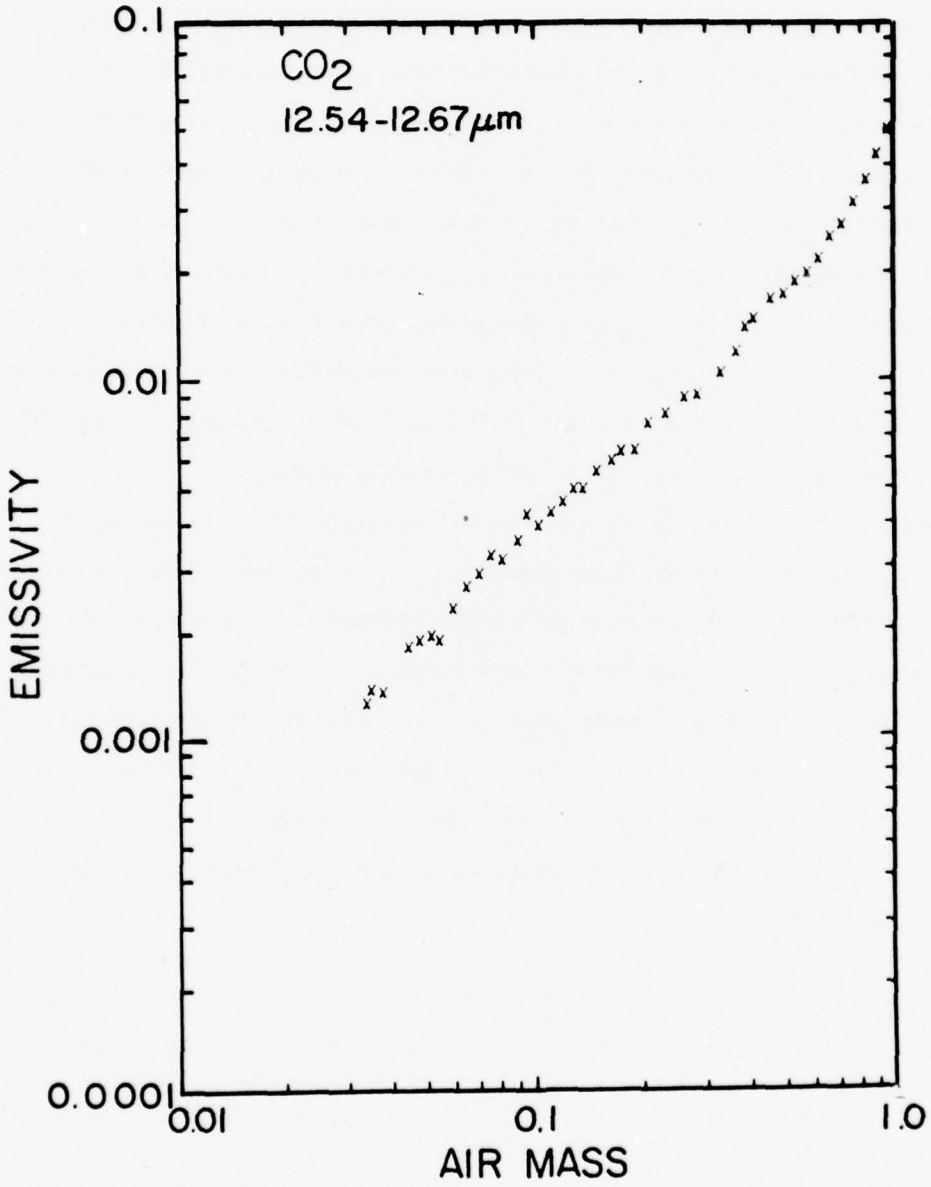

Figure 74. Plot of emissivity vs air mass for spectral region number 16, 19 February 1975.

VI. ANALYSIS OF SPECTRAL RADIANCE

The spectral radiance combined with the observational parameters of pressure, temperature and secant angle are used to calculate constituent concentrations. The derivation of the vertical distribution of the minor constituents is done by fitting the observed integrated radiance of selected isolated spectral regions to the corresponding theoretical integrals. Two methods are used: the line-by-line method and the band model method.[4,5] The individual line parameters (frequencies, intensities, halfwidths and energy levels) and band model parameters (average intensities and average halfwidths) are available for most atmospheric molecules of interest. Elaborate computer programs have been developed for these computations and are currently being used on the CDC 6600/7600 computers at the National Center for Atmospheric Research in Boulder, Colorado.

The radiometric measurements are made from different altitudes $h_1, h_2, \ldots, h_m$ at a constant zenith angle. The atmosphere is assumed to be stratified into layers defined by actual altitudes of observation. The analysis starts at h_1, the highest altitude of observation with the smallest radiance values and then proceeds layer by layer to the lower altitudes with increasing radiance values. The residual atmosphere above h_1 is considered as one homogeneous layer so that the infinite resolution radiance at wavenumber $\nu(cm^{-1})$ to be observed at altitude h_1, $N(\nu, h_1)$ is a one-layer emission.

$$N(\nu, h_1) = \epsilon(v, 1)\, B(\nu, 1),$$

---

[4]A. Goldman, D. G. Murcray, F. H. Murcray, W. J. Williams and J. N. Brooks, "Distribution of Water Vapor in the Stratosphere as Determined from Balloon Measurements of Atmospheric Emission Spectra in the 24-29μm Region," Appl. Opt. 12, 1045-1053, 1973.

[5]D. G. Murcray, A. Goldman, F. H. Murcray, W. J. Williams, J. N. Brooks and D. B. Barker, "Vertical Distribution of Minor Atmospheric Constituents as Derived from Air Borne Measurements of Atmospheric Emission and Absorption Spectra," AIAA Paper No. 73-103, Presented at the 11th Aerospace Sciences Meeting, Washington, D.C. Jan. 10-12, 1973.

where $B(\nu, 1)$ is the black body radiance at temperature θ of layer 1, and $\epsilon(\nu, 1)$ is the infinite resolution emissivity of this layer. The atmosphere below h_1 is divided into m-1 homogeneous layers, defined by h_2, h_3, . . . , h_m. The emission from the first layer is transmitted through the second layer according to $\tau(\nu, 2)\ N(\nu, h_1)$, where $\tau(\nu, 2)$ is the infinite resolution transmittance of the second layer. In addition, the second layer emits radiance according to $\epsilon(\nu, 2)\ B(\nu, 2)$. Thus the infinite resolution radiance observed at h_2, $N(\nu, h_2)$ is given by

$$N(\nu, h_2) = \tau(\nu, 2)\ N(\nu, h_1) + \epsilon(\nu, 2)\ B(\nu, 2).$$

This process proceeds through all the layers below h_1 according to

$$N(\nu, h_n) = \tau(\nu, n)\ N(\nu, h_{n-1}) + \epsilon(\nu, n)\ B(\nu, n) \quad , \text{ for } n = 2, \ldots, m.$$

These equations represent successive equations for $N(\nu, h_n)$, where each step below h_1 involves two consecutive layers.

Assuming no scattering, the relation $\tau(\nu) = 1 - \epsilon(\nu)$ will hold for thermodynamical equilibrium and can be substituted into the above equations. $\tau(\nu, h_n)$ is a function of the amount of constituent U(n) in the layer n between altitudes h_n and h_{n-1}. Once a theoretical model is developed for $\tau(\nu, h_n)$, the equations can be solved successively for U(n), n - 1 , . . . , m, thus yielding the desired constituent profile. However, the observed spectral radiance $\overline{N}(\nu, h_n)$ is not at infinite resolution, but rather is a convolution of the infinite resolution radiance $N(\nu, h_n)$, with the spectrometer slit function $g(\nu - \nu')$ according to

$$\overline{N}(\nu, h_n) = \int_{\nu-a}^{\nu+a} N(\nu, h_n)\ g(\nu - \nu')\ d\nu' \Big/ \int_{\nu-a}^{\nu+a} g(\nu - \nu')\ d\nu',$$

where 2a (cm^{-1}) is the spectral width of the slit function.

The integrated radiance, though, is independent of the slit function, so that

$$\int_{\nu_1}^{\nu_2} N(\nu, h_n)\, d\nu = \int_{\nu_1}^{\nu_2} \overline{N}(\nu, h_n)\, d\nu,$$

where ν_1 and ν_2 are limits of the spectral region under consideration. Thus, the integrated radiance is a suitable parameter for a fitting of theoretical

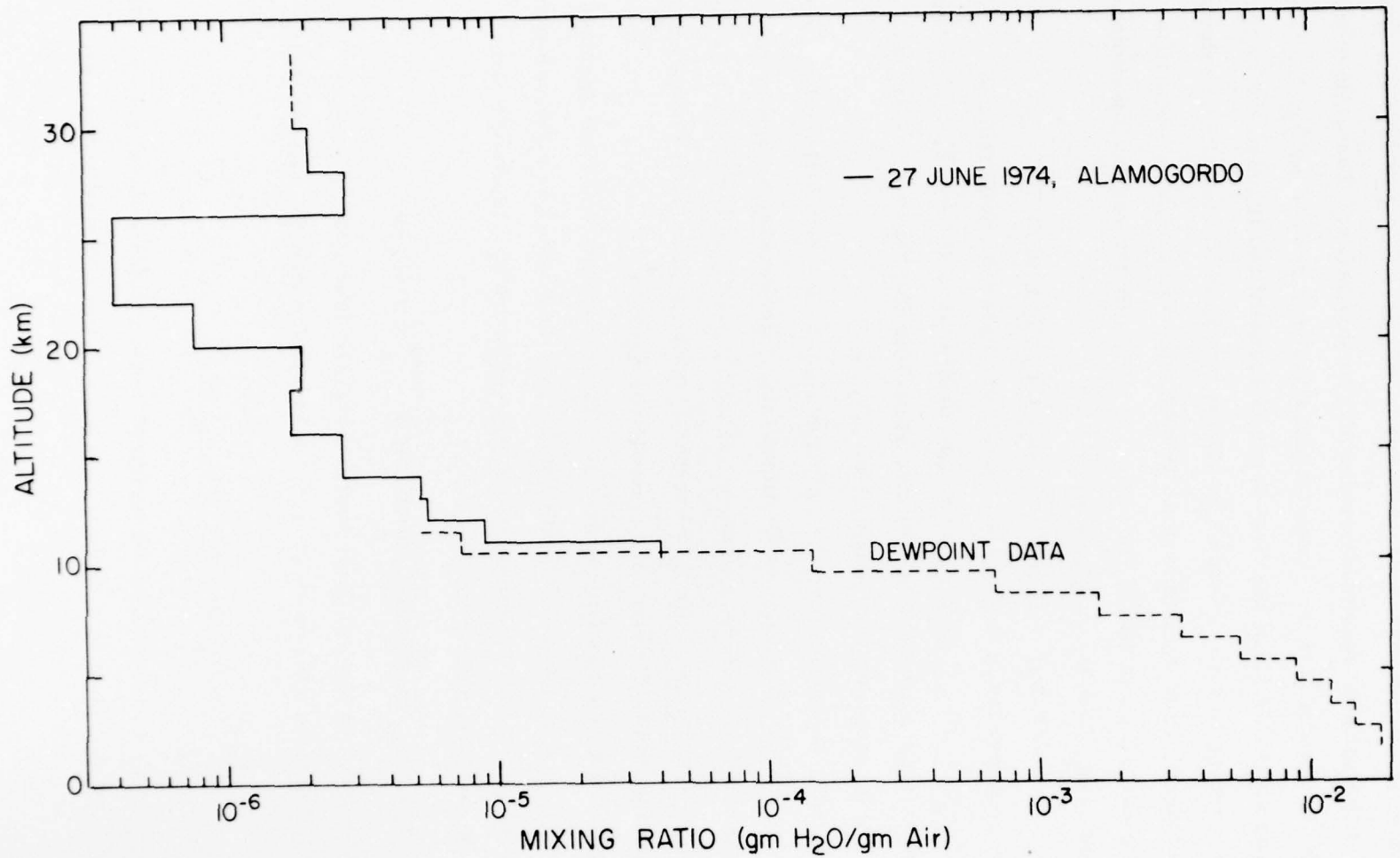

Figure 75. Water vapor mixing ratio height profile derived from spectral radiance measured on the balloon flight of 27 June 1974.

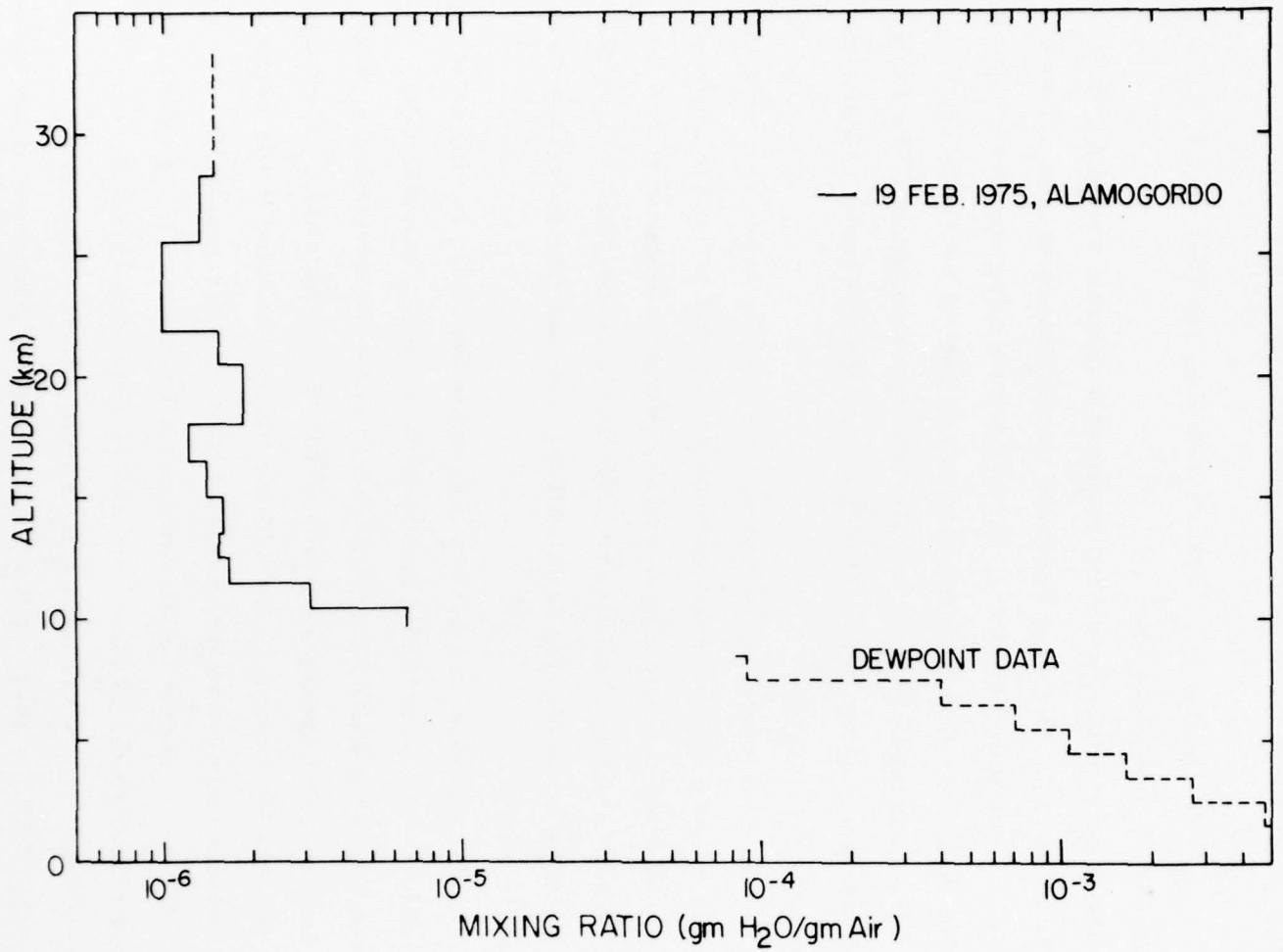

Figure 76. Water vapor mixing ratio height profile derived from spectral radiance measured on the balloon flight of 19 February 1975.

integrated radiance $\int N(\nu, h_n)d\nu$ (over an isolated region) to the experimental values $\int \overline{N}(\nu, h_n)d\nu$ by successive solutions of the equations

$$F[U(n)] = \int_{\nu_1}^{\nu_2} N(\nu, h_n)d\nu - \int_{\nu_1}^{\nu_2} N(\nu, h_n)\, d\nu = 0, \text{ for } U(n), \; n = 1, \ldots, m,$$

where $N(\nu, h_n)$ is given above.

The above determination of U(n) requires a suitable model for the calculation of $\tau(\nu, n)$. The most accurate transmittance is obtained by a line-by-line calculation. However, for some molecular species adequate parametric values for this type calculation are not yet available and band model parameters are used to calculate concentrations. The same basic 2 layer radiometric approach is used and the integrals (calculated and measured) are equated.

The line-by-line model is used to calculate water vapor emission spectra.[4] Mixing ratio height profiles for water vapor using this technique in the 25.2μm region were derived for both flights and are shown in Figures 75 and 76 for the 27 June 1974 and 19 February 1975 flights, respectively. Included on these profiles is the mixing ratio derived from the dew point data shown in Figures 11 and 14.

Band model analysis was used to caluculate the HNO_3 mixing ratio height profiles. The band model parameters for HNO_3 calculated by Goldman et al.[6] have sufficient resolution to allow the derivation of HNO_3 profiles from several spectral regions within the 11.3μm band. Consequently, spectral regions 10 through 13 from Table VII are included in the integrated spectral results rather than just the total band which is region 10. The HNO_3 profiles, of course, should be the same for all regions. The profiles shown in Figures 77 and 78 for 27 June 1974 and 19 February 1975 are derived from two of these regions (10 and 12). Profiles from both regions are included so that both the shape of the profiles and the magnitude of the mixing

---

[6]A. Goldman, T. G. Kyle and F. S. Bonomo, "Statistical Band Model Parameters and Integrated Intensities for the 5.9μm, 7.5μm, and 11.3μm Bands of HNO_3 Vapor," Appl. Opt. 10, 65-73, 1971.

ratios can be compared. The parameter a in these figures is the exponent for the temperature correction term required to adjust the laboratory band model parameters to atmospheric temperatures (see discussion in references 5 and 6). This exponent for the entire band is 1.5 and for narrow spectral regions within the band is 1.0.[7] In one case, however, the total band coefficient was adjusted using a = 1 for comparative purposes (27 June 1974). The various profiles shown in Figures 77 and 78 are very similar, nevertheless, the questions raised by the slight differences are being studied as to their implications.

Band model analysis[8,9] was also used to derive ozone mixing ratio height profiles using radiance data in spectral region 1 at 9μm. This analysis is similar to that used for the HNO_3 and described in references above. For small values of emissivity the mixing ratio for ozone is calculated from the following equation:

$$\beta = \frac{\Delta\epsilon}{(S^o/d)(\Delta P)H} \frac{M(O_3)}{M(air)},$$

where

$\Delta\epsilon = \frac{\Delta N(O_3)}{B(h_n)}$,

ΔN = change in radiance from height h_n to h_{n+1},

S^o/d = average absorption coefficient over spectral region 1,

ΔP = change in pressure from h_n to h_{n+1},

H = atmospheric scale height at $\frac{h_n + h_{n+1}}{2}$,

$M(O_3)$ and $M(air)$ = molecular weight of ozone and air respectively.

[7] D. G. Murcray, A. Goldman, A. Csoeke-Poeckh, F. H. Murcray, W. J. Williams and R. N. Stocker, "Nitric Acid Distribution in the Stratosphere," J. Geophys. Res. 78, 7033-7038, 1973.

[8] A. Goldman, "Statistical Band Model Parameters for Long Path Atmospheric Ozone in the 9-10μm Region," Appl. Opt. 9, 2600-2604, 1970.

[9] A. Goldman and T. G. Kyle, "A Comparison Between Statistical Model and Line-by-Line Calculation with Application to the 9.6μm Ozone and 2.7μm Water Vapor Bands," Appl. Opt. 7, 1167-1177, 1968.

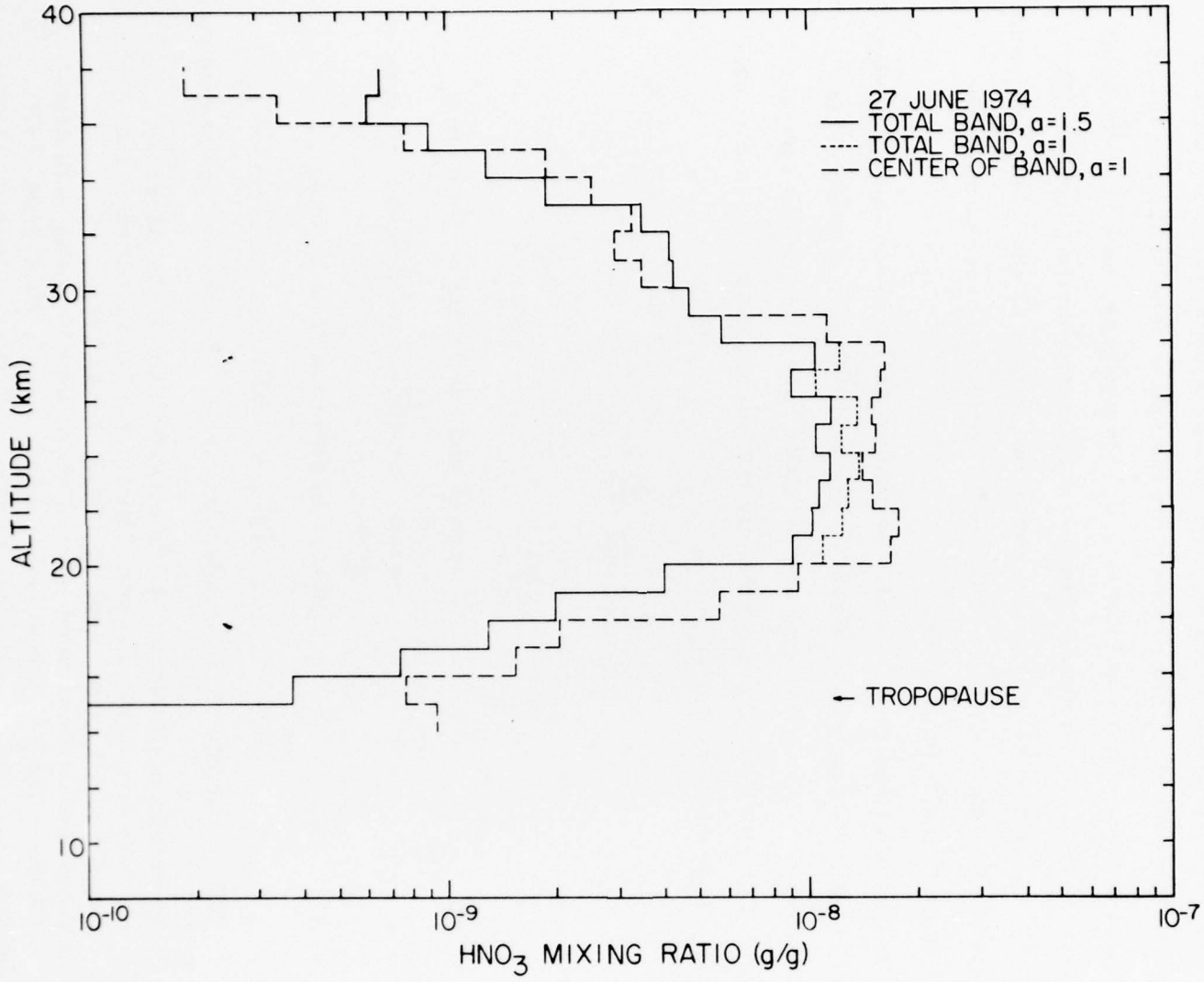

Figure 77. Plot of HNO_3 mixing ratio vs altitude for 27 June 1974.

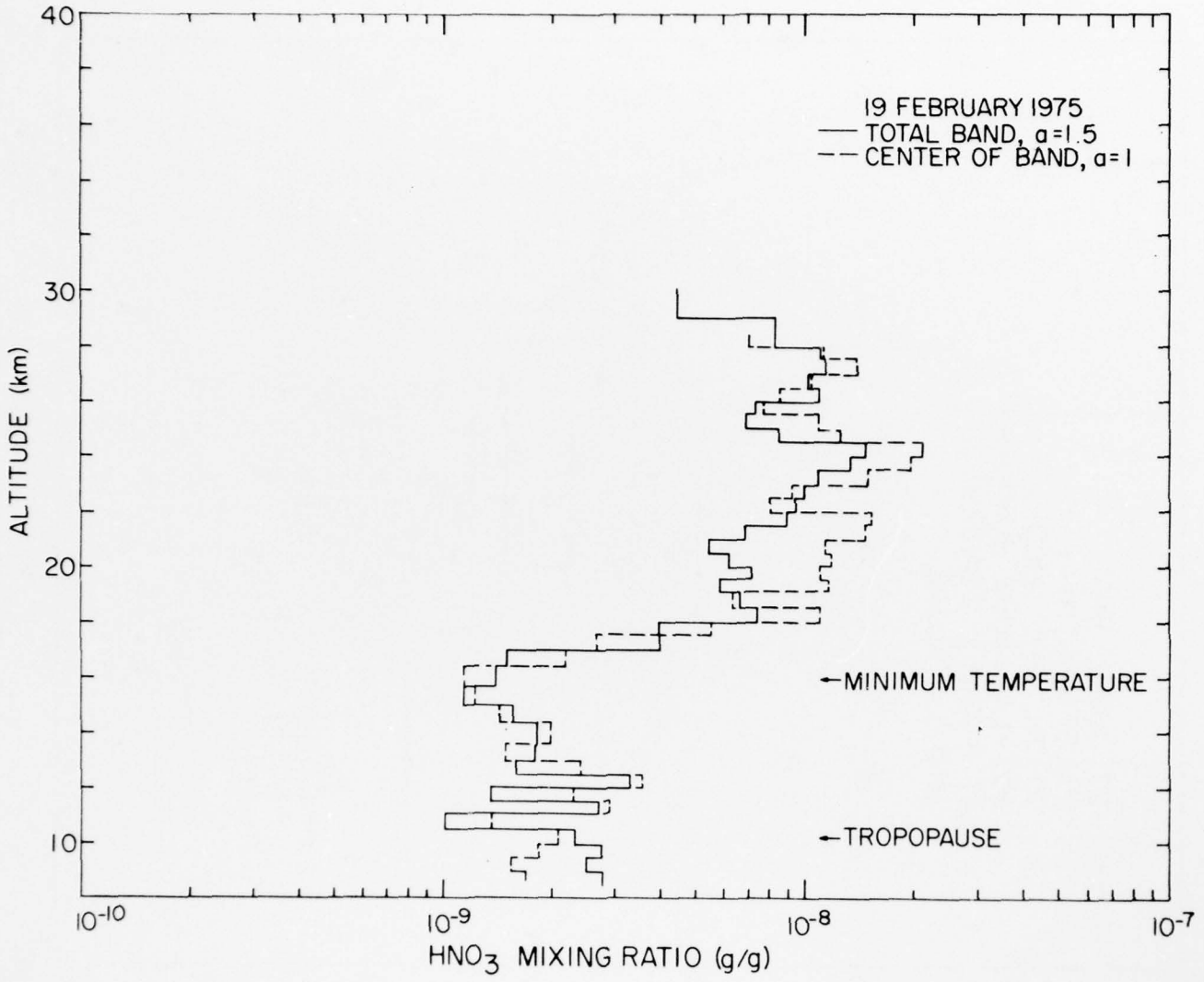

Figure 78. Plot of HNO_3 mixing ratio vs altitude for 19 February 1975.

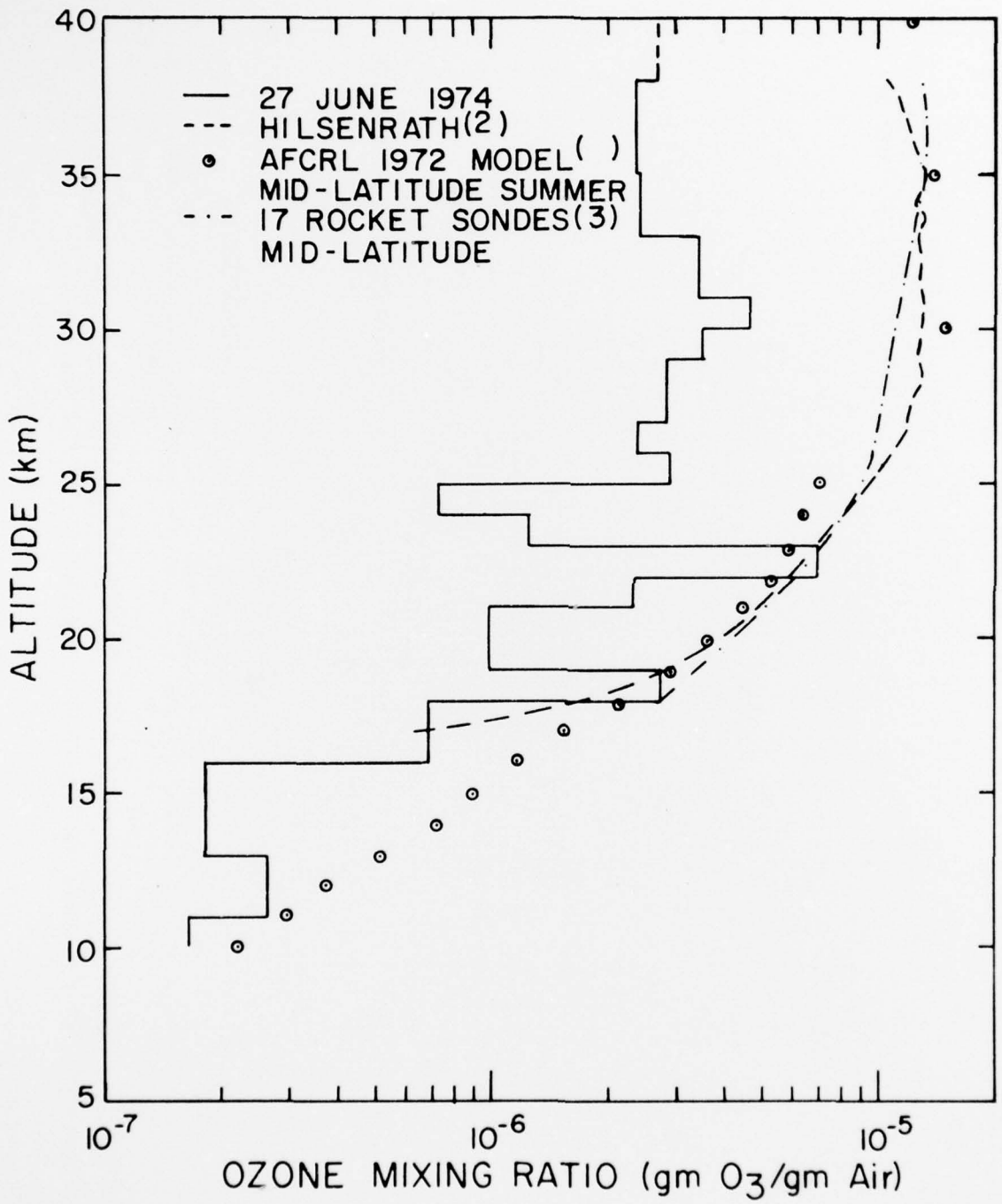

Figure 79. Ozone mixing ratio height profile derived from spectral radiance measured on the balloon flight of 27 June 1974.

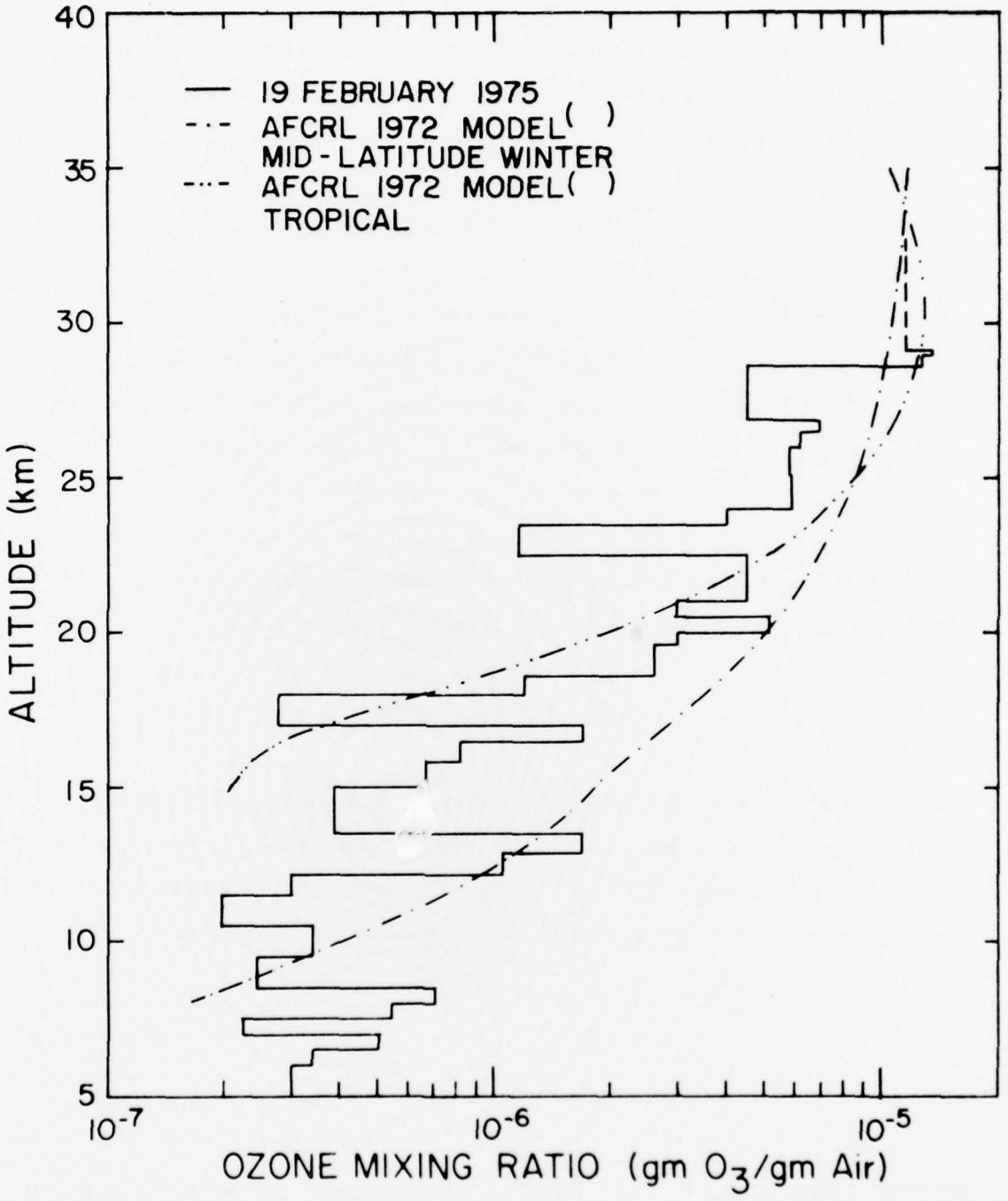

Figure 80. Ozone mixing ratio height profile derived from spectral radiance measured on the balloon flight of 19 February 1975.

The values for $N(O_3)$ have not been significantly smoothed for this initial calculation. As a result some of the apparent layering may be over exaggerated. The derived profiles are shown in Figures 79 and 80 for 27 June 1974 and 19 February 1975. The ozone data of Hilsenrath[2] is included on the 27 June 1974 figure along with mean mid-latitude profiles from rocket soundings[3] and ozone models proposed by AFCRL.[10]

VII. CONCLUSIONS

The liquid helium cooled spectral radiometer designed for the Ballistic Research Laboratories has been operated successfully. A number of instrumental adjustments were indicated as a result of these first two flights. They have been incorporated into the instrument and will be discussed in future reports. The radiometer was designed to measure constituent height profiles. Profiles for several constituents have been reported here. Summaries of these and profiles from additional flights will be presented at an appropriate time.

ACKNOWLEDGMENTS

We wish to thank the National Center for Atmospheric Research, which is sponsored by the National Science Foundation, for computer time used in this research. We wish to thank C. Bauer for preparation of the figures and editing the text and E. Vernon for preparing the text.

[10] R. A. McClatchey, R. W. Fenn, J. E. A. Selby, F. E. Volz and J. S. Garing, "Optical Properties of the Atmosphere," AFCRL-72-0497, Environmental Research Papers, No. 411, 1972.

REFERENCES

1. J. N. Brooks, A. Goldman, J. J. Kosters, D. G. Murcray, F. H. Murcray and W. J. Williams, "Balloon-Borne Infrared Measurements," Phys. Chem. Upper Atmos. (B. McCormac, ed.) 278-285, 1973.

2. E. Hilsenrath and T. A. Ashenfelter, "A Balloon Ozone Measurement Utilizing an Optical Absorption Cell and an Ejector Air Sampler," NASA Technical Note No. NASA TN D-8281, Goddard Space Flight Center, Greenbelt, Md. 20771, July 1976.

3. A. J. Krueger, "The Mean Ozone Distribution of Several Series of Rocket Soundings to 52 km at Latitudes from 58°S to 64°N," Pure Appl. Geophys. 106-108, 1272-1280, 1973.

4. A. Goldman, D. G. Murcray, F. H. Murcray, W. J. Williams and J. N. Brooks, "Distribution of Water Vapor in the Stratosphere as Determined from Balloon Measurements of Atmospheric Emission Spectra in the 24-29μm Region," Appl. Opt. 12, 1045-1053, 1973.

5. D. G. Murcray, A. Goldman, F. A. Murcray, W. J. Williams, J. N. Brooks and D. B. Barker, "Vertical Distribution of Minor Atmospheric Constituents as Derived from Air-Borne Measurements of Atmospheric Emission and Absorption Spectra," AIAA Paper No. 73-103, Presented at the 11th Aerospace Sciences Meeting, Washington, D.C., January 10-12, 1973.

6. A. Goldman, T. G. Kyle and F. S. Bonomo, "Statistical Band Model Parameters and Integrated Intensities for the 5.9μm, 7.5μm, and 11.3μm Bands of HNO_3 Vapor," Appl. Opt. 10, 65-73, 1971.

7. D. G. Murcray, A. Goldman, A. Csoeke-Poeckh, F. H. Murcray, W. J. Williams and R. N. Stocker, "Nitric Acid Distribution in the Stratosphere," J. Geophys. Res. 78, 7033- 7038, 1973.

8. A. Goldman, "Statistical Band Model Parameters for Long Path Atmospheric Ozone in the 9-10μm Region," Appl. Opt. 9, 2600-2604, 1970.

9. A. Goldman and T. G. Kyle, "A Comparison Between Statistical Model and Line-by-Line Calculation with Application to the 9.6μm Ozone and the 2.7μm Water Vapor Bands," Appl. Opt. 7, 1167-1177, 1968.

10. R. A. McClatchey, R. W. Fenn, J. E. A. Selby, F. E. Volz and J. S. Garing, "Optical Properties of the Atmosphere," AFCRL-72-0497, Environmental Research Papers, No. 411, 1972

DISTRIBUTION LIST

No. of Copies	Organization
12	Commander Defense Documentation Center ATTN: DDC-TCA Cameron Station Alexandria, VA 22314
1	Director Institute for Defense Analyses ATTN: Dr. E. Bauer 400 Army-Navy Drive Arlington, VA 22202
2	Director Defense Advanced Research Projects Agency ATTN: STO, CPT J. Justice, Dr. S. Zakanyca 1400 Wilson Boulevard Arlington, VA 22209
1	Director of Defense Research and Engineering ATTN: Mr. D. Brockway Washington, DC 20305
3	Director Defense Nuclear Agency ATTN: STAP (APTL) STRA (RAAE) Dr. C. Blank Dr. H. Fitz, Jr. Washington, DC 20305
5	DASIAC/DOD Nuclear Information and Analysis Center General Electric Company-TEMPO ATTN: Mr. A. Feryok Mr. W. Knapp Dr. T. Stevens Dr. M. Stanton Mr. T. Barrett 816 State Street P.O. Drawer QQ Santa Barbara, CA 93102
1	Commander US Army Materiel Development and Readiness Command ATTN: DRCDMA-ST 5001 Eisenhower Avenue Alexandria, VA 22333
1	Commander US Army Aviation Systems Command ATTN: DRSAV-E 12th and Spruce Streets St. Louis, MO 63166
1	Director US Army Air Mobility Research and Development Laboratory Ames Research Center Moffett Field, CA 94035
1	Commander US Army Electronics Command ATTN: DRSEL-RD Fort Monmouth, NJ 07703
11	Commander/Director US Army Electronics Command Atmospheric Sciences Laboratory ATTN: Dr. E. H. Holt Mr. N. Beyers Mr. F. Horning Mr. R. Olsen Dr. F. E. Niles Dr. D. E. Snider Mr. B. Kennedy Dr. J. Randhawa Mr. H. Ballard Mr. H. Rachele Dr. M. Heaps White Sands Missile Range, NM 88002
1	Commander US Army Missile Command ATTN: DRSMI-R Redstone Arsenal, AL 35809

DISTRIBUTION LIST

No. of Copies	Organization
1	Commander US Army Tank Automotive Development Command ATTN: DRDTA-RWL Warren, MI 48090
1	Commander US Army Mobility Equipment Research & Development Command ATTN: Tech Docu Cen, Bldg. 315 DRSME-RZT Fort Belvoir, VA 22060
1	Commander US Army Armament Command Rock Island, IL 61202
2	Commander US Army Harry Diamond Labs ATTN: DRXDO-TI 2800 Powder Mill Road Adelphi, MD 20783
1	Director US Army TRADOC Systems Analysis Activity ATTN: ATAA-SA White Sands Missile Range NM 88002
1	Commander US Army Nuclear Agency ATTN: Dr. J. Berberet Fort Bliss, TX 79916
3	Commander US Army Research Office ATTN: Dr. A. Dodd Dr. R. Mace Dr. R. Lontz P. O. Box 12211 Research Triangle Park, NC 27709
2	Director US Army BMD Advanced Technology Center ATTN: Mr. W. Davies Mr. M. Capps P.O. Box 1500 Huntsville, AL 35807
1	HQDA (DAEN-RDM, Dr. F. dePercin) Washington, DC 20310
1	Commander US Army Research and Standardization Group (Europe) ATTN: Dr. H. Lemons P. O. Box 15 FPO New York 09510
1	Chief of Naval Research ATTN: Code 418, Dr. J. Dardis Department of the Navy Washington, DC 20360
1	Commander US Naval Surface Weapons Center ATTN: Dr. L. Rutland Silver Spring, MD 20910
1	Commander US Naval Electronics Laboratory ATTN: Mr. W. Moler San Diego, CA 92152
4	Commander US Naval Research Laboratory ATTN: Dr. W. Ali Dr. D. Strobel Code 7700, Mr. J. Brown Code 2020, Tech Lib Washington, DC 20375
4	HQ USAF (AFNIN; AFRD; AFRDQ; ARTAC, COL C. Anderson) Washington, DC 20330

DISTRIBUTION LIST

No. of Copies	Organization
2	AFSC (DLCAW, LTC R. Linkous; SCS) Andrews AFB Washington, DC 20334
10	AFGL (Dr. R. McClatchey; Dr. J. Garing; Dr. H. Gardiner; Mr. D. Smith; Dr. A. T. Stair; Dr. J. Kennealy; Dr. K. Champion; Dr. W. Swider; Dr. T. Keneshea; Dr. R. Narcisi) Hanscom AFB, MA 01730
1	Director National Oceanic and Atmospheric Administration ATTN: Dr. L. Machta US Department of Commerce 8060 13th Street Silver Spring, MD 20910
1	Director National Oceanic and Atmospheric Administration US Department of Commerce ATTN: Dr. E. Ferguson Boulder, CO 80302
1	Director Transportation System Center US Department of Transportation ATTN: Dr. T. Hard 55 Broadway Cambridge, MA 02142
1	Director Air Pollution Technical Information Center US Environmental Protection Agency ATTN: P. Halpin Research Triangle Park NC 27709
1	National Center for Atmospheric Research ATTN: Dr. J. Gille P. O. Box 3000 Boulder, CO 80303
1	Director Lawrence Livermore Laboratory ATTN: Dr. H. Ellsaesser, L-71 P. O. Box 808 Livermore, CA 94550
4	Director Los Alamos Scientific Lab ATTN: Dr. W. Maier (Gp J-10) Dr. J. Zinn (MS 664) Dr. W. Myers Dr. M. Peek P. O. Box 1663 Los Alamos, NM 87544
2	Director Jet Propulsion Laboratory ATTN: Dr. C. Farmer Dr. R. Toth 4800 Oak Grove Drive Pasadena, CA 91103
4	Director National Aeronautics and Space Administration Goddard Space Flight Center ATTN: Dr. E. Hilsenrath Dr. V. Kunde Dr. A. Aikin Dr. R. Goldberg Greenbelt, MD 20771
1	Director National Aeronautics and Space Administration Langley Research Center ATTN: Dr. J. Russell Hampton, VA 23365

DISTRIBUTION LIST

No. of Copies	Organization
2	Director National Science Foundation ATTN: Dr. F. Eden Dr. G. Adams 1800 G Street, NW Washington, DC 20550
2	General Electric Company Valley Forge Space Technology Center ATTN: Dr. M. Bortner Dr. T. Baurer P. O. Box 8555 Philadelphia, PA 19101
1	General Research Corporation ATTN: Dr. R. Zirkind 1501 Wilson Boulevard Arlington, VA 22209
3	Lockheed Palo Alto Research Laboratory ATTN: Dr. B. McCormack Dr. J. Ragan Mr. R. Sears 3251 Hanover Street Palo Alto, CA 94304
1	Mission Research Corporation ATTN: Dr. R. Hendrick 735 State Street P. O. Drawer 719 Santa Barbara, CA 93101
1	Mitre Corporation ATTN: Tech Lib P. O. Box 208 Bedford, MA 01730
1	R&D Associates ATTN: Dr. F. Gilmore P. O. Box 9695 Marina del Rey, CA 90291
2	Sandia Laboratories ATTN: Dr. R. O. Woods Dr. F. Hudson P. O. Box 5800 Albuquerque, NM 87115
1	The Ohio State University Department of Physics ATTN: Dr. J. Shaw Columbus, OH 43210
1	Stanford Research Institute ATTN: Dr. J. Peterson 333 Ravenswood Avenue Menlo Park, CA 94025
6	University of Denver Denver Research Institute ATTN: Dr. R. Amme Dr. D. Murcray Dr. A. Goldman Dr. J. Williams Mr. J. Brooks Mr. J. Kosters P. O. Box 10127 Denver, CO 80210
1	University of Illinois Dept of Electrical Engineering ATTN: Dr. C. Sechrist, Jr. Urbana-Champaign Campus Urbana, IL 61801
2	University of Michigan High Altitude Engineering Lab ATTN: Dr. F. Bartman Dr. S. Drayson Rsch Activities Building Ann Arbor, MI 48105
1	University of Minnesota, Morris Div of Science and Mathematics ATTN: Dr. M. N. Hirsh Morris, MN 56267

DISTRIBUTION LIST

No. of Copies	Organization
1	University of Wyoming Dept of Physics & Astronomy ATTN: Dr. T. Pepin Laramie, WY 82070
4	Utah State University Center for Research in Aeronomy ATTN: Dr. L. Megill Dr. P. Williamson Dr. K. Baker Dr. D. Baker Logan, UT 84321

Aberdeen Proving Ground

Marine Corps Ln Ofc
Dir, USAMSAA